UNIVERSITY OF CALIFORNIA SAN DIEGO

Spatial-Temporal Dynamics in Multi-Strain Bacterial Populations

A dissertation submitted in partial satisfaction of the
requirements for the degree
Doctor of Philosophy

in

Physics

by

Liyang Xiong

Committee in charge:

Massimo Vergassola, Chair
Lev Tsimring, Co-Chair
Olga Dudko
Jeff Hasty
Terence Hwa

2019

The dissertation of Liyang Xiong is approved, and it is acceptable in quality and form for publication on microfilm and electronically:

_____

_____

_____

_____
Co-Chair

_____
Chair

University of California San Diego

2019

EPIGRAPH

The single greatest constant of history is that everything changes.

—Yuval Noah Harari, *Homo Deus: A Brief History of Tomorrow*

TABLE OF CONTENTS

LIST OF FIGURES

LIST OF TABLES

ACKNOWLEDGEMENTS

I would like to thank my advisors, Lev Tsimring and Jeff Hasty, for their mentoring and guidance during my five years at UCSD. Without their patience and encouragement, I would not have been able to succeed in completing my Ph.D. research. Lev and Jeff taught me how to conduct scientific research and solve problems and their advice in my research has always been insightful and inspiring. Lev plays the most influential role in every project I have worked on at UCSD. Lev's office is close to mine and we had a lot of discussions which often led to good ideas. Lev is extremely insightful in mathematical modeling and simulations which often motivates me. Besides, he is also an excellent photographer and often travels around the world. His love of life also inspires me.

I want to thank Robert Cooper, who taught me how to do biological experiments and has always been a very good friend. We often discussed science and other stuff and I learned a lot from his critical thinking. Besides, I would like to recognize everyone in Biodynamics Lab who were very helpful in my daily life and made my Ph.D. life more colorful.

I would also like to thank my other committee members: Massimo Vergassola, Olga Dudko and Terence Hwa. It is my great honor to have them serve on my committee.

Last but not least, I want to thank my family and Anzhi for their love and unwavering support.

Chapter 2 contains material originally published as Xiong, L., Cooper, R. and Tsimring, L.S., 2018. Coexistence and pattern formation in bacterial mixtures with contact-dependent killing. *Biophysical Journal*. The dissertation author was the primary investigator of this paper.

Chapter 3 contains material being prepared for submission as Xiong, L., Cao, Y., Cooper, R., Rappel, W.J., Hasty, J. and Tsimring, L., 2019. Flower-like patterns in multi-species bacterial colonies. The dissertation author was the primary investigator of this paper.

Chapter 4 contains material originally published as Humphries, J., Xiong, L., Liu, J., Prindle,

A., Yuan, F., Arjes, H.A., Tsimring, L. and Suel, G.M., 2017. Species-independent attraction to biofilms through electrical signaling. *Cell*. The chapter also contains material originally published as Scott, S.R., Din, M.O., Bittihn, P., Xiong, L., Tsimring, L.S. and Hasty, J., 2017. A stabilized microbial ecosystem of self-limiting bacteria using synthetic quorum-regulated lysis. *Nature Microbiology*. The dissertation author was the primary investigator of these papers.

VITA

2014	B.S. in Physics, Peking University, Beijing, China
2019	Ph.D. in Physics, University of California, San Diego

PUBLICATIONS

Xiong, L., Cao, Y., Cooper, R., Rappel, W.J., Hasty, J. and Tsimring, L., 2019. Flower-like patterns in multi-species biofilms. *bioRxiv*, p.550996. (submitted to peer-reviewed journal)

Xiong, L., Cooper, R. and Tsimring, L.S., 2018. Coexistence and pattern formation in bacterial mixtures with contact-dependent killing. *Biophysical journal*, 114(7), pp.1741-1750.

Scott, S.R., Din, M.O., Bittihn, P., Xiong, L., Tsimring, L.S. and Hasty, J., 2017. A stabilized microbial ecosystem of self-limiting bacteria using synthetic quorum-regulated lysis. *Nature microbiology*, 2(8), p.17083.

Humphries, J., Xiong, L., Liu, J., Prindle, A., Yuan, F., Arjes, H.A., Tsimring, L. and Suel, G.M., 2017. Species-independent attraction to biofilms through electrical signaling. *Cell*, 168(1-2), pp.200-209.

Shi, W., Ma, W., Xiong, L., Zhang, M. and Tang, C., 2017. Adaptation with transcriptional regulation. *Scientific reports*, 7, p.42648.

Xiong, L., Shi, W. and Tang, C., 2016. Adaptation through proportion. *Physical biology*, 13(4), p.046007.

ABSTRACT OF THE DISSERTATION

Spatial-Temporal Dynamics in Multi-Strain Bacterial Populations

by

Liyang Xiong

Doctor of Philosophy in Physics

University of California San Diego, 2019

Massimo Vergassola, Chair
Lev Tsimring, Co-Chair

Bacteria are widespread on Earth. They play important roles in shaping the global ecosystems as well as influencing human health. In nature, different bacterial species often coexist in a common environment. The interactions of them are diverse and often lead to intricate spatial-temporal dynamics. Quantitative experimental measurements as well as mathematical modeling could help us better understand the mechanisms behind such dynamics. In this dissertation, I discuss several spatial-temporal structures for multi-strain bacterial systems and different modeling strategies are used to help explore the mechanisms of different spatial-temporal patterns. A key

question regarding a system of different bacterial species is how coexistence is maintained, considering that different bacterial species often have different growth rates and they can even kill each other sometimes. In Chapter Two, I discuss a novel theoretical framework for robust coexistence and pattern formation in bacterial mixtures with contact-dependent killing. In Chapter Three, I present a beautiful spatial flower-like pattern in two-species bacterial systems from experiments and build two different models, a discrete interface model and a phase-field model, to elucidate how differential motility and mechanical interactions between bacterial species can create complex spatial structures. In Chapter Four, I introduce the agent-based modeling, which simulates each individual bacterial cell in large populations. Two examples of applications of such agent-based modeling in microfluidic environments are described. All these chapters combine to highlight the effort towards understanding the spatial-temporal dynamics of multi-strain microbial systems quantitatively.

Chapter 1

Introduction

Microbial communities inhabit every ecosystem on Earth, from soil to hydrothermal vents to plants to the human gut [1, 2, 3]. They often form dense biofilms, whose structures are shaped by biological, chemical, and physical factors [4, 5, 6]. In the wild, most biofilms are comprised of multiple bacterial strains. They feature a diverse repertoire of social interactions, including cooperation [7, 8], competition [9], and predation [10]. Bacteria often signal, sense, and respond to each other through secondary metabolites [11] or antibiotic compounds [12], and co-cultures can even exhibit different motility from either species on its own [13]. These interactions may lead to the emergence of complex spatial structures, which can have a profound effect on bacteria survival and function, and promote biodiversity by optimizing the division of labor within the biofilm [14]. Spatial structure can also enhance horizontal gene transfer among different species [15].

All these complicated interactions determine that bacterial systems are often not at steady states but rather dynamical and coupled to the environments they inhabit. Understanding the mechanisms of the various spatial-temporal dynamics is critical and can benefit human health [16], industrial fermentation [17], agriculture [18], etc. To better unveil the fundamental principles governing the dynamics of bacterial systems, quantitative methods are essential. In quantitative

biology, the combination of quantitative experimental measurements and mathematical modeling could not only shed light on the explanation of observed phenomena, but also help make predictions about the living systems. Building predictive models for microbial communities in nature is often challenging, considering the large number of bacterial species and their diverse interactions. However, even starting from relatively simple systems with only a few strains or species present, the principles for microbial organization uncovered could be general and provide hints at systems with more complexity. In the next few chapters, I would like to illustrate some examples of how modeling and experiments can be combined to explore different dynamics in different multi-strain bacterial populations.

References

[1] Craig L Moyer, Fred C Dobbs, and David M Karl. Phylogenetic diversity of the bacterial community from a microbial mat at an active, hydrothermal vent system, loihi seamount, hawaii. *Applied and environmental microbiology*, 61(4):1555–1562, 1995.

[2] Steven R Gill, Mihai Pop, Robert T DeBoy, Paul B Eckburg, Peter J Turnbaugh, Buck S Samuel, Jeffrey I Gordon, David A Relman, Claire M Fraser-Liggett, and Karen E Nelson. Metagenomic analysis of the human distal gut microbiome. *science*, 312(5778):1355–1359, 2006.

[3] Noah Fierer and Robert B Jackson. The diversity and biogeography of soil bacterial communities. *Proceedings of the National Academy of Sciences*, 103(3):626–631, 2006.

[4] Paul Stoodley, Karin Sauer, David Gwilym Davies, and J William Costerton. Biofilms as complex differentiated communities. *Annual Reviews in Microbiology*, 56(1):187–209, 2002.

[5] Hans-Curt Flemming, Jost Wingender, Ulrich Szewzyk, Peter Steinberg, Scott A Rice, and Staffan Kjelleberg. Biofilms: an emergent form of bacterial life. *Nature Reviews Microbiology*, 14(9):563, 2016.

[6] Reed M Stubbendieck, Carol Vargas-Bautista, and Paul D Straight. Bacterial communities: interactions to scale. *Frontiers in microbiology*, 7:1234, 2016.

[7] Eshel Ben-Jacob, Inon Cohen, and Herbert Levine. Cooperative self-organization of microorganisms. *Advances in Physics*, 49(4):395–554, 2000.

[8] Ashleigh S Griffin, Stuart A West, and Angus Buckling. Cooperation and competition in pathogenic bacteria. *Nature*, 430(7003):1024–1027, 2004.

[9] Michael E Hibbing, Clay Fuqua, Matthew R Parsek, and S Brook Peterson. Bacterial competition: surviving and thriving in the microbial jungle. *Nature Reviews Microbiology*, 8(1):15–25, 2010.

[10] Klaus Jürgens and Carsten Matz. Predation as a shaping force for the phenotypic and genotypic composition of planktonic bacteria. *Antonie van Leeuwenhoek*, 81(1-4):413–434, 2002.

[11] Matthew F Traxler, Jeramie D Watrous, Theodore Alexandrov, Pieter C Dorrestein, and Roberto Kolter. Interspecies interactions stimulate diversification of the streptomyces coelicolor secreted metabolome. *MBio*, 4(4):e00459–13, 2013.

[12] Paolina Garbeva, Cornelis Hordijk, Saskia Gerards, and Wietse de Boer. Volatile-mediated interactions between phylogenetically different soil bacteria. *Frontiers in microbiology*, 5:289, 2014.

[13] Lucy M McCully, Adam S Bitzer, Sarah C Seaton, Leah M Smith, and Mark W Silby. Interspecies social spreading: Interaction between two sessile soil bacteria leads to emergence of surface motility. *mSphere*, 4(1):e00696–18, 2019.

[14] Carey D Nadell, Knut Drescher, and Kevin R Foster. Spatial structure, cooperation and competition in biofilms. *Nature Reviews Microbiology*, 14(9):589, 2016.

[15] Robert M Cooper, Lev Tsimring, and Jeff Hasty. Inter-species population dynamics enhance microbial horizontal gene transfer and spread of antibiotic resistance. *Elife*, 6:e25950, 2017.

[16] Ilseung Cho and Martin J Blaser. The human microbiome: at the interface of health and disease. *Nature Reviews Genetics*, 13(4):260, 2012.

[17] Ignacio Belda, Iratxe Zarraonaindia, Matthew Perisin, Antonio Palacios, and Alberto Acedo. From vineyard soil to wine fermentation: microbiome approximations to explain the terroir concept. *Frontiers in microbiology*, 8:821, 2017.

[18] Jacqueline M Chaparro, Amy M Sheflin, Daniel K Manter, and Jorge M Vivanco. Manipulating the soil microbiome to increase soil health and plant fertility. *Biology and Fertility of Soils*, 48(5):489–499, 2012.

Chapter 2

Coexistence and pattern formation in bacterial mixtures with contact-dependent killing

2.1 Introduction

In natural habitats, microorganisms often form multispecies communities with intricate social organization and complex spatial structure [1]. The repertoire of interactions among microorganisms is very diverse and includes cooperation [2, 3], competition for common resources [4, 5], and predation [6, 7, 8]. One major question drawing significant interest is how different microbial species may stably coexist within a common environment in the presence of competition and predation [4, 9]. In this chapter, we address this question theoretically, focusing on one ubiquitous mechanism of bacterial predation: contact-dependent killing of neighboring cells by direct injection of lethal toxins via the type VI secretion system (T6SS) [10, 11, 12, 13, 14, 15, 16]. The T6SS has been found in many genera of bacteria, including *Vibrio*, *Pseudomonas*, and *Acinetobacter*.

In a recent paper [17], Borenstein et al. demonstrated that while small micro-colonies of T6SS-sensitive cells are quickly eliminated by surrounding T6SS-active cells, sufficiently large micro-colonies can survive the assault and expand. They explained this size-dependent bifurcation with a purely geometric mechanism. Since the killing occurs on the perimeter of the colony, and the growth is in the bulk, the overall balance between killing and growth depends on the colony size. However, these theoretical results predicted no stable coexistence; rather, T6SS inhibition was expected to lead to bistability. Depending on initial conditions, either the T6SS-sensitive or T6SS-active bacteria outcompete the other strain and asymptotically approach a spatially uniform state. The experiments with mixtures of *E. coli* (T6SS-sensitive strain) and *Vibrio cholerae* (T6SS-active strain) indeed showed either growth or shrinkage of localized domains of *E. coli* depending on their initial size. However, the finite time span of the experiments did not allow the authors to see complete elimination of one strain, thus the question of possible coexistence remained open. McNally et al. [18] also recently studied phase separation in a system of two mutually-antagonistic T6SS-active strains of *V. cholerae* and found persistent domain coarsening, which indicates that the stronger strain would eventually win the competition.

In another recent paper [19], Blanchard et al. computationally studied the dynamics of a bacterial population with contact-dependent inhibition, such as that mediated by the T6SS. In the well-mixed case, they also found bistability leading to extinction of one strain or the other. On the other hand, they reported that in spatio-temporal simulations, if the diffusion of bacteria was sufficiently slow, two strains could coexist separated by stationary interfaces in a finite parameter domain. However, this effect in their two-component model with bistability could have been a consequence of front pinning that may sometimes occur in coarse finite-difference numerical simulations [20] (see more on this in the Discussion).

While local antagonistic interactions generically lead to phase separation and coarsening via front propagation and thus cannot sustain stable strain coexistence, additional long-range interactions

may potentially change this outcome and lead to stable coexistence. In this chapter, we revisit the possibility of stable coexistence in a binary mixture of T6SS-active and T6SS-sensitive bacteria, taking into consideration the potential effects of long-range growth inhibition. We demonstrate theoretically and numerically, using both continuous deterministic and discrete stochastic models, that the interplay of short-range killing and long-range growth inhibition can indeed stabilize the system in a bimodal state with well-separated patches of different bacterial strains. Furthermore, when diffusion of the inhibitor is fast but finite, stable patterns with a characteristic spatial scale can emerge. Such long-range growth inhibition can plausibly arise in natural settings, since a number of factors that limit colony growth, including resource availability, waste accumulation, and quorum sensing, are mediated by fast-diffusing small molecules [21, 22, 23]. Long-range growth inhibition can also be forward-engineered using the tools of modern synthetic biology [24], for example, by placing an antibiotic resistance gene under the control of a promoter that is repressed by a fast-diffusing quorum-sensing signal (e.g. AHL).

2.2 Methods

2.2.1 Continuum deterministic model

We developed a continuum population dynamics model for a binary mixture of two strains of bacteria that grow on a two-dimensional surface and interact via both short-range contact-dependent killing and long-range growth inhibition. The model is based on the partial differential equations for the area densities of T6SS-sensitive bacteria $n_1(\mathbf{r},t)$ and T6SS-active bacteria $n_2(\mathbf{r},t)$, and the reaction-diffusion equation for the density of the growth inhibitor $A(\mathbf{r},t)$ in a two-dimensional

space, $\mathbf{r} \in \mathbf{R}^2$:

$$\frac{\partial n_1}{\partial t} = \frac{\gamma_1}{1+A} n_1(1-n_1-n_2) - \delta n_1 - \kappa n_1 n_2 + \nabla^2 n_1 \tag{2.1}$$

$$\frac{\partial n_2}{\partial t} = n_2(1-n_1-n_2) - \delta n_2 + \nabla^2 n_2 \tag{2.2}$$

$$\frac{\partial A}{\partial t} = \gamma_A n_1 - \delta_A A + D_A \nabla^2 A \tag{2.3}$$

The first equation describes the logistic growth of the T6SS-sensitive cells, their spontaneous death, killing by co-located T6SS-active cells, and diffusion. Note that the growth rate of T6SS-sensitive strain 1 is reduced by the local concentration of inhibitor $A(\mathbf{r},t)$. We use a simple Hill-like function for the inhibition since the specific form is not qualitatively important. The second equation describes the logistic growth of T6SS-active cells, their spontaneous death, and diffusion. The death rates of both strains are small, and if they move on solid agar, their diffusion rates are also small. While these parameters can be different for the two strains, that difference is not essential, and we assume them to be equal for simplicity. The third equation describes synthesis, decay, and diffusion of the inhibitor A that reduces the growth rate of species n_1. This model has a typical structure of a reaction-diffusion system. Strictly speaking, bacterial communities are not reaction-diffusion systems since they do not "react" with each other as chemical species, and their motility is often quite different from simple linear diffusion. However, such simplified description of their collective dynamics (growth, death, interactions, and motility) is convenient and may serve as a reasonable first approximation to more realistic models of multi-strain bacterial communities.

Here, we assume that A is only produced by n_1 and only inhibits growth of n_1. This interaction of A only with n_1 can be realized in synthetic biology as discussed later. However, in natural environments, it might also be produced by n_2 and inhibit growth of n_2. The analysis of a more general model with A produced by and inhibiting growth of both strains is discussed in Appendix, where we also allow for different death rates of the two strains. In the analysis and

simulations described below, we use Eqs. (2.1)-(2.3) for simplicity, but our main conclusions are general. In these equations, all variables and parameters are scaled by the growth rate of species 2, the diffusion constant of both strains, and the maximum total density of bacteria at which the logistic growth saturates. Note that in our model the cell growth saturates in the bulk at sufficiently large density, while Borenstein et al. [17] assumed that growth was continuous, with new cells pushing old cells out of the simulation domain once the maximum density was reached. This is an important difference, since in the latter case, the faster-growing strain always wins for sufficiently large initial domains, while in our system, the outcome is more complex and parameter-dependent.

2.2.2 Discrete stochastic model

We also developed a lattice-based, discrete-element model to study the effects of stochasticity on the population dynamics of two bacterial strains. We assume that each site of a square lattice may contain an integer number of T6SS-sensitive and T6SS-active cells, n_1 and n_2, respectively. At every time step, each cell can divide with a probability that is proportional to its growth rate (γ_1 or γ_2, respectively), thereby increasing the occupancy number of the corresponding cell type in that lattice site by one. We assume that each lattice site can only accommodate no more than n_0 cells, so once the total number of cells $n_1 + n_2$ at a certain lattice site reaches n_0, cell division at that site is suspended. To model the short-range cell motility, we allow cells to hop to any of four neighboring lattice sites with rates P_n if that neighboring site has a vacancy. A cell can also spontaneously die with probability proportional to δ, thus reducing the number of cells of its type in its lattice site by one. Finally, type-2 cells can kill type-1 cells with probability proportional to κ if they occupy the same site, thus reducing the occupancy number n_1 by one. All these processes are simulated as independent Markovian events. We also introduce a real-valued inhibitor field A that is defined on the same lattice. It is produced at each lattice site in proportion to the corresponding n_1 value, degrades with rate δ_A, and diffuses with the diffusion constant D_A. The spatio-temporal evolution

of A was simulated deterministically using the first-order split-step pseudo-spectral method. We employed 256×256 or 512×512 lattices with periodic boundary conditions.

2.3 Results

2.3.1 Continuum deterministic theory

Population dynamics without long-range inhibition

Let us first consider the two-species population dynamics without long-range inhibition by assuming $\gamma_A = 0$ and imposing the initial condition $A(\mathbf{r},0) = 0$. Clearly, $A(\mathbf{r},t)$ will then remain zero at all times and can be omitted from consideration. The set of two Eqs. (2.1), (2.2) possesses at most four fixed points, including the trivial fixed point $n_{1,2} = 0$, two "pure" states in which either $n_1 = 0, n_2 \neq 0$ or $n_1 \neq 0, n_2 = 0$, and a mixed state where both $n_{1,2} \neq 0$. The linear stability analysis (see Appendix of this Chapter) shows that if $\delta < 1, \gamma_1$, the trivial state is always unstable, and pure n_1 and n_2 states are stable for sufficiently large and small γ_1, respectively. For intermediate γ_1, at $1 < \gamma_1 < 1 + \kappa(1-\delta)/\delta$, the system is bistable (see Fig. 2.7A, blue wedge). In the following, we will always assume $\gamma_1 > 1$, since the most interesting dynamics occur within this regime. For non-zero γ_A, the bifurcation analysis can be carried out as well (Appendix of this Chapter).

In the bistable regime, two sub-colonies dominated by species 1 and 2, can coexist by occupying different spatial domains. If these domains contact each other and the diffusion coefficients of the two species are non-zero, smooth fronts will form separating the domains of different species. These fronts will generally move in either direction depending on the system parameters γ_1, δ, κ. Generally, since $\gamma_1 > 1$, for small killing rate κ, the front propagates in the direction of species 2, and species 1 wins, while for sufficiently large κ the front reverses, and T6SS-active species 2 wins. For given γ_1 and δ, there is a unique value of κ_s at which the front is stationary. For $\delta, \kappa \ll 1$ it can

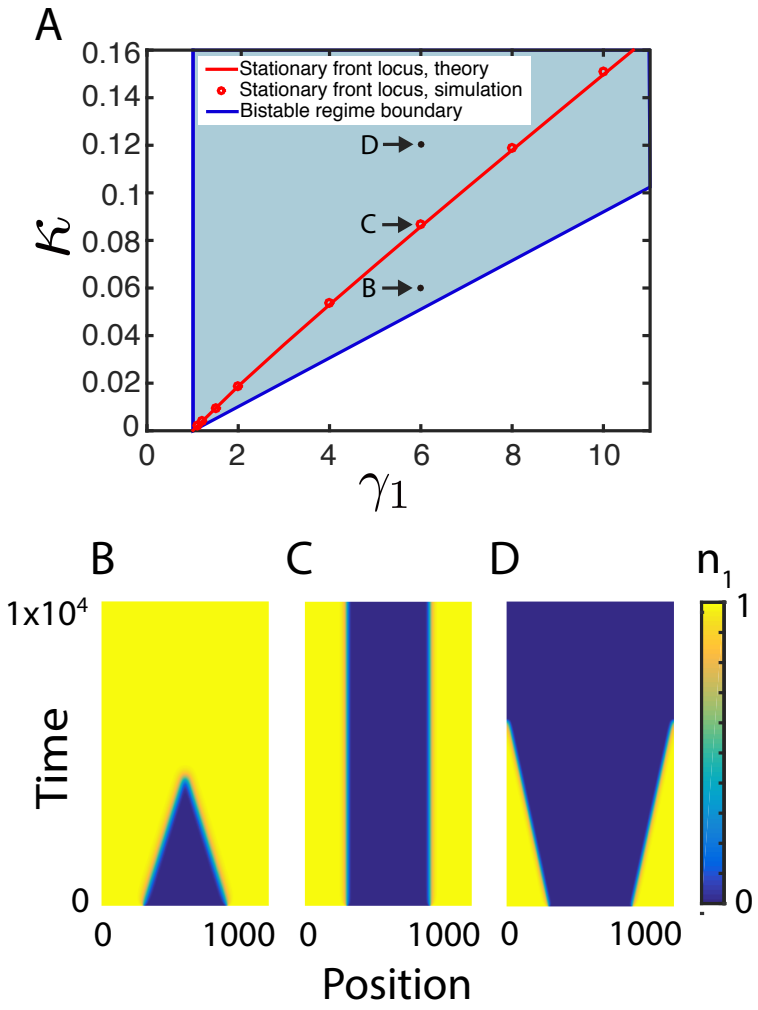

Figure 2.1: (A) The blue-shaded wedge in the parameter plane (γ_1, κ) for $\delta = 0.01$ shows the region of bistability in which both pure states are stable and may transiently coexist in space; however, the fronts separating them would generically move in either direction when diffusion is not zero. (B, C, D) demonstrate how one-dimensional fronts reverse direction when κ is increased from 0.06 (B) to 0.087 (C) to 0.12 (D) for $\gamma_1 = 6$ [direct numerical integration of Eqs. (2.1), (2.2)]. Only the dynamics of n_1 are shown here. In the region where n_1 is high, n_2 is low and vice versa. The red solid line in (A), which is plotted according to formula (2.4), corresponds to the stationary front solution. It separates the parameter regions in which either n_1 or n_2 win the competition. The symbols show the parameters values for which the fronts were indeed found to be stationary in direct simulations.

be found analytically using the so-called Maxwell rule [25] (see Appendix for details),

$$\kappa_s = \frac{3\delta(\gamma_1 - 1)^2(\gamma_1^2 - 1 - 2\gamma_1 \ln \gamma_1)}{2\gamma_1^3 + 3\gamma_1^2 - 6\gamma_1 + 1 - 6\gamma_1^2 \ln \gamma_1} \tag{2.4}$$

For small $\gamma_1 - 1$, this expression simplifies to $\kappa_s = 2\delta(\gamma_1 - 1)$. Direct numerical simulations of Eqs. (2.1), (2.2) agree well with this formula (Fig. 2.1).

Infinitely fast inhibitor diffusion

In the limit of infinitely fast inhibitor diffusion ($D_A \to \infty$), A is spatially-uniform with a magnitude that is dependent on the average concentration of type-1 bacteria over the entire domain: $N_1(t) = \int_C n_1(\mathbf{r},t)d\mathbf{r}/\text{Area}(C)$. For $\delta_A \gg \delta$, after the initial transient, the magnitude of the inhibitor A becomes slaved to the current value of N_1: $A(t) = \gamma_A N_1(t)/\delta_A$. In the bistable regime, after the phase separation has occurred, $N_1 \approx n_1^* s_1$, where s_1 is the surface area fraction occupied by the type-1 strain and $n_1^* = 1 - \delta(1+A)/\gamma_1$ is at the local fixed point. This yields the self-consistency condition resulting in the relation between s_1 and A:

$$A = \frac{\gamma_1 - \delta}{\frac{\delta_A \gamma_1}{\gamma_A s_1} + \delta}. \tag{2.5}$$

Now we can use the results of the analysis of the two-variable model with re-normalized

$$\gamma_1^* = \gamma_1/(1+A) = (\delta_A \gamma_1 + \delta\gamma_A s_1)/(\delta_A + \gamma_A s_1) \tag{2.6}$$

instead of γ_1 and determine how the region of bistability will depend on s_1 (see Fig. 2.2A). The bistability region for arbitrary $0 < s_1 < 1$ is the wedge $1 < \gamma_1^* < 1 + \kappa(1-\delta)/\delta$ (Fig. 2.2A). Since for each s_1 there is a unique line corresponding to a stationary front, we can also plot a union of all lines $\kappa(\gamma_1)$ by using Eq. (2.4) with γ_1 replaced by γ_1^* for arbitrary $0 < s_1 < 1$; this union forms a wedge shown in Fig. 2.2B. Thus, any combination of κ and γ_1 within this wedge can yield a stationary, phase-separated structure with a particular area fraction s_1^*, for which κ and $\gamma_1^*\left(s_1^*\right)$ satisfy Eq. (2.4). Similar results can be obtained in the dual-inhibition model in which both species produce and are inhibited by the same inhibitor (see Appendix).

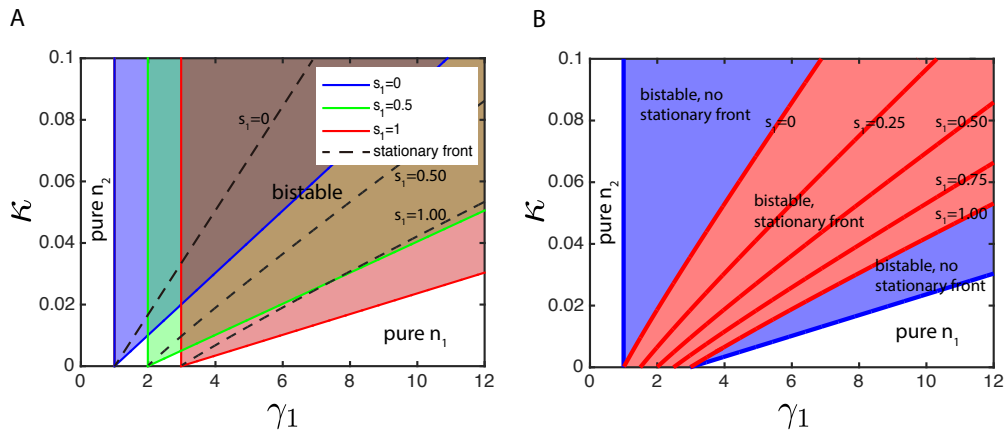

Figure 2.2: (A) Regions for bistability on (κ, γ_1) plane for three different values of strain 1 area fraction s_1. Blue wedge ($s_1 = 0$) that corresponds to $s_1 = 0$ and $A = 0$ is the same as the one for the two-variable model shown in Fig. 2.1. (B) The region of bistability for all values $0 < s_1 < 1$ (blue wedge) and the region where fronts would become stationary at specific values of s_1 (red region). Parameters are $\delta = 0.01, \gamma_A/\delta_A = 2$.

Dynamically, if the parameters κ and γ_1 fall within the domain allowing a stationary front for a certain area fraction s_1^* given by Eqs. (2.4), (2.6), but the initial area fraction of species 1 $s_1(t=0)$ is smaller than s_1^*, then n_1-domains will expand, and s_1 will increase until it becomes equal to s_1^*, at which time the expansion terminates. Conversely, if $s_1(t=0) > s_1^*$, domains of n_1 will shrink until $s_1 \to s_1^*$. This phase separation with subsequent stabilization of the total area fractions occupied by n_1 and n_2 is easily seen even when $\delta_A/\delta = O(1)$ in numerical simulations of a 2D version of this model starting from random initial conditions (Fig. 2.11). Figure 2.12 shows a comparison of the stationary state of a 1D system as predicted either analytically using Eqs. (2.4), (2.6) or with direct 1D numerical simulations of the continuum model.

Finite inhibitor diffusion

For large but finite diffusion rate D_A, the approximation of spatially-uniform A is only applicable for a sufficiently small system size $L \ll q \equiv \sqrt{D_A/\delta_A}$. In larger systems, the spatial variability of A becomes essential. Furthermore, a finite diffusion rate D_A imposes a characteristic

scale for isolated domains of n_1 and n_2. Indeed, consider an isolated island of n_1 in an infinite "sea" of n_2 in 1D (Fig. 2.3A). This island is a source of inhibitor A that gradually dissipates in the surrounding area. Thus, an island of n_1 generates a localized bump of A, whose amplitude A_0 depends on the size of the island. If the half-width of the island x_0 is much smaller than the inhibitor diffusion scale q, we can neglect the variation of A across the island and obtain the following approximate expression for A_0 valid for small qx_0 (see Appendix),

$$A_0 = \frac{\gamma_A}{\delta_A}(1-\delta/\gamma_1^*)qx_0 \tag{2.7}$$

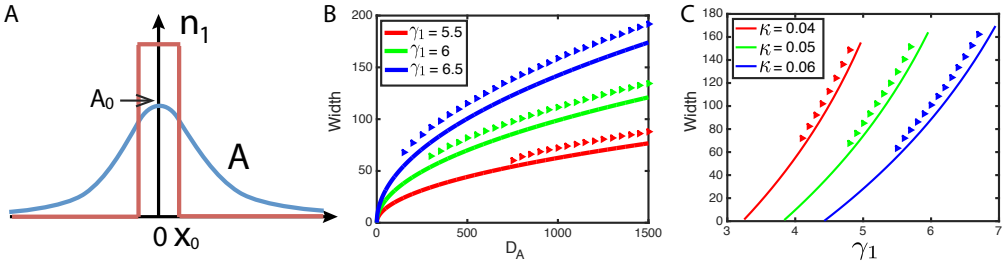

Figure 2.3: (A) A sketch showing the distribution of A produced by a spot of n_1 surrounded by the sea of n_2. (B, C) The width of an isolated spot of n_1 as a function of D_A (B) and γ_1 (C). The curves show the results from theory while the symbols are from simulations. Parameters are $\delta = 0.01$, $\delta_A = 0.02$, and $\gamma_A = 0.04$. $\kappa = 0.06$ in (B), and $D_A = 800$ in (C).

The value of A_0 depends on the size $2x_0$ of the island of n_1. For a very small island, the value of A_0 is also small, γ_1^* is large, and the island will be expanding. For a sufficiently large island, the value of A_0 is also large, the effective growth rate of n_1, γ_1^* will be small, and the island will shrink. The island will neither expand nor shrink if the value of $\gamma_1^* = \gamma_1/(1+A_0)$ satisfies Eq. (2.4), which in turn yields a solution for x_0. Comparisons between the width of an isolated spot of n_1 given by this calculation and the direct simulation are illustrated in Fig. 2.3B, C (for these plots, we used a more accurate expression for A_0 than Eq. (2.7), see Appendix). The simulation results are generally consistent with the theory; the slight deviation is due to the fact that we neglected the variation of

A and n_1 across the island. Also, in the simulations, there is a minimum size for stable stationary islands - very small islands shrink and disappear. Ref. [17] also pointed out the existence of a critical minimal size of a T6SS-sensitive domain surrounded by T6SS-active cells, but in that work, the mechanism behind it was related to the balance between the bulk growth and perimeter killing, so the bigger the domain, the greater the ratio between the area and the surrounding perimeter. In our model, the bulk growth is saturated at the maximum local density, so the balance between killing and growth is weakly dependent on the area. The existence of the critical minimum domain size is not seen in the analytical results because we neglected the width of the front between n_1 and n_2 in the theory (Fig. 2.3A). However, in our simulations, for a finite diffusion of n_1 and n_2, the interfaces have a finite width. When the size of an island becomes so small that the two finite-width fronts of the island between n_1 and n_2 overlap and annihilate each other, the island collapses.

We also performed simulations of the full 3-component deterministic model in 2D starting from random initial conditions and observed the formation of quasi-regular patterns of a characteristic size, see Fig. 2.4. Depending on the parameters (such as the strain 1 growth advantage γ_1 in the case of Fig. 2.4B), the patterns can manifest as strain 1 islands surrounded by strain 2, or vice versa. For intermediate values of γ_1, labyrinthine patterns are observed.

Turing-like instability

It is well known that an interplay of short-range activation and long-range inhibition is responsible for the onset of the Turing instability [26]. We wondered if pattern formation in our system is also the result of a Turing-like instability. Here, indeed, slowly-diffusing bacteria n_1 effectively play the role of self-activator by shielding interior cells from the killer strain n_2 and thus promoting their own growth. At the same time, the fast-diffusing field A produced by n_1 acts as an inhibitor for the growth of n_1. When the diffusion constants of activator and inhibitor are sufficiently different, the Turing mechanism manifests itself in the linear instability of a uniform state with

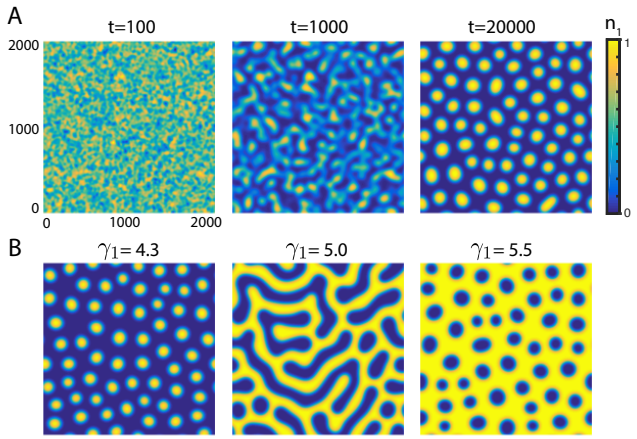

Figure 2.4: Pattern formation in a deterministic model with finite $D_A = 80$ and random initial conditions. (A) Three snapshots of n_1. (B) Snapshots at time $t = 40000$ for different γ_1. $\gamma_1 = 4.5$ in (A) and other parameters: $\delta = 0.01$, $\kappa = 0.03$, $\gamma_A = 0.04$, $\delta_A = 0.02$.

respect to small spatially-periodic perturbations with finite wavenumbers. To test whether our system indeed exhibits Turing-like instability, we linearized the full model Eqs. (2.1)-(2.3) near the mixed state and computed the eigenvalues of spatially-periodic perturbations. We indeed found that for certain parameter values, the mixed state is linearly unstable with respect to finite-wavenumber perturbations (Appendix).

Figure 2.5A shows the region corresponding to the Turing-like instability in the (κ, γ_1) plane for fixed $\delta, \gamma_A, \delta_A$ and finite D_A, along with the theoretical lines limiting the region for stationary fronts in the case of infinite D_A, as shown as the red sector in Fig. 2.2B. As explained above, the existence of such fronts leads to stable pattern formation. The heatmap indicates the values of the wavenumber corresponding to the maximum positive eigenvalue. The Turing-like instability region lies inside the domain allowing stationary fronts, but it is much narrower. Similarly, the region for stable pattern formation obtained numerically from the full nonlinear model Eqs. (2.1)-(2.3) for finite inhibitor diffusion is significantly wider than the corresponding Turing-like instability domain (Fig. 2.5B). These results suggest that pattern formation in this system is more robust and easily observable phenomenon than linear Turing-like instability of a well-mixed state. While the

Turing-like instability can indeed initiate morphogenesis in this system, the patterns can emerge and stabilize in a much broader range of system parameters due to nonlinearity of the system. In fact, our numerical simulations show that patterns emerge spontaneously if the two strains are initially well-separated (there are sufficiently large regions where $n_1 \gg n_2$ or $n_2 \gg n_1$).

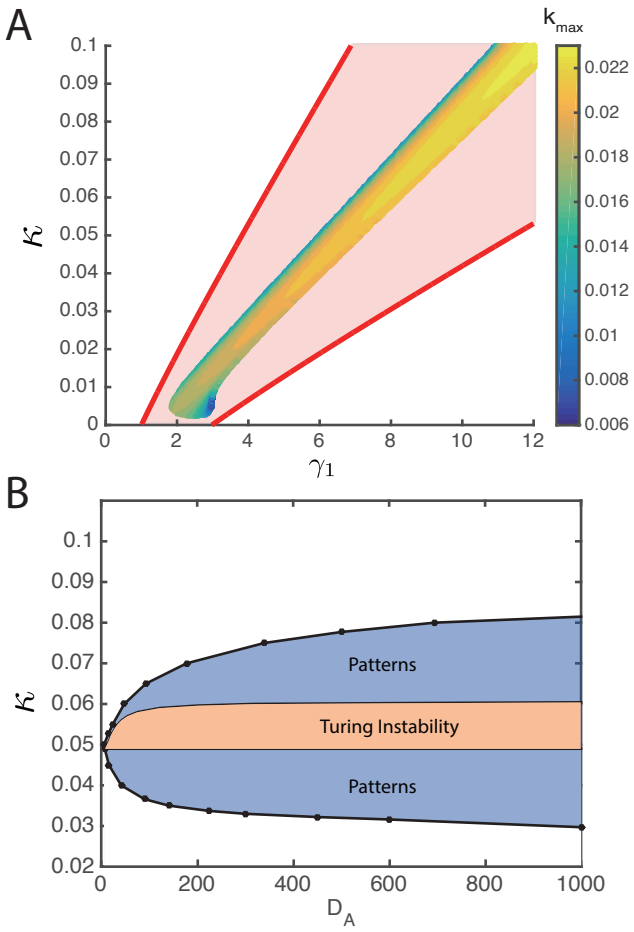

Figure 2.5: The region of the linear Turing-like instability in the $\kappa - \gamma_1$ (A) and $\kappa - D_A$ (B) parameter planes. (A) The heatmap depicts the wavenumber k_{max} corresponding to the maximal positive eigenvalue for the Turing-like instability for $D_A = 500$. The red lines limit the region with stationary fronts and pattern. The parameter values: (A) $D_A = 500$, (B) $\gamma_1 = 7$. Other parameters, $\delta = 0.01, \gamma_A = 0.04, \delta_A = 0.02$, are the same for both panels.

2.3.2 Discrete stochastic model

As described in the previous section, the 3-component continuum model for the two slowly-diffusing bacterial densities and one fast-diffusing growth inhibitor exhibits a pattern-forming Turing-like instability. However, numerical simulations show that stable patterns can exist in a much wider parameter range. We identified a nonlinear mechanism of pattern formation that is based on interface stabilization due to the self-consistent changes in the growth caused by the fast-diffusing inhibitor. This raises the question of how such well-separated states can emerge from an unpatterned initial condition, if it is linearly stable. We note, however, that in an actual experiment, relatively dilutely inoculated mixtures would initially grow in conditions that are actually very different from the spatially-uniform, well-mixed state that is typically assumed in deterministic reaction-diffusion models. If a mixture was inoculated as a smattering of isolated bacteria that initially have no direct contact, then bacteria of both types would grow for some time unimpeded by interaction with bacteria of the other type until they form micro-colonies that are large enough when they begin contacting each other. This scenario can lead to pattern formation even when the uniformly mixed state is linearly stable.

We used a lattice-based discrete-element model introduced in Methods to simulate this scenario. The simulation results from this model are illustrated by three snapshots of n_1 and n_2 in Fig. 2.13A. The initial condition for this simulation was a "dilute mixture" of both strains, so on average only 10% of lattice sites were occupied, and typically by no more than a single cell of either type. As seen from the figure, this initial condition eventually gives rise to a patterned state in which spots of n_1 are surrounded by a "sea" of n_2. A characteristic size of the pattern emerges, as evidenced by the narrow-peaked area distribution of n_1 spots (Fig. 2.13B). If either inhibitor production is disabled ($\gamma_A = 0$) or neighbor-killing is turned off ($\kappa = 0$), patterns do not form, and either n_1 or n_2 takes over the whole system while the other species is driven to extinction unless the system parameters are tuned precisely to satisfy the balance condition similar to Eq. (2.4) (results

are not shown).

To evaluate the range of parameters in which patterns spontaneously emerge from a dilute initial state, we ran a series of discrete stochastic simulations with a range of values of γ_1 and κ. Again, the initial condition were randomly distributed n_1 and n_2 cells at low concentration. In agreement with the continuum theory, in the bulk of the region where the existence of stable patterns was expected, the patterns indeed spontaneously emerged, see Fig. 2.6. As seen from this figure, depending on the relative growth advantage of the type-1 strain and the killing efficiency of the type-2 strain, the patterns change their structure: for smaller γ_1/γ_2 or larger κ, they appear as isolated islands of n_1 surrounded by n_2. For large growth advantage of the type-1 strain or small κ, the patterns are reversed: the islands of n_2 are surrounded by the sea of n_1. In the intermediate range, we found more symmetric labyrinthine patterns. We also characterized the observed patterns by the average fraction of n_1 vs. n_2 and the power spectrum of the spatial distribution of n_1 (Fig. 2.14).

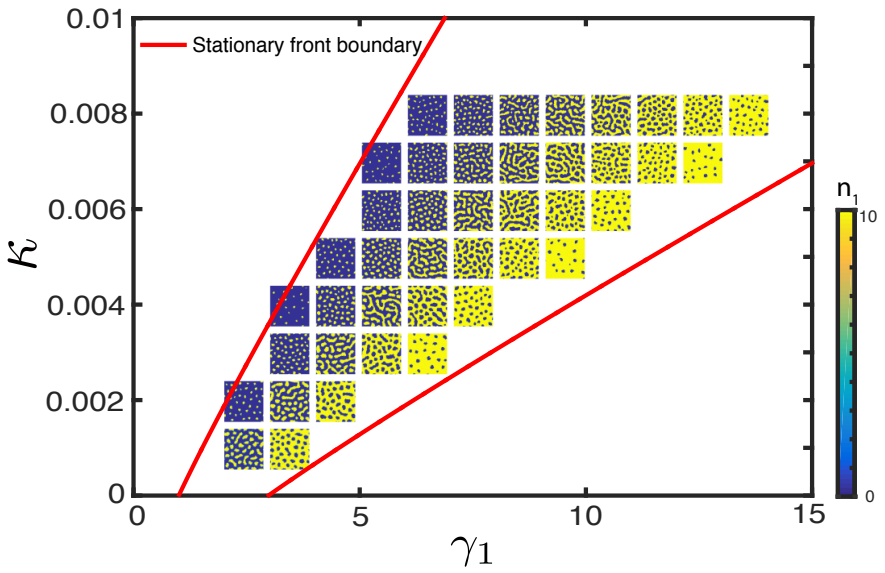

Figure 2.6: Typical patterns emerging from random initial conditions in stochastic simulations for different values of parameters κ and γ_1. Other parameters are: $\gamma_2 = 1, n_0 = 10, \delta = 0.01, \delta_A = 0.02, \gamma_A = 0.004, P_n = 0.1, D_A = 12.5$. The system size is 256×256. Because the number of cells must be integers in stochastic simulations, we use unscaled parameters here.

2.4 Discussion

Ecological diversity is ubiquitous in nature, ranging in scale from the ecosystems that cover our planet to the microbiome that inhabits our gut. Diversity plays an important role in maintaining the functions of an ecosystem; e.g., the gut microbiome provides many health benefits to its host [27, 28, 29, 30]. However, the conditions and mechanisms that robustly stabilize this biodiversity are still unclear. To study and explain the coexistence of different species within a community, several models have been proposed, such as the rock-paper-scissors game models [31, 32, 33, 34]. On the other hand, in synthetic biology, stabilization of multi-strain microbial communities has proven to be a challenge [35]. One recent example of ongoing efforts in this direction is a stable co-culture of two different strains with different growth rates in microfluidic chips using synthetic population control gene circuit [36].

Previous modeling studies of multi-strain coexistence used population dynamics equations similar to our work. Frank [37] studied the dynamics of bacteriocin producers killing susceptibles and found that only when the habitat was spatially heterogeneous, could the two species coexist. His results can also be readily applied to other mechanisms of contact-dependent killing. In another work, Durrett and Levin [31] studied two-species interactions via colicins and showed that in spite of bistability of well-mixed populations, in a spatially-structured population only one "stronger" strain will eventually win depending on system parameters; i.e., neither bistability, nor coexistence occurs. This was consistent with previous experimental results [38]. On the other hand, Iwasa et al. [39] showed that in relatively small stochastic lattice-type models, a narrow parameter region of bistability may exist, but still without coexistence. Blanchard et al. [19] studied the interaction of two bacterial strains in the presence of contact-dependent killing using a reaction-diffusion-type model and correctly predicted the emergence of bistability that may in principle lead to coexistence of the strains. They also showed through numerical simulations that fronts separating two strains can remain static in a finite parameter range if the diffusion of bacteria is slow enough. However,

this latter result has to be taken with the grain of salt because front stabilization in finite-difference simulations may come from pinning. The phenomenon of front pinning in systems with periodic or random inhomogeneities has been studied previously [40, 41, 42, 43, 44]. Discretization of a continuous reaction-diffusion model in finite-difference numerical integration provides such periodic structure that can stop slowly moving fronts [45, 46]. In our simulations, to minimize pinning artifacts, we used high spatial resolution (512-1024 nodes) and relatively large diffusion constant for bacteria $D_n = 1$. We also verified our simulations by increasing spatial resolution and comparing the results to analytical predictions. The results shown in Fig. 2.1 demonstrate that our simulations are indeed consistent with continuum theory. However, if we artificially decrease spatial resolution and reduce the diffusion constant in our simulations, we immediately begin to see prominent pinning effects. We performed numerical simulations of the two-variable model (without long-range inhibition) for small bacterial diffusion $D_n = 0.01$ and different numbers of grid points N_g. Some results of these simulations are shown in Appendix (Fig. 2.15). For example, for $N_g = 128$ nodes and a certain value of γ_1, there is a large finite range of κ at which the fronts are stationary, but this range becomes progressively smaller as the number of nodes increases toward the values used in our work.

The coexistence of different species creates the possibility of the emergence of regular patterns. One example is a spiral pattern in the rock-paper-scissors model [34]. The balance of local activation and global inhibition has been used to explain many forms of pattern formation, such as self-organized patchiness in ecosystems [47]. In another study, nutrient competition and mechanical pushing can drive the occurrence of spatial patterns that can also cycle through hole, labyrinth, and spot patterns [48]. The mechanical pushing plays the role of local activation, and nutrient competition assumes the task of global inhibition.

In this paper, we demonstrated that a combination of short-range killing with long-range growth inhibition may lead to stable coexistence and pattern formation in mixtures of T6SS-

sensitive and T6SS-active bacteria. In the absence of either one of these two mechanisms, one of the two strains eventually takes over, and no stable spatial patterns form. While the mechanism of pattern formation is similar to the Turing instability, the parameter region for stable coexistence and pattern formation is much broader than the range of the linear Turing-like instability of the uniform mixed state. Thus, in a broad parameter range, the stable patterns may co-exist with stable uniform states, and the final outcome depends on the initial conditions. If cells of both types are initially well separated, the system evolves towards stable patterns. In experiments, this would correspond to an initially dilute bacterial inoculum where individual cells are not in direct contact, allowing them to develop into patches (micro-colonies) before making contact with each other. We performed simulations of a lattice-based discrete stochastic model that incorporates cell growth, death, diffusion, neighbor killing and growth inhibition, and indeed found that patterns emerge spontaneously from an initially dilute state for a broad range of parameters, as predicted by the theory.

In our continuous model, the motion of bacterial cells is described by diffusion terms. In reality, bacterial cells do not simply diffuse like Brownian particles. For example, T6SS-sensitive motile *E. coli* cells perform a run-and-tumble random walk, and T6SS-active bacteria *A. baylyi* move on agar surface through twitching using their pili [49]. Furthermore, when bacteria form dense communities such as biofilms, cells push each other, and so mechanical stress plays an important role in cell motility and overall colony organization [50, 51, 52]. In addition, cell motion and growth of real biofilms are affected by cell-cell adhesion and secretion of extracellular matrix [53]. None of these factors are included explicitly in our model. Instead, we use diffusion as a simple but reasonable approximation of the cell motility, as many researchers have done previously [54, 55, 56, 57]. In our stochastic lattice model, the cells can jump to neighboring sites only if there is room there. Still, the results of our stochastic simulations are consistent with the theory and simulations of the deterministic continuum model.

While we only presented theoretical results here, we anticipate that the mechanism of pattern formation described in this paper operates in nature and can be observed in the laboratory. Compared to the Turing instability, this mechanism can produce stable patterns in a much wider parameter range, likely making it easier for experimental verification. In our system, it requires that the T6SS-sensitive bacteria grow faster than T6SS-active ones ($\gamma_1 > 1$) and the killing rate κ is small. These conditions are not difficult to fulfill. Different bacteria exhibit vastly different growth rates and abilities to metabolize different carbon sources [58, 59, 60]. For example, in our preliminary experiments, the growth rate of T6SS-sensitive *E. coli* was found to be significantly faster than T6SS-active *A. baylyi*. In the laboratory, we can also vary growth rates by changing carbon sources and/or adding sublethal amounts of antibiotics that selectively slow down growth of different species. The ability of T6SS-active bacteria to kill their neighbors also varies greatly by both the predator and the prey. For example, of three T6SS-active species, *A. baylyi* can kill *V. cholerae*, while *A. baylyi* itself succumbs to *Pseudomonas aeruginosa* [61]. According to the same study, the T6SS killing rates of these strains are comparable to their division rates if predator and prey cells maintain prolonged contact. However, motile cells are unlikely to have prolonged contacts, so the effective killing rate may be significantly smaller. Furthermore, in laboratory environments, one could tune killing rates in a broad range by knocking out certain T6SS toxic effectors [62], placing key components of the T6SS under an inducible promoter in the predator, or by placing an immunity gene under an inducible promoter in the prey. The death rate used in our model is of the order of 0.01 compared with the growth rate which is typical in reality [63].

Our model also requires bacteria to produce a long-range inhibitor. As mentioned above, production of fast-diffusing waste or consumption of fast-diffusing nutrients could provide a native mechanism of long-range inhibition. Since bacteria vary in their ability to utilize different carbon sources, it is likely that the degree of growth inhibition within a pair of strains would also differ. However, long-range inhibition could be also forward-engineered using synthetic biology [24]. For

example, *E. coli* could be endowed with an antibiotic resistance gene controlled by a promoter repressed by a quorum-sensing signal, such as AHL produced by a constitutively expressed AHL-synthase LuxI [64, 65]. If we add that antibiotic to the media, then as *E. coli* grow and produce more and more AHL, which represses the antibiotic resistance gene, the growth of *E. coli* colonies would gradually slow down. The T6SS-active strain (*A. baylyi*) could be made immune to this antibiotic by constitutively expressing the same resistance gene. Another possible candidate for such long-range inhibitor is colicin, a type of bacteriocin. Some wild type *E. coli* can produce colicins against closely related bacteria [66, 67, 68], but they themselves are usually not affected by their own colicin so long as they express an immunity gene [67]. If that immunity gene was knocked out, fast-diffusing colicins would inhibit the growth of *E. coli*.

2.5 Acknowledgements

We thank Igor Aranson, Philip Bittihn, and Jeff Hasty for helpful discussions. This work was supported by the National Institutes of Health grant R01-GM069811, San Diego Center for Systems Biology (NIH grant P50-GM085764) and the Office of Naval Research (grant N00014-16-1-2093).

Chapter 2 contains material originally published as Xiong, L., Cooper, R. and Tsimring, L.S., 2018. Coexistence and pattern formation in bacterial mixtures with contact-dependent killing. *Biophysical Journal*. The dissertation author was the primary investigator of this paper.

2.6 Appendix

2.6.1 Analysis of the two-strain model

We consider the interaction of two strains of bacteria, fast-growing strain 1 with local density $n_1(\mathbf{r},t)$ and slow-growing strain 2 with local density $n_2(\mathbf{r},t)$. The growth of both strains is limited

by the total local density of bacteria, so when n_1+n_2 approaches n_0, the growth of both strains saturates. Both strains are characterized by the same death rate δ. Additionally, strain 2 kills strain 1 on direct contact with the rate κ. Both strains are assumed to diffuse horizontally with the same small diffusion constant D_n. The model reads as follows

$$\frac{\partial n_1}{\partial t} = \gamma_1 n_1(1-\frac{n_1+n_2}{n_0}) - \delta n_1 - \kappa n_1 n_2 + D_n \nabla^2 n_1 \tag{2.8}$$

$$\frac{\partial n_2}{\partial t} = \gamma_2 n_2(1-\frac{n_1+n_2}{n_0}) - \delta n_2 + D_n \nabla^2 n_2 \tag{2.9}$$

In the following, we assume that all parameters $\gamma_1, \gamma_2, \delta, \kappa, D_n, n_0$ are positive. Without loss of generality, we can rescale time $\tilde{t} = \gamma_2 t$, space $\tilde{x} = (\gamma_2/D_n)^{1/2} x$, and densities, $\tilde{n} = n/n_0$, so in rescaled variables $\tilde{\gamma}_2 = 1, \tilde{\gamma}_1 = \gamma_1/\gamma_2, \tilde{\delta} = \delta/\gamma_2, \tilde{\kappa} = \kappa n_0/\gamma_2, \tilde{D}_n = 1$. For simplicity, in the following we will drop tildas and keep the same notation for the rescaled variables and parameters:

$$\frac{\partial n_1}{\partial t} = \gamma_1 n_1(1-n_1-n_2) - \delta n_1 - \kappa n_1 n_2 + \nabla^2 n_1 \tag{2.10}$$

$$\frac{\partial n_2}{\partial t} = n_2(1-n_1-n_2) - \delta n_2 + \nabla^2 n_2 \tag{2.11}$$

Spatially uniform steady states and their stability. This system has four steady states:

1. $n_1 = 1-\frac{\delta}{\gamma_1}, n_2 = 0.$
2. $n_1 = 0, n_2 = 1-\delta.$
3. $n_1 = 1-\delta-\frac{\delta}{\kappa}(\gamma_1-1), n_2 = \frac{\delta}{\kappa}(\gamma_1-1).$
4. $n_1 = n_2 = 0.$

The Jacobian matrix is

$$J = \begin{pmatrix} a_{11} & a_{12} \\ a_{21} & a_{22} \end{pmatrix}$$

with

$$a_{11} = \gamma_1(1-2n_1-n_2)-\delta-\kappa n_2 \tag{2.12}$$

$$a_{12} = -\gamma_1 n_1 - \kappa n_1 \tag{2.13}$$

$$a_{21} = -n_2 \tag{2.14}$$

$$a_{22} = 1-n_1-2n_2-\delta \tag{2.15}$$

Steady state 1 has eigenvalues $\lambda_1 = \delta-\gamma_1, \lambda_2 = (\frac{1}{\gamma_1}-1)\delta$. When $\gamma_1 > \delta, 1$, it is stable and $n_1 > 0$. Steady state 2 has eigenvalues $\lambda_1 = (\gamma_1-1)\delta-\kappa(1-\delta), \lambda_2 = \delta-1$. When $\delta < 1$ and $\kappa > \kappa_b = \frac{\delta(\gamma_1-1)}{1-\delta}$, it is stable and $n_2 > 0$. Steady state 3 is positive when $\gamma_1 > 1$, $\delta < 1$ and $\kappa > \kappa_b$ but is unstable. Trivial steady state 4 is unstable if $\gamma_1 > \delta$ or $\delta < 1$.

The system is bistable in the range

$$1 < \gamma_1 < 1 + \frac{\kappa(1-\delta)}{\delta} \tag{2.16}$$

Stationary front in two-variable model. In the bistable regime, there may exist fronts separating colonies of strains 1 and 2. These fronts generally move in either direction depending on the system parameters. Generally, if $\gamma_1 > 1$, for very small killing rate κ, strain 1 always wins, and the front propagates in the direction of strain 2, while for sufficiently large κ the front reverses. There is a unique value of $\kappa_s = \kappa(\gamma_1, \delta)$ at which the front is stationary. This value of κ_s can be found approximately for small δ and κ, when $n_1 + n_2$ is close to 1 using the Maxwell rule known in

thermodynamics.

In the following we assume that $\kappa = \varepsilon K$, $\delta = \varepsilon\Delta$ with $\varepsilon \ll 1$, and introduce new variables

$$N = \varepsilon^{-1}(n_1 + n_2 - 1), \;\; \xi = n_1 - n_2. \tag{2.17}$$

Conversely, $n_1 = (1+\varepsilon N + \xi)/2, n_2 = (1+\varepsilon N - \xi)/2$. In the new variables and in the first order in ε, Eqs. (2.10),(2.11) can be rewritten as

$$\begin{aligned} \partial_t N &= -\frac{N}{2}(\gamma_1+1) - \frac{N}{2}(\gamma_1-1)\xi - \Delta - \frac{K}{4}(1-\xi^2) + \nabla^2 N, & (2.18)\\ \varepsilon^{-1}\partial_t \xi &= -\frac{N}{2}(\gamma_1-1) - \frac{N}{2}(\gamma_1+1)\xi - \Delta\xi - \frac{K}{4}(1-\xi^2) + \varepsilon^{-1}\nabla^2\xi. & (2.19) \end{aligned}$$

The first equation describes fast relaxation toward the solution

$$N = -\frac{2\left(\Delta + \frac{K}{4}(1-\xi^2)\right)}{\gamma_1 + 1 + \xi(\gamma_1 - 1)}. \tag{2.20}$$

Assuming that the fast initial relaxation has occurred, and N is slaved to slow variably ξ, we can substitute N from Eq. (2.20) in Eq. (2.19). Returning to the original parameters κ and δ, after simple algebra we get a single reaction-diffusion equation for the slow dynamics of ξ,

$$\partial_t \xi = f(\xi) + \nabla^2 \xi, \tag{2.21}$$

where

$$f(\xi) = \delta \frac{1-\xi^2}{1+\Gamma\xi}\left[\Gamma + (\Gamma - 1)(1-\xi)\frac{\kappa}{4\delta}\right] \tag{2.22}$$

with $\Gamma = (\gamma_1 - 1)/(\gamma_1 + 1)$. For small δ and κ, this equation describes slow front propagation. Function $f(\xi)$ has two roots $\xi_{1,2} = \pm 1$ corresponding to stable fixed points of Eq. (2.21), and an intermediate root at $\Gamma + (\Gamma - 1)(1-\xi)\frac{\kappa}{4\delta} = 0$ corresponding to an unstable fixed point. Maxwell

rule states that a front solution of the 1-D reaction-diffusion equation (2.21) connecting stable fixed points ξ_1 and ξ_2 is stationary if $\int_{\xi_1}^{\xi_2} f(\xi)d\xi = 0$.

For $\Gamma \ll 1$, we can drop $\Gamma\xi$ in the denominator of (2.22). Then it becomes a cubic polynomial, and it is evident that the integral will be zero if $f(\xi)$ is anti-symmetric with respect to zero, i.e. when intermediate root is $\xi = 0$, or $\Gamma + (\Gamma - 1)\frac{\kappa}{4\delta} = 0$, which gives

$$\frac{\kappa}{\delta} = 2(\gamma_1 - 1). \tag{2.23}$$

For finite Γ, integration of the full function (2.22) yields the following expression for the ratio κ/δ at which the front is stationary,

$$\frac{\kappa}{\delta} = \frac{3(\gamma_1 - 1)^2(\gamma_1^2 - 1 - 2\gamma_1 \ln \gamma_1)}{2\gamma_1^3 + 3\gamma_1^2 - 6\gamma_1 + 1 - 6\gamma_1^2 \ln \gamma_1}. \tag{2.24}$$

It is easy to check that expression (2.24) reduces to (2.23) for small $\gamma_1 - 1$.

2.6.2 Analysis of the three-variable model

The full model with long-range inhibition reads as follows

$$\frac{\partial n_1}{\partial t} = \frac{\gamma_1}{1 + A/A_0} n_1 \left(1 - \frac{n_1 + n_2}{n_0}\right) - \delta n_1 - \kappa n_1 n_2 + D_n \nabla^2 n_1, \tag{2.25}$$

$$\frac{\partial n_2}{\partial t} = \gamma_2 n_2 \left(1 - \frac{n_1 + n_2}{n_0}\right) - \delta n_2 + D_n \nabla^2 n_2, \tag{2.26}$$

$$\frac{\partial A}{\partial t} = \gamma_A n_1 - \delta_A A + D_A \nabla^2 A. \tag{2.27}$$

Use the same scaling as above and $\tilde{A} = A/A_0, \tilde{\gamma}_A = \gamma_A n_0/(\gamma_2 A_0), \tilde{\delta}_A = \delta_A/\gamma_2, \tilde{D}_A = D_A/D_n$, we have

$$\frac{\partial n_1}{\partial t} = \frac{\gamma_1}{1+A} n_1(1-n_1-n_2) - \delta n_1 - \kappa n_1 n_2 + \nabla^2 n_1 \tag{2.28}$$

$$\frac{\partial n_2}{\partial t} = n_2(1-n_1-n_2) - \delta n_2 + \nabla^2 n_2 \tag{2.29}$$

$$\frac{\partial A}{\partial t} = \gamma_A n_1 - \delta_A A + D_A \nabla^2 A \tag{2.30}$$

where we again drop tildes for simplicity of notation.

Bifurcation analysis of the spatially uniform steady states. Full three-variable system possesses at most 5 real spatially uniform steady states:

1. $n_1 = \frac{\gamma_1 - \delta}{\frac{\delta\gamma_A}{\delta_A} + \gamma_1}, n_2 = 0, A = \frac{\gamma_1 - \delta}{\delta + \frac{\gamma_1 \delta_A}{\gamma_A}}$.
2. $n_1 = 0, n_2 = 1 - \delta, A = 0$.
3. $n_1 = \frac{-b + \sqrt{b^2 - 4ac}}{2a}, n_2 = 1 - n_1 - \delta, A = \frac{\gamma_A}{\delta_A} n_1$ where $a = \frac{\kappa\gamma_A}{\delta_A}, b = \kappa - \frac{\gamma_A}{\delta_A}[\delta + \kappa(1-\delta)], c = (\gamma_1 - 1)\delta - \kappa(1-\delta)$.
4. $n_1 = \frac{-b - \sqrt{b^2 - 4ac}}{2a}, n_2 = 1 - n_1 - \delta, A = \frac{\gamma_A}{\delta_A} n_1$ where a, b, c are the same as those in steady state 3.
5. $n_1 = 0, n_2 = 0, A = 0$.

The Jacobian matrix for the system is

$$J = \begin{pmatrix} a_{11} & a_{12} & a_{13} \\ a_{21} & a_{22} & a_{23} \\ a_{31} & a_{32} & a_{33} \end{pmatrix}$$

with

$$
\begin{aligned}
a_{11} &= \frac{\gamma_1}{1+A}(1-2n_1-n_2)-\delta-\kappa n_2 \\
a_{12} &= -\frac{\gamma_1}{1+A}n_1-\kappa n_1 \\
a_{13} &= -\frac{\gamma_1}{(1+A)^2}n_1(1-n_1-n_2) \\
a_{21} &= -n_2 \\
a_{22} &= 1-n_1-2n_2-\delta \\
a_{23} &= 0 \\
a_{31} &= \gamma_A \\
a_{32} &= 0 \\
a_{33} &= -\delta_A .
\end{aligned}
$$

The trivial fixed point 5 is always unstable, and we will not consider it below. The steady states of n_1, n_2 vs. κ with their stability are illustrated in Fig. 2.7(A),(B). When γ_1 is smaller than a threshold γ_{1c}, steady states 3 and 4 always exist although steady state 3 is non-physical in this case (it corresponds to negative n_2) [Fig. 2.7(C) left]. At the critical value $\gamma_1 = \gamma_{1c}$, a codimension-2 bifurcation occurs when steady state 2 overlaps with steady states 3 and 4 and two saddle-node bifurcation points emerge [Fig. 2.7(C) middle]. When $\gamma_1 > \gamma_{1c}$, there are two isolated saddle-node bifurcation points in which steady states 3 and 4 merge and disappear [Fig. 2.7(C) right].

The condition for the saddle-node bifurcation is $b^2 - 4ac = 0$, which leads to the equation for bifurcation values of $\kappa = \kappa_s$,

$$
[1+\frac{\gamma_A}{\delta_A}(1-\delta)]^2\kappa_s^2 - 2\frac{\gamma_A\delta}{\delta_A}[2\gamma_1 - 1 - \frac{\gamma_A}{\delta_A}(1-\delta)]\kappa_s + \left(\frac{\gamma_A\delta}{\delta_A}\right)^2 = 0, \tag{2.31}
$$

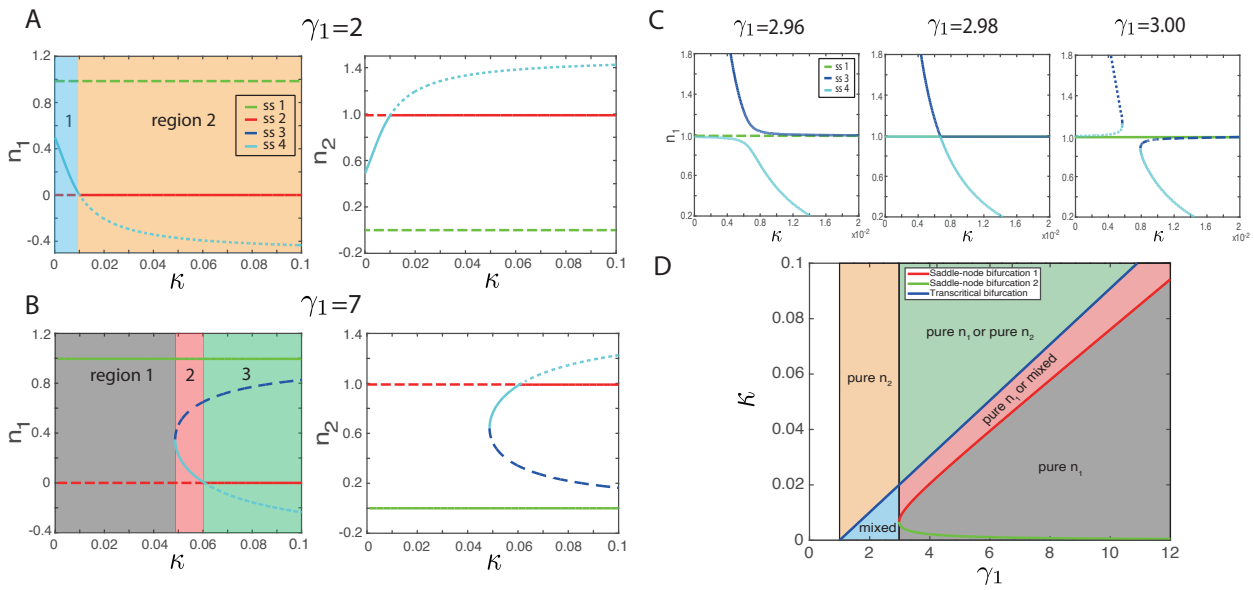

Figure 2.7: (A),(B) Steady states of n_1 and n_2 for different γ_1 and κ. Solid lines correspond to stable solutions, long-dashed to unstable solutions, and short-dashed to non-physical steady states for which either n_1 or n_2 are negative. (C) Codimension-2 bifurcation at $\gamma_{1c} = 2.98$. when two saddle-node bifurcation points are born at certain γ_1 and κ and pure solution $n_1 \neq 0, n_2 = 0$ changes stability. (D) Domains of different stable steady states in the (γ_1, κ) parameter plane. Other parameters: $\delta = 0.01, \gamma_A = 0.04, \delta_A = 0.02$.

and thus

$$\kappa_{s\pm} = \frac{\gamma_A \delta}{\delta_A} \left\{ \frac{2\gamma_1 - 1 - \frac{\gamma_A}{\delta_A}(1-\delta) \pm 2\sqrt{\gamma_1^2 - \gamma_1[1 + \frac{\gamma_A}{\delta_A}(1-\delta)]}}{[1 + \frac{\gamma_A}{\delta_A}(1-\delta)]^2} \right\}. \tag{2.32}$$

From Eq. (2.32), it can be shown that $\kappa_{s\pm}$ are real only when

$$\gamma_1 > \gamma_{1c} = 1 + \frac{\gamma_A}{\delta_A}(1-\delta). \tag{2.33}$$

We also notice that there is a transcritical bifurcation between steady states 2 and 4 [Fig. 2.7(A)(B)]. At the transcritical bifurcation point, $n_1 = 0$ which leads to $c = 0$, and thus

$$\kappa = \kappa_t = \frac{\delta(\gamma_1 - 1)}{1 - \delta}. \tag{2.34}$$

It is worth mentioning that if $b > 0$ at $\kappa = \kappa_{s_+}$, the saddle-node bifurcation between steady states 3 and 4 happens at $n_1 < 0$, and then the transcritical bifurcation occurs between steady states 2 and 3 instead of 2 and 4 (an example is shown in Fig. 2.8). In this case, region 2 in Fig. 2.7(B) disappears, and only regions 1 and 3 remain.

Domains in the parameter plane (γ_1, κ) corresponding to different spatially-uniform stable steady states are shown in Fig. 2.7(D).

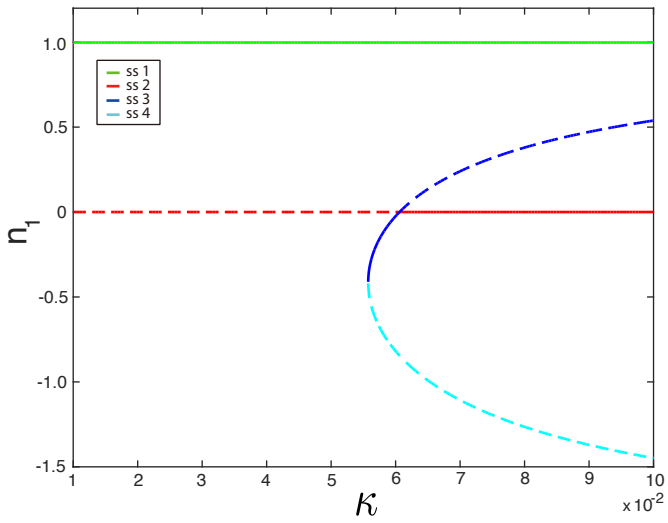

Figure 2.8: For sufficiently large γ_1 and small γ_A, the saddle-node bifurcation between steady states 3 and 4 moves to (non-physical) negative n_1, and the transcritical bifurcation occurs between steady states 2 and 3. Parameters: $\gamma_1 = 7, \gamma_A = 0.01$, other parameters are the same as in Fig. 2.7.

Localized spot of $\mathbf{n_1}$. Here we find an approximate solution for the width of a stationary spot of n_1 surrounded by the sea of n_2, when the diffusion coefficient of A is large but finite. For that we need to compute the distribution of A produced by such a spot, and find at which spot size the level of A within the spot is such that the interfaces between n_1 and n_2 are stationary. To compute the stationary distribution of A we use Eq. (2.30) with $\partial_t A = 0$,

$$\gamma_A n_1 - \delta_A A + D_A \nabla^2 A = 0. \tag{2.35}$$

We consider only the 1D case here, but the generalization to 2D is straightforward. We assume that the spot size is much larger than the width of the interfaces separating n_1 and n_2 (which is of the order of $(D_n/\gamma_1)^{1/2}$), but much smaller than the diffusive scale of the inhibitor $q = (\delta_A/D_A)^{1/2}$, and so the spot can be approximated by a rectangular "pulse" with constant $n_1 \approx n_{1*} = 1-\delta(1+A(0))/\gamma_1$ for $-x_0 < x < x_0$ and zero outside (see Fig. 2.3A). Solving the Poisson equation (2.35) in these two domains and matching A and dA/dx at $x = \pm x_0$, we obtain the following solution for $A(x)$:

$$A(x) = \begin{cases} \frac{\gamma_A}{\delta_A} n_{1*}(1 - e^{-qx_0}\cosh(qx)), & -x_0 < x < x_0 \\ \frac{\gamma_A}{\delta_A} n_{1*} \frac{e^{qx_0} - e^{-qx_0}}{2} e^{-q|x|}, & |x| > x_0 \end{cases} \tag{2.36}$$

Substituting $n_{1*} = 1-\delta(1+A(0))/\gamma_1$ in Eq. (2.36) and take $x = 0$, we can obtain $A(0)$ explicitly,

$$A(0) = \frac{\frac{\gamma_A}{\delta_A}\left(1 - \frac{\delta}{\gamma_1}\right)\left(1 - e^{-qx_0}\right)}{1 + \frac{\gamma_A \delta}{\gamma_1 \delta_A}\left(1 - e^{-qx_0}\right)} \tag{2.37}$$

The value of A at the front is

$$A(x_0) = \frac{\frac{\gamma_A}{\delta_A}\left(1 - \frac{\delta}{\gamma_1}\right)\left(1 - e^{-qx_0}\cosh(qx_0)\right)}{1 + \frac{\gamma_A \delta}{\gamma_1 \delta_A}\left(1 - e^{-qx_0}\right)} \tag{2.38}$$

For large inhibitor diffusion, $qx_0 \ll 1$, the difference between $A(0)$ and $A(x_0)$ is small, these expressions can be further simplified to

$$A(0) \approx A(x_0) \approx \frac{\gamma_A}{\delta_A}\left(1 - \frac{\delta}{\gamma_1}\right) qx_0, \tag{2.39}$$

which shows that for small x_0 the magnitude of A bump is proportional to x_0, as expected. The spot will be neither expanding nor shrinking if the value of $\gamma_1^* = \gamma_1/(1+A(x_0))$ with $A(x_0)$ from (2.38) satisfies Eq. (2.24), which yields the equation for x_0.

Turing-like instability. To explore the possibility of a linear Turing-like instability in our three-component system, we linearized Eqs. (2.28)-(2.30) near relevant fixed points and studied the eigenvalues corresponding to spatially-periodic perturbations $\sim \exp(ikx+\lambda t)$. Each fixed point has three eigenvalues. Fig. 2.9 shows three examples of maximal eigenvalues of relevant steady states in different parameter regions [regions 1, 2 and 3 in Fig. 2.7(B)] vs. wave number k. The middle panel ($\kappa = 0.053$) indeed demonstrates the occurrence of the Turing-like instability when steady state 4 is unstable with respect to small perturbations within a finite range of wavenumbers. The right panel ($\kappa = 0.07$) shows the situation when the fixed point is unstable with respect to spatially uniform as well as spatially-periodic perturbations, but the maximal growth rate occurs at a finite wavenumber. Our numerical simulations show that stable patterns are also possible in this parameter range.

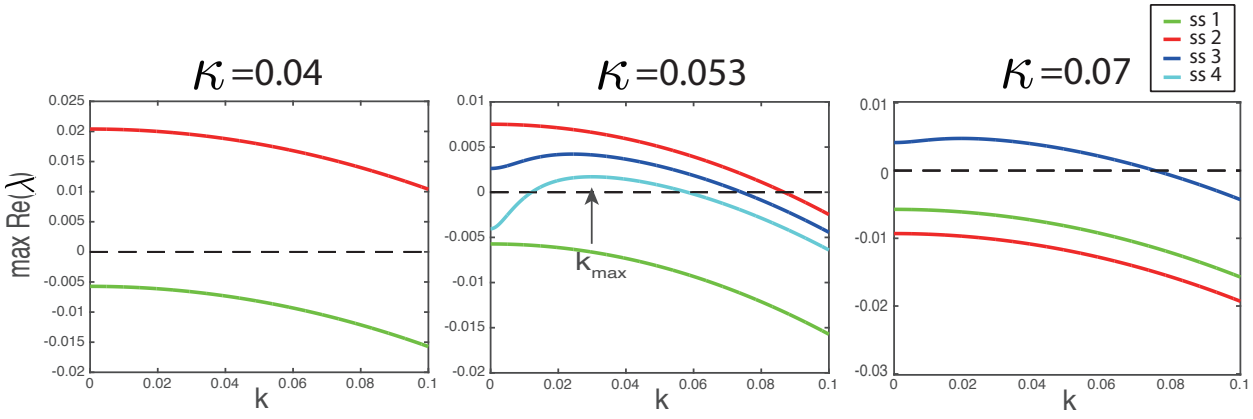

Figure 2.9: Maximal real parts of eigenvalues of different steady states in different regions (regions 1, 2 and 3) in Fig. 2.7(B) vs. wave number k. Parameters are $\gamma_1 = 7, \delta = 0.01, \gamma_A = 0.04, \delta_A = 0.02, D_A = 100$.

2.6.3 Dual-inhibition model

To formulate the model considered in the Main text, we assumed that the long-range inhibitor A was only produced by the T6SS-sensitive strain, and only affected its own growth. To generalize this model, here we assume that A is produced by both n_1 and n_2 and it also can inhibit the growth

rates of both strains, although not necessarily equally. Furthermore, here we allow strains to have different death rates δ_1 and δ_2. We still assume that both strains have the same diffusion constant for simplicity. Now the model equations read as

$$\frac{\partial n_1}{\partial t} = \frac{\gamma_1}{1+A} n_1(1-n_1-n_2) - \delta_1 n_1 - \kappa n_1 n_2 + \nabla^2 n_1, \tag{2.40}$$

$$\frac{\partial n_2}{\partial t} = \frac{1}{1+\alpha A} n_2(1-n_1-n_2) - \delta_2 n_2 + \nabla^2 n_2, \tag{2.41}$$

$$\frac{\partial A}{\partial t} = \gamma_{A1} n_1 + \gamma_{A2} n_2 - \delta_A A + D_A \nabla^2 A. \tag{2.42}$$

Similar to the results in the Main text, for infinitely fast inhibitor diffusion, A is spatially-uniform with a magnitude that is now dependent on the mean concentrations of both types of bacteria over the entire domain. If s_1 is the surface area fraction occupied by the type-1 strain, then $n_1^* = 0, n_2^* = 1-\delta_2(1+\alpha A)$ and $n_1^* = 1-\frac{\delta_1}{\gamma_1}(1+A), n_2^* = 0$ are the two local fixed points. This yields the self-consistency condition resulting in the relation between s_1 and A:

$$s_1\gamma_{A1}(1-\frac{\delta_1}{\gamma_1}(1+A)) + (1-s_1)\gamma_{A2}(1-\delta_2(1+\alpha A)) = \delta_A A, \tag{2.43}$$

then

$$A = \frac{s_1\gamma_{A1}(1-\frac{\delta_1}{\gamma_1}) + (1-s_1)\gamma_{A2}(1-\delta_2)}{s_1\gamma_{A1}\frac{\delta_1}{\gamma_1} + (1-s_1)\gamma_{A2}\delta_2\alpha + \delta_A}. \tag{2.44}$$

Stationary fronts for infinitely fast inhibitor diffusion. First, we derive the condition for stationary fronts for the generalized two-variable model with $\delta_1 \neq \delta_2$. Since A affects the growth rate of n_2 in the subsequent analysis, we also do not scale out the growth rate of n_2 and write it

explicitly as γ_2. Consider the equations

$$\frac{\partial n_1}{\partial t} = \gamma_1 n_1(1-n_1-n_2) - \delta_1 n_1 - \kappa n_1 n_2 + \nabla^2 n_1, \quad (2.45)$$

$$\frac{\partial n_2}{\partial t} = \gamma_2 n_2(1-n_1-n_2) - \delta_2 n_2 + \nabla^2 n_2. \quad (2.46)$$

We assume that $\kappa = \varepsilon K$, $\delta_1 = \varepsilon\Delta_1$, $\delta_2 = \varepsilon\Delta_2$ with $\varepsilon \ll 1$, and again introduce new variables

$$N = \varepsilon^{-1}(n_1+n_2-1), \;\; \xi = n_1 - n_2. \quad (2.47)$$

Conversely, $n_1 = (1+\varepsilon N+\xi)/2, n_2 = (1+\varepsilon N-\xi)/2$. In new variables and in the first order in ε,

$$\partial_t N = -\frac{N}{2}(\gamma_1+\gamma_2) - \frac{N}{2}(\gamma_1-\gamma_2)\xi - \frac{1}{2}(\Delta_1+\Delta_2) - \frac{\xi}{2}(\Delta_1-\Delta_2) - \frac{K}{4}(1-\xi^2) + \nabla^2 N \quad (2.48)$$

$$\frac{\partial_t \xi}{\varepsilon} = -\frac{N}{2}(\gamma_1-\gamma_2) - \frac{N}{2}(\gamma_1+\gamma_2)\xi - \frac{\xi}{2}(\Delta_1+\Delta_2) - \frac{1}{2}(\Delta_1-\Delta_2) - \frac{K}{4}(1-\xi^2) + \frac{\nabla^2\xi}{\varepsilon} \quad (2.49)$$

The first equation describes fast relaxation toward the solution

$$N = -\frac{(\Delta_1+\Delta_2) + \xi(\Delta_1-\Delta_2) + \frac{K}{2}(1-\xi^2)}{\gamma_1+\gamma_2+\xi(\gamma_1-\gamma_2)}. \quad (2.50)$$

Assuming that the fast initial relaxation has occurred, and N is slaved to ξ, we can substitute N from Eq. (2.50) in Eq. (2.49). Returning to the original parameters κ and $\delta_{1,2}$, after simple algebra we get a single reaction-diffusion equation for the slow dynamics of ξ,

$$\partial_t \xi = f(\xi) + \nabla^2 \xi, \quad (2.51)$$

where

$$f(\xi) = \frac{1-\xi^2}{1+\Gamma\xi}\left[\frac{\delta_1+\delta_2}{2}\Gamma - \frac{\delta_1-\delta_2}{2} + (\Gamma-1)(1-\xi)\frac{\kappa}{4}\right] \quad (2.52)$$

with $\Gamma = (\gamma_1 - \gamma_2)/(\gamma_1 + \gamma_2)$. For small $\delta_{1,2}$ and κ, this equation describes slow front propagation. Function $f(\xi)$ has two roots $\xi_{1,2} = \pm 1$ corresponding to stable fixed points of Eq. (2.51), and an intermediate root at $\frac{\delta_1+\delta_2}{2}\Gamma - \frac{\delta_1-\delta_2}{2} + (\Gamma-1)(1-\xi)\frac{\kappa}{4} = 0$ corresponding to an unstable fixed point. Maxwell rule states that a front solution of the 1-D reaction-diffusion equation (2.51) connecting stable fixed points ξ_1 and ξ_2 is stationary if $\int_{\xi_1}^{\xi_2} f(\xi) d\xi = 0$.

For finite Γ, integration of the full function (2.52) yields the following expression for κ at which the front is stationary,

$$\kappa = \frac{3(\gamma-1)^2(\gamma^2 - 1 - 2\gamma\ln\gamma)}{2\gamma^3 + 3\gamma^2 - 6\gamma + 1 - 6\gamma^2\ln\gamma}\left(\frac{\delta_1+\delta_2}{2} - \frac{\delta_1-\delta_2}{2}\frac{\gamma+1}{\gamma-1}\right), \tag{2.53}$$

where $\gamma = \gamma_1/\gamma_2$.

Returning to the three-variable model (Eqs. (2.40)-(2.42)), we notice that for spatially uniform A, the rescaled growth rates are $\gamma_1^* = \frac{\gamma_1}{1+A}$ and $\gamma_2^* = \frac{1}{1+\alpha A}$, and

$$\gamma = \frac{\gamma_1^*}{\gamma_2^*} = \gamma_1\frac{1+\alpha A}{1+A}. \tag{2.54}$$

Thus, the fronts become stationary when A is equal to uniform A^* at which γ and κ satisfy Eq. (2.53). This value of A^* corresponds to a particular area fraction s_1^* according to Eq. (2.44). Thus, the union of the curves defined by Eq. (2.53) together with Eqs. (2.44) and (2.54) when s_1 changes from 0 to 1, will yield the region for stationary fronts where we can expect emergence of patterns.

Stability of stationary fronts. Next we derive the condition for stability of stationary fronts with respect to their uniform displacement. If there is a small front displacement that changes s_1 with respect to s_1^* by a perturbation Δs_1, then the ratio of γ_1/γ_2 changes as well, by $\Delta\gamma = \frac{\partial\gamma}{\partial A}\frac{\partial A}{\partial s_1}\Delta s_1$. It is easy to see that the stationary front is stable if $\Delta s_1 \Delta\gamma < 0$, so for $s_1 > s_1^*$, $\gamma < \gamma^*$, the front moves in the direction that decreases s_1 back to s_1^*. In the opposite case, the front will move in the direction

to further increase s_1, and n_1 will win. Thus, the condition for stable stationary fronts is

$$\frac{\partial\gamma}{\partial A}\frac{\partial A}{\partial s_1} = \gamma_1 \frac{\alpha-1}{(1+A)^2} \frac{\gamma_{A1}\gamma_{A2}[\alpha\delta_2(1-\frac{\delta_1}{\gamma_1}) - \frac{\delta_1}{\gamma_1}(1-\delta_2)] + [\gamma_{A1}(1-\frac{\delta_1}{\gamma_1}) - \gamma_{A2}(1-\delta_2))]\delta_A}{[s_1\gamma_{A1}\frac{\delta_1}{\gamma_1} + (1-s_1)\gamma_{A2}\delta_2\alpha + \delta_A]^2} < 0. \tag{2.55}$$

If $\delta_1, \delta_2, \gamma_{A1}, \gamma_{A2} \ll 1$, the condition can be simplified to

$$(\alpha-1)(\gamma_{A1} - \gamma_{A2}) < 0. \tag{2.56}$$

This means if n_2 produces A faster than n_1 ($\gamma_{A2} > \gamma_{A1}$), for the stationary fronts to be stable, the growth inhibition of n_2 should be stronger ($\alpha > 1$) and vice versa. If $\alpha = 1$, then $\gamma = \gamma_1$ is a constant, and the front is only stationary on a single curve, as in the two-variable model without long-range inhibition.

One example of the region for stationary fronts and pattern formation is shown in Fig. 2.10.

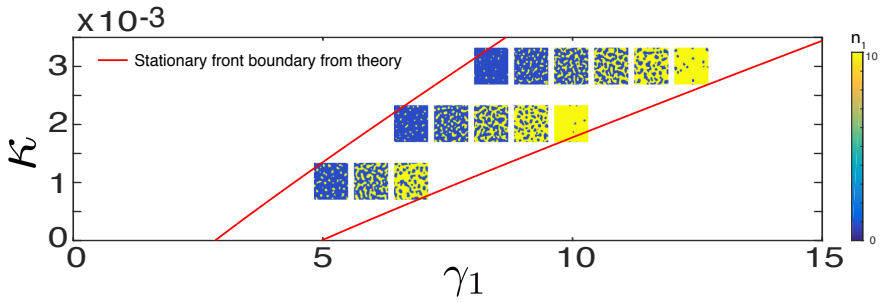

Figure 2.10: Typical patterns emerging from random initial conditions in stochastic simulations of the dual-inhibition model for different values of parameters κ and γ_1. Other parameters are $n_0 = 10, \alpha = 0.1, \delta_1 = 0.01, \delta_2 = 0.005, \gamma_{A1} = 0.004, \gamma_{A2} = 0.001, \delta_A = 0.02, D_A = 12.5, P_n = 0.1$. The system size is 256×256.

2.6.4 Front pinning

To address the issue of possible front pinning due to spatial discretization of continuous reaction-diffusion-type models and compare the results with Blanchard et al.[19], we performed 1D simulations of front dynamics in the two-variable model (Eqs. (2.10)(2.11)), but changed the diffusion constant to a much smaller value $D_n = 0.01$ using different spatial discretizations of the computational domain of fixed length $L = 1024$. The results are shown in Fig. 2.15. The width of the wedge in the (γ_1, κ) plane in which fronts are stationary decreases exponentially with the number of grid points. When the number of spatial points is 1024, the width of the wedge is so small that it appears as a single line that is consistent with the continuum theory prediction (red curve). However, when the number of spatial points is reduced to 512, the wedge where fronts are stationary appears, which means front pinning. When the number of points is reduced even further, the region for front pinning becomes larger. The fewer number of grid points is equivalent to smaller diffusion constants for the same spatial resolution, thus these results also imply that, as the diffusion constant becomes smaller, the parameter region for pinned fronts increases, which is consistent with Ref. [19]. In our simulations, we used relatively high diffusion constant $D_n = 1$ and a sufficiently large number of grid points to make pinning effects negligible.

2.6.5 Details of the discrete lattice model

In our stochastic simulations, we used a discrete lattice model to simulate strain competition and pattern formation. Specifically, the rules of the model are as follows: the number of cells in each strain is an integer number, so we used unscaled parameters to carry out the simulations. We use a lattice model to do stochastic simulations, the rules for the simulations are:

1. We consider a square lattice model $0 \leq \{i, j\} \leq N$.

2. The number of individuals of each of the two species n_1, n_2 at each lattice site $\{i, j\}$ is integer,

and the sum of $n_1(i,j)$ and$n_2(i,j)$ cannot exceed the maximum carrying capacity n_0.

3. The inhibitor A is defined as a real-valued field on the same lattice.

4. At each time step Δt, $n_1(i,j)$ can increase by one, $[n_1(i,j) \to n_1(i,j)+1]$, with the probability $\gamma_1 n_1(i,j)[1-(n_1(i,j)+n_2(i,j))/n_0]\Delta t$ or die $[n_1(i,j) \to n_1(i,j)-1]$ with the probability $(\delta n_1(i,j)+\kappa n_1(i,j)n_2(i,j))\Delta t$. Similar probabilities apply to n_2 with swapping of subscripts $1 \leftrightarrow 2$ without the killing term.

5. Each cell can jump to one of four neighboring squares with the probability $P_n\Delta t$. The destination site is chosen at random, unless the neighboring site already has n_0 cells, then jumping there is forbidden.

6. We impose periodic boundary conditions in both dimensions for $n_1(i,j), n_2(i,j)$, and $A(i,j)$.

7. Reaction-diffusion dynamics of A is implemented via a split-step pseudo-spectral method.

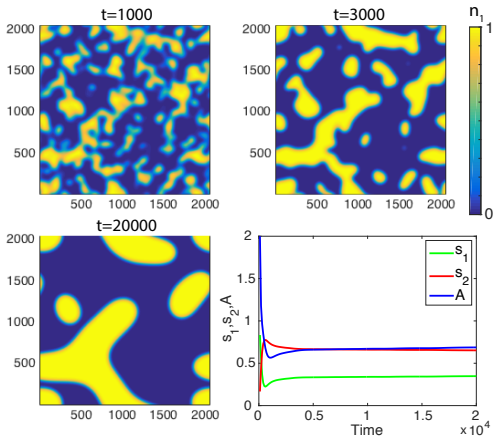

Figure 2.11: Phase separation in the deterministic model with spatially uniform inhibitor A (infinite D_A) and random initial conditions. Three snapshots of n_1 and the time course of s_1, s_2 and A for 2D model. At large times, the area fractions s_1 and s_2 approach constant values, and the patterned state stabilizes. Parameters: $\gamma_1 = 4.5$, $\delta = 0.01$, $\kappa = 0.03$, $\gamma_A = 0.04$, $\delta_A = 0.02$.

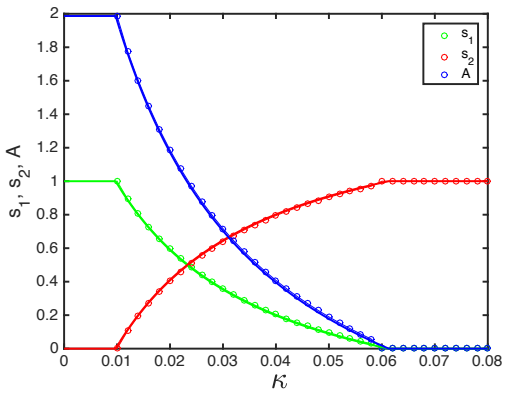

Figure 2.12: Final area fractions of the two strains and the inhibitor level A as functions of the killing rate κ in the deterministic 1D model with spatially uniform inhibitor A (infinite D_A) and random initial conditions. The solid curves show the theoretical predictions using Eqs. (2.4)(2.6) in the Main text, and the circles show the simulation results. Parameters: $\gamma_1 = 4.5, \delta = 0.01, \gamma_A = 0.04, \delta_A = 0.02$, system size is 4096.

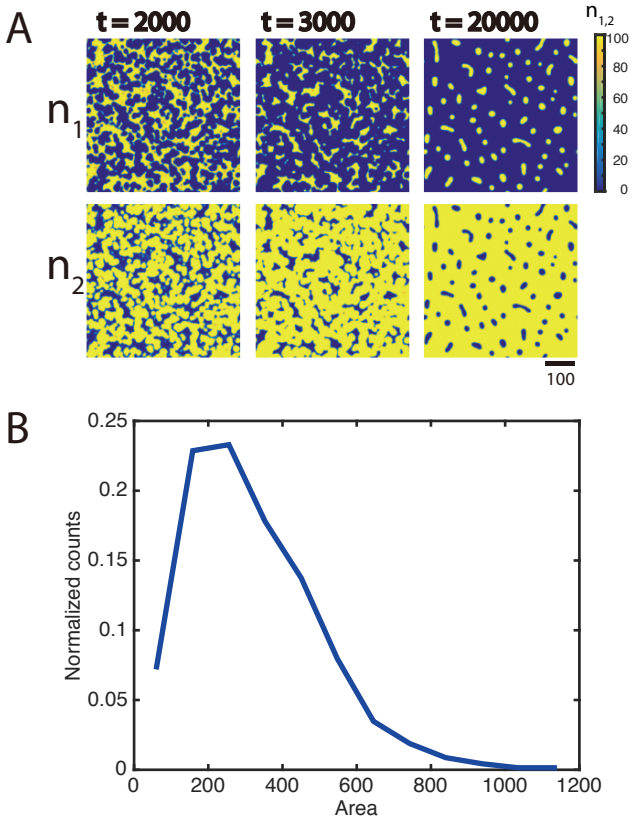

Figure 2.13: Discrete stochastic simulations of pattern formation in a mixture of T6SS-sensitive (n_1) and T6SS-active (n_2) bacteria. (A) Three snapshots of a typical simulation. (B) Area distribution of spots of n_1 at $t = 20000$. The distribution result is from 10 stochastic simulations. Parameters: $\gamma_1 = 3, \gamma_2 = 1, n_0 = 100, \delta = 0.01, \gamma_A = 0.0001, \delta_A = 0.005, P_n = 0.04, D_A = 5$ and $\kappa = 0.00025$.

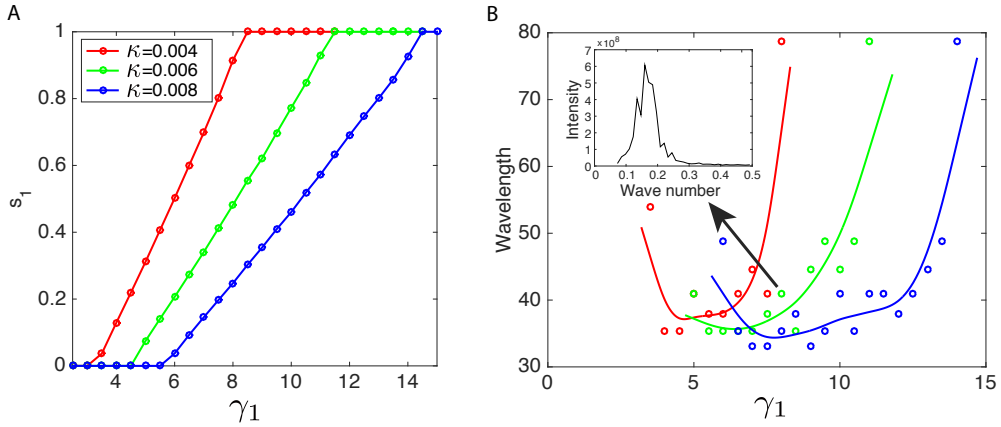

Figure 2.14: Analysis of the patterns in stochastic simulations in Fig. 2.6. (A) n_1 area ratio s_1 vs. γ_1 in stochastic simulations for different κ. The fraction of n_1 changes continuously from 0 to 1 as the control parameter γ_1 moves across the pattern-forming range. (B) Peak wavelength of the asymptotic pattern vs. γ_1 for the same three values of κ as in panel (A). The circles are from simulations. The curves are smoothing spline extrapolated of the circles with the same color. The characteristic scale is diverging near the boundaries of the pattern-forming region in the parameter space. Inset: the power spectrum for $\kappa = 0.006, \gamma_1 = 8$. It has a well-defined peak corresponding to the characteristic distance between the spots or the period of the labyrinthine pattern.

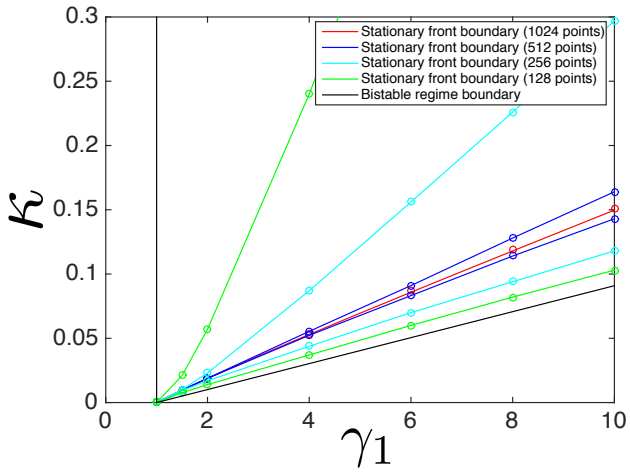

Figure 2.15: Coarse spatial discretization leads to front pinning in finite-difference numerical simulations. Different lines show the simulation results for different numbers of grid points. Parameters: $\delta = 0.01, D_n = 0.01$.

References

[1] Reed M Stubbendieck, Carol Vargas-Bautista, and Paul D Straight. Bacterial communities: interactions to scale. *Frontiers in microbiology*, 7:1234, 2016.

[2] Ashleigh S Griffin, Stuart A West, and Angus Buckling. Cooperation and competition in pathogenic bacteria. *Nature*, 430(7003):1024–1027, 2004.

[3] Joao B Xavier, Wook Kim, and Kevin R Foster. A molecular mechanism that stabilizes cooperative secretions in pseudomonas aeruginosa. *Molecular Microbiology*, 79(1):166–179, 2011.

[4] Michael E Hibbing, Clay Fuqua, Matthew R Parsek, and S Brook Peterson. Bacterial competition: surviving and thriving in the microbial jungle. *Nature Reviews Microbiology*, 8(1):15–25, 2010.

[5] Olaya Rendueles and Jean-Marc Ghigo. Mechanisms of competition in biofilm communities. *Microbiology Spectrum*, 3(3):MB–0009–2014, 2015.

[6] H Stolp and MP Starr. Bdellovibrio bacteriovorus gen. et sp. n., a predatory, ectoparasitic, and bacteriolytic microorganism. *Antonie Van Leeuwenhoek*, 29(1):217–248, 1963.

[7] Susan C Straley and SF Conti. Chemotaxis by bdellovibrio bacteriovorus toward prey. *Journal of Bacteriology*, 132(2):628–640, 1977.

[8] Klaus Jürgens and Carsten Matz. Predation as a shaping force for the phenotypic and genotypic composition of planktonic bacteria. *Antonie van Leeuwenhoek*, 81(1-4):413–434, 2002.

[9] Katharine Z Coyte, Jonas Schluter, and Kevin R Foster. The ecology of the microbiome: networks, competition, and stability. *Science*, 350(6261):663–666, 2015.

[10] Stefan Pukatzki, Amy T Ma, Derek Sturtevant, Bryan Krastins, David Sarracino, William C Nelson, John F Heidelberg, and John J Mekalanos. Identification of a conserved bacterial protein secretion system in Vibrio cholerae using the Dictyostelium host model system. *Proceedings of the National Academy of Sciences, USA*, 103(5):1528–1533, 2006.

[11] Petr G Leiman, Marek Basler, Udupi A Ramagopal, Jeffrey B Bonanno, J Michael Sauder, Stefan Pukatzki, Stephen K Burley, Steven C Almo, and John J Mekalanos. Type VI secretion apparatus and phage tail-associated protein complexes share a common evolutionary origin. *Proceedings of the National Academy of Sciences, USA*, 106(11):4154–4159, 2009.

[12] M Basler, M Pilhofer, GP Henderson, GJ Jensen, and JJ Mekalanos. Type VI secretion requires a dynamic contractile phage tail-like structure. *Nature*, 483(7388):182–186, 2012.

[13] Lisa G Pell, Voula Kanelis, Logan W Donaldson, P Lynne Howell, and Alan R Davidson. The phage λ major tail protein structure reveals a common evolution for long-tailed phages and the type VI bacterial secretion system. *Proceedings of the National Academy of Sciences, USA*, 106(11):4160–4165, 2009.

[14] Véronique de Berardinis, David Vallenet, Vanina Castelli, Marielle Besnard, Agnes Pinet, Corinne Cruaud, Sumitta Samair, Christophe Lechaplais, Gabor Gyapay, Céline Richez, et al. A complete collection of single-gene deletion mutants of acinetobacter baylyi adp1. *Molecular Systems Biology*, 4(1):174, 2008.

[15] Michael D Carruthers, Paul A Nicholson, Erin N Tracy, and Robert S Munson Jr. Acinetobacter baumannii utilizes a type VI secretion system for bacterial competition. *PloS one*, 8(3):e59388, 2013.

[16] M Basler and JJ Mekalanos. Type 6 secretion dynamics within and between bacterial cells. *Science*, 337(6096):815–815, 2012.

[17] David Bruce Borenstein, Peter Ringel, Marek Basler, and Ned S Wingreen. Established microbial colonies can survive type VI secretion assault. *PLoS Comput Biol*, 11(10):e1004520, 2015.

[18] Luke McNally, Eryn Bernardy, Jacob Thomas, Arben Kalziqi, Jennifer Pentz, Sam P Brown, Brian K Hammer, Peter J Yunker, and William C Ratcliff. Killing by Type VI secretion drives genetic phase separation and correlates with increased cooperation. *Nature Communications*, 8:14371, 2017.

[19] Andrew E Blanchard, Venhar Celik, and Ting Lu. Extinction, coexistence, and localized patterns of a bacterial population with contact-dependent inhibition. *BMC Systems Biology*, 8(1):1, 2014.

[20] Ana Carpio and Luis L Bonilla. Depinning transitions in discrete reaction-diffusion equations. *SIAM Journal on Applied Mathematics*, 63(3):1056–1082, 2003.

[21] Mitsugu Matsushita and Hiroshi Fujikawa. Diffusion-limited growth in bacterial colony formation. *Physica A: Statistical Mechanics and its Applications*, 168(1):498–506, 1990.

[22] Beth A Lazazzera. Quorum sensing and starvation: signals for entry into stationary phase. *Current Opinion in Microbiology*, 3(2):177–182, 2000.

[23] K Nakano, M Rischke, S Sato, and H Märkl. Influence of acetic acid on the growth of escherichia coli k12 during high-cell-density cultivation in a dialysis reactor. *Applied Microbiology and Biotechnology*, 48(5):597–601, 1997.

[24] Ahmad S Khalil and James J Collins. Synthetic biology: applications come of age. *Nature Reviews Genetics*, 11(5):367–379, 2010.

[25] James Clerk Maxwell. On the dynamical evidence of the molecular constitution of bodies. *Nature*, 11(279):357–359, 1875.

[26] Alan Mathison Turing. The chemical basis of morphogenesis. *Philosophical Transactions of the Royal Society of London B: Biological Sciences*, 237(641):37–72, 1952.

[27] Fredrik Bäckhed, Ruth E Ley, Justin L Sonnenburg, Daniel A Peterson, and Jeffrey I Gordon. Host-bacterial mutualism in the human intestine. *science*, 307(5717):1915–1920, 2005.

[28] Sarkis K Mazmanian, June L Round, and Dennis L Kasper. A microbial symbiosis factor prevents intestinal inflammatory disease. *Nature*, 453(7195):620–625, 2008.

[29] Yun Kyung Lee and Sarkis K Mazmanian. Has the microbiota played a critical role in the evolution of the adaptive immune system? *Science*, 330(6012):1768–1773, 2010.

[30] Les Dethlefsen and David A Relman. Incomplete recovery and individualized responses of the human distal gut microbiota to repeated antibiotic perturbation. *Proceedings of the National Academy of Sciences*, 108(Supplement 1):4554–4561, 2011.

[31] Rick Durrett and Simon Levin. Allelopathy in spatially distributed populations. *Journal of theoretical biology*, 185(2):165–171, 1997.

[32] Benjamin Kerr, Margaret A Riley, Marcus W Feldman, and Brendan JM Bohannan. Local dispersal promotes biodiversity in a real-life game of rock–paper–scissors. *Nature*, 418(6894):171–174, 2002.

[33] Tamás L Czárán, Rolf F Hoekstra, and Ludo Pagie. Chemical warfare between microbes promotes biodiversity. *Proceedings of the National Academy of Sciences*, 99(2):786–790, 2002.

[34] Tobias Reichenbach, Mauro Mobilia, and Erwin Frey. Mobility promotes and jeopardizes biodiversity in rock–paper–scissors games. *Nature*, 448(7157):1046–1049, 2007.

[35] Karen De Roy, Massimo Marzorati, Pieter Van den Abbeele, Tom Van de Wiele, and Nico Boon. Synthetic microbial ecosystems: an exciting tool to understand and apply microbial communities. *Environmental microbiology*, 16(6):1472–1481, 2014.

[36] Spencer R Scott, M Omar Din, Philip Bittihn, Liyang Xiong, Lev S Tsimring, and Jeff Hasty. A stabilized microbial ecosystem of self-limiting bacteria using synthetic quorum-regulated lysis. *Nature Microbiology*, 2:nmicrobiol201783, 2017.

[37] Steven A Frank. Spatial polymorphism of bacteriocins and other allelopathic traits. *Evolutionary Ecology*, 8(4):369–386, 1994.

[38] Lin Chao and Bruce R Levin. Structured habitats and the evolution of anticompetitor toxins in bacteria. *Proceedings of the National Academy of Sciences*, 78(10):6324–6328, 1981.

[39] Yoh Iwasa, Mayuko Nakamaru, et al. Allelopathy of bacteria in a lattice population: competition between colicin-sensitive and colicin-producing strains. *Evolutionary Ecology*, 12(7):785–802, 1998.

[40] Yves Pomeau. Front motion, metastability and subcritical bifurcations in hydrodynamics. *Physica D: Nonlinear Phenomena*, 23(1):3–11, 1986.

[41] James P Keener. Propagation and its failure in coupled systems of discrete excitable cells. *SIAM Journal on Applied Mathematics*, 47(3):556–572, 1987.

[42] Gábor Fáth. Propagation failure of traveling waves in a discrete bistable medium. *Physica D: Nonlinear Phenomena*, 116(1):176–190, 1998.

[43] Joel Keizer, Gregory D Smith, Silvina Ponce-Dawson, and John E Pearson. Saltatory propagation of ca 2+ waves by ca 2+ sparks. *Biophysical journal*, 75(2):595–600, 1998.

[44] Igor S Aranson, Boris A Malomed, Len M Pismen, and Lev S Tsimring. Crystallization kinetics and self-induced pinning in cellular patterns. *Physical Review E*, 62(1):R5, 2000.

[45] Konstantin Kladko, Igor Mitkov, and AR Bishop. Universal scaling of wave propagation failure in arrays of coupled nonlinear cells. *Physical review letters*, 84(19):4505, 2000.

[46] Igor Mitkov, Konstantin Kladko, and John E Pearson. Tunable pinning of burst waves in extended systems with discrete sources. *Physical review letters*, 81(24):5453, 1998.

[47] Max Rietkerk, Stefan C Dekker, Peter C de Ruiter, and Johan van de Koppel. Self-organized patchiness and catastrophic shifts in ecosystems. *Science*, 305(5692):1926–1929, 2004.

[48] Joao B Xavier, Esteban Martinez-Garcia, and Kevin R Foster. Social evolution of spatial patterns in bacterial biofilms: when conflict drives disorder. *The American Naturalist*, 174(1):1–12, 2009.

[49] Mariana Bitrian, Rodrigo H González, Gaston Paris, Klaas J Hellingwerf, and Clara B Nudel. Blue-light-dependent inhibition of twitching motility in acinetobacter baylyi adp1: additive involvement of three bluf-domain-containing proteins. *Microbiology*, 159(9):1828–1841, 2013.

[50] Dmitri Volfson, Scott Cookson, Jeff Hasty, and Lev S Tsimring. Biomechanical ordering of dense cell populations. *Proceedings of the National Academy of Sciences*, 105(40):15346–15351, 2008.

[51] Denis Boyer, William Mather, Octavio Mondragón-Palomino, Sirio Orozco-Fuentes, Tal Danino, Jeff Hasty, and Lev S Tsimring. Buckling instability in ordered bacterial colonies. *Physical biology*, 8(2):026008, 2011.

[52] Timothy J Rudge, Paul J Steiner, Andrew Phillips, and Jim Haseloff. Computational modeling of synthetic microbial biofilms. *ACS Synthetic Biology*, 1(8):345–352, 2012.

[53] Carey D Nadell, Knut Drescher, and Kevin R Foster. Spatial structure, cooperation and competition in biofilms. *Nature Reviews Microbiology*, 14(9):589–600, 2016.

[54] Ido Golding, Yonathan Kozlovsky, Inon Cohen, and Eshel Ben-Jacob. Studies of bacterial branching growth using reaction–diffusion models for colonial development. *Physica A: Statistical Mechanics and its Applications*, 260(3):510–554, 1998.

[55] Masayasu Mimura, Hideo Sakaguchi, and Mitsugu Matsushita. Reaction–diffusion modelling of bacterial colony patterns. *Physica A: Statistical Mechanics and its Applications*, 282(1):283–303, 2000.

[56] Howard C Berg. *E. coli in Motion*. Springer Science & Business Media, 2008.

[57] Chenli Liu, Xiongfei Fu, Lizhong Liu, Xiaojing Ren, Carlos KL Chau, Sihong Li, Lu Xiang, Hualing Zeng, Guanhua Chen, Lei-Han Tang, et al. Sequential establishment of stripe patterns in an expanding cell population. *Science*, 334(6053):238–241, 2011.

[58] Maxime Durot, François Le Fèvre, Véronique de Berardinis, Annett Kreimeyer, David Vallenet, Cyril Combe, Serge Smidtas, Marcel Salanoubat, Jean Weissenbach, and Vincent Schachter. Iterative reconstruction of a global metabolic model of acinetobacter baylyi adp1 using high-throughput growth phenotype and gene essentiality data. *BMC Systems Biology*, 2(1):85, 2008.

[59] Matthew Scott, Carl W Gunderson, Eduard M Mateescu, Zhongge Zhang, and Terence Hwa. Interdependence of cell growth and gene expression: origins and consequences. *Science*, 330(6007):1099–1102, 2010.

[60] Rutger Hermsen, Hiroyuki Okano, Conghui You, Nicole Werner, and Terence Hwa. A growth-rate composition formula for the growth of e. coli on co-utilized carbon substrates. *Molecular systems biology*, 11(4):801, 2015.

[61] Michaeline B Nelson, Alexander B Chase, Jennifer BH Martiny, Roman Stocker, Jen Nguyen, Karen Lloyd, Reid T Oshiro, Daniel B Kearns, Johannes P Schneider, Peter D Ringel, et al. The microbial olympics 2016. *Nature microbiology*, 1:16122, 2016.

[62] Peter David Ringel, Di Hu, and Marek Basler. The role of type vi secretion system effectors in target cell lysis and subsequent horizontal gene transfer. *Cell reports*, 21(13):3927–3940, 2017.

[63] Ping Wang, Lydia Robert, James Pelletier, Wei Lien Dang, Francois Taddei, Andrew Wright, and Suckjoon Jun. Robust growth of escherichia coli. *Current biology*, 20(12):1099–1103, 2010.

[64] Tal Danino, Octavio Mondragón-Palomino, Lev Tsimring, and Jeff Hasty. A synchronized quorum of genetic clocks. *Nature*, 463(7279):326–330, 2010.

[65] Arthur Prindle, Phillip Samayoa, Ivan Razinkov, Tal Danino, Lev S Tsimring, and Jeff Hasty. A sensing array of radically coupled genetic biopixels. *Nature*, 481(7379):39–44, 2012.

[66] Osnat Gillor, Benjamin C Kirkup, and Margaret A Riley. Colicins and microcins: the next generation antimicrobials. *Advances in Applied Microbiology*, 54:129–146, 2004.

[67] Margaret A Riley and John E Wertz. Bacteriocins: evolution, ecology, and application. *Annual Reviews in Microbiology*, 56(1):117–137, 2002.

[68] David Gordon, Elizabeth Oliver, and Jane Littlefield-Wyer. The diversity of bacteriocins in gram-negative bacteria. *Bacteriocins*, pages 5–18, 2007.

Chapter 3

Flower-like patterns in multi-species bacterial colonies

3.1 Introduction

In addition to biochemical interactions, mechanical forces also play an important role in shaping the structure of bacterial communities. In dense colonies, bacteria push against each other due to growth and motility. Bacteria can exploit these mechanical interactions to adapt to the environment. For example, mechanical stresses cause buckling in *Bacillus subtilis* biofilms that allows them to improve nutrient transport and consumption [1, 2, 3]. Although the role of mechanical interactions in single-species colonies has been studied previously [4, 5, 6, 7, 8], dynamics of multi-species communities driven by mechanical forces have received much less attention. Since bacterial strains can have significant differences in their growth and motility characteristics, one can expect the development of highly-heterogeneous mechanical stress distribution , which in turn can result in a complex spatiotemporal dynamics of the colony.

To study the interactions between bacterial species with distinct biological and physical

properties, we choose *Acinetobacter baylyi*, a gram-negative bacterium that easily moves on soft surfaces using twitching motility [9, 10, 11], and an *Escherichia coli* strain that is almost non-motile on soft agar. Additionally, wild-type *A. baylyi* possesses a Type VI Secretion System (T6SS) that enables them to kill other bacteria (including *E. coli*) on direct contact [12, 13]. We found that when these two strains are mixed together and inoculated on an agar surface, growing colonies develop intricate flower-like structures that are absent when either species is grown by itself.

To shed light on the mechanism behind this intricate pattern formation, we tested whether biological cell-cell communication or mechanical interaction between strains with different motilities played the key role. Experiments with *A. baylyi* mutants lacking T6SS showed that the pattern formation did not rely on this system. On the other hand, genetically impairing *A. baylyi* motility eliminated the patterns entirely. We also demonstrated that agar concentration that affects cell motility, also played an important role in pattern formation. These findings suggested that the mechanical interactions between species were indeed primarily responsible for the pattern formation.

We then formulated and analyzed two models: a geometrical model of the colony boundary motion and a 2D phase-field model of the entire colony, to describe the mechanical interactions between two species. Our results show that growth and cell motility differences are sufficient to explain the emerging patterns. Since the mechanism of flower-like pattern formation is rather general, it may be broadly generalizable to other multi-species colonies.

3.2 Results

3.2.1 Flower-like patterns in mixtures of *A. baylyi* and *E. coli* on nutrient-rich soft agar

We inoculated a mixture of *E. coli* and *A. baylyi* cells with an initial density ratio of 10:1 at the center of a Petri dish filled with soft LB agar (0.5% agar). To distinguish the two strains, we

labeled *E. coli* with constitutively expressed mTFP. After growing at 37°C for 3 days, this colony developed an intricate flower-like pattern (Fig. 3.1a). To see how such patterns form, we tracked the colony growth with time-lapse imaging (Fig. 3.1b). Up to 8 hours after inoculation, the expanding colony remained nearly uniform and circular. Then the colony front began visibly undulate. As the colony expanded further, the undulations grew and formed cusps that in turn would leave behind tracks (or "branches"). These branches then merged, following the movement of cusps along the interface as the colony continued to expand. The branches were visible even in bright-field imaging, but they were also bright in the teal fluorescence channel, indicating that branches predominantly consisted of *E. coli* cells (Fig. 3.6).

To test whether these flower-like patterns originate from interactions between the two species, we grew each species separately on the same 0.5% LB agar surface. The *E. coli* motility on agar is small, and the colony size remained relatively unchanged after 16 hours of growth (Fig. 3.1c, left). After the same time, a colony of highly motile *A. baylyi* reached the edge of the plate (Fig. 3.1c, right). In both cases, no patterns emerged, which proved that the flower-like pattern formation was a result of inter-species interaction. We measured the sizes of mixed, pure *E. coli* and pure *A. baylyi* colonies at different times after inoculation (Fig. 3.1d). The expansion speed of mixed colonies falls between those of pure *A. baylyi* and pure *E. coli* colonies, and the speed did not change much once the colonies began expanding.

3.2.2 *E. coli* destabilize colony front by hindering *A. baylyi* expansion

To observe the pattern formation at higher resolution, we modified the experimental setup to fit under a fluorescence microscope (see Methods). After 24 hours of growth, a droplet of 1:1 mixture of *E. coli* (expressing mTFP) and *A. baylyi* (expressing mCherry) grew into a clearly-visible flower-like pattern (Fig. 3.2a). By zooming in on the front of the expanding colony, we were able to track the formation and merging of branches that gave rise to the flower-like structure of the patterns

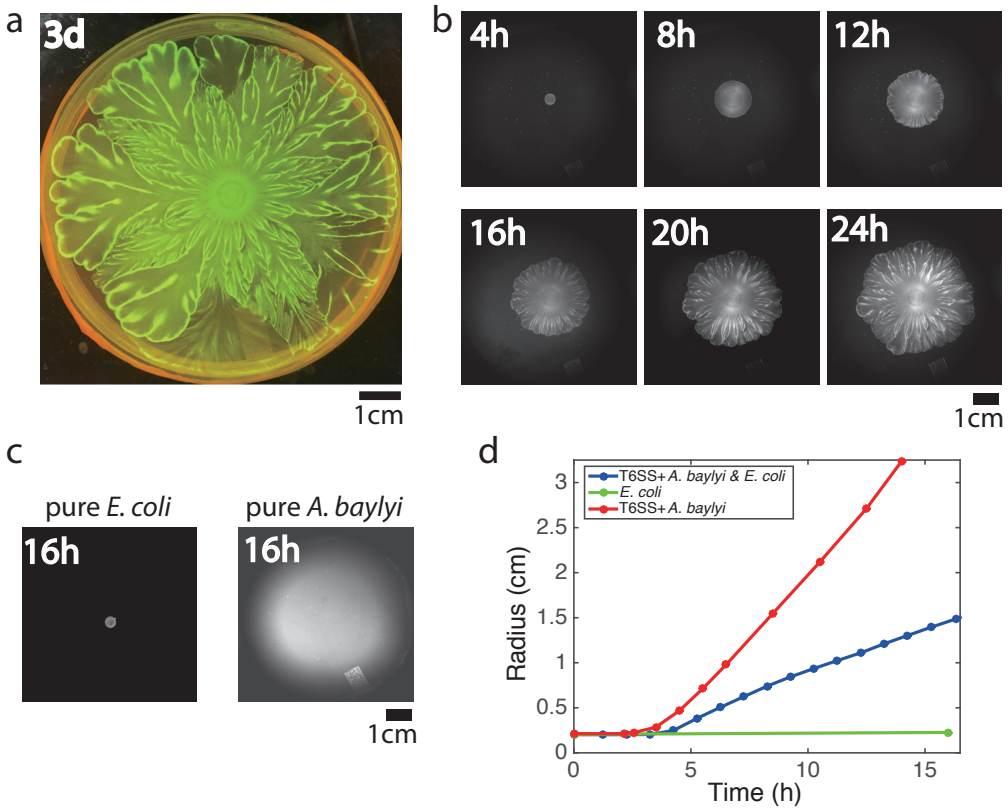

Figure 3.1: Flower-like patterns in mixtures of *E. coli* and *A. baylyi*. **a**, The pattern after 3 days of growth on a 0.5% LB agar surface. **b**, Time-lapse bright-field images of the developing pattern. **c**, Pure *E. coli* and pure *A. baylyi* colonies show no patterns. **d**, Radius of the colony vs time for pure *E. coli* (green), pure *A. baylyi* (red), and the mixture of *E. coli* and *A. baylyi* (blue). The radius is defined as $\sqrt{Area/\pi}$ where *Area* is the area of the colony which is calculated after image segmentation.

(Fig. 3.2b). While *A. baylyi* killed most of *E. coli* via T6SS within the inoculum, a significant number of *E. coli* managed to survive at the periphery where they were not in direct contact with *A. baylyi*. *E. coli* also has a higher growth rate (1.53 ± 0.11 h^{-1}, $n = 3$) than *A. baylyi* (1.13 ± 0.03 h^{-1}, $n = 3$), so by the time the colony began to expand, *E. coli* cells had already grown near the colony boundary which resulted in a band of *E. coli* around the expanding colony of mostly *A. baylyi* (Fig. 3.2b, 11h).

As the colony kept expanding, in regions with more *E. coli* cells near the front, the expansion was slower, so the interface began to curve inward (Fig. 3.2b, 13h). As the undulations grew bigger,

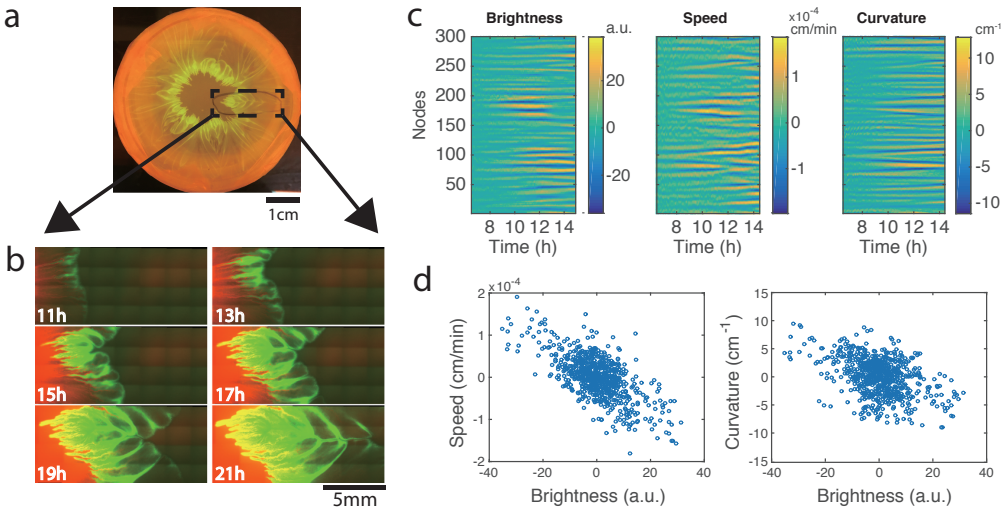

Figure 3.2: Development of branches in a growing pattern. **a**, The whole colony in a Petri dish after one day. **b**, Time-lapse microscopic images of the front propagation leading to branch formation and merging. **c**, Kymographs of detrended brightness, speed and curvature along the colony boundary. **d**, Scatter plots for detrended brightness vs speed (left) and detrended brightness vs curvature (right). Each circle corresponds to one virtual tracking node at one time point.

the *E. coli* in the regions lagging behind became more concentrated, thus slowing down the local front advance even more. Eventually, the front folded onto itself near these stagnant regions and formed narrow "branches" that continued to grow outward with the expanding colony front (Fig. 3.2b, 15h, 17h). Later, the front with the branches folded again, and the previous branches merged inside the new fold (Fig. 3.2b, 19h, 21h). Since *E. coli* continued to grow at the expanding colony front, new undulations and branches constantly appeared, and eventually a macroscopic, flower-like pattern of growing and converging branches formed.

To quantify the effect of local *E. coli* concentration on the colony expansion, we analyzed the time-lapse images in Fig. 3.1b (see Methods). We adapted a boundary tracking program for eukaryotic cells [14] to track the boundary of the bacterial colony. The colony boundary was parameterized by 300 virtual "nodes" connected by springs [15]. For each node, we measured local brightness (a proxy for *E. coli* concentration), speed and curvature. To offset the non-uniformity of

the illumination and the overall change in speed and curvature for a growing colony, we detrended the data. The kymographs of these quantities for each node are shown in Fig. 3.2c. Then we computed cross-correlations between these quantities within the time window when the pattern began to form (about 9.5 - 11.5 hours after inoculation). As shown in Fig. 3.2d (left), the brightness and extension speed show strong anti-correlation (Pearson coefficient $\rho = -0.67$). This result confirms that higher *E. coli* density slows down the front propagation. Variations in the front speed lead to variations of the local curvature, and the scatter plot between brightness and curvature indeed shows significant anti-correlation (Fig. 3.2d right, Pearson coefficient $\rho = -0.43$).

3.2.3 Robustness of flower-like patterns to perturbations

First, we explored the effect of the initial *A. baylyi*:*E. coli* (A:E) density ratio on the resulting pattern. We varied the ratio of *A. baylyi* to *E. coli* in the inoculum while maintaining the same total density of bacteria. We found that when the starting ratios are low (A:E = 1:100 and 1:10), flower-like patterns emerged, while at high ratios (10:1 and 100:1) the *E. coli* were completely eliminated and no patterns formed (Fig. 3.3a). At the intermediate ratio 1:1, *A. baylyi* dominated significantly at the center of the colony by killing *E. coli*, but the flower-like structure still developed at the colony periphery.

Second, we wondered whether T6SS-dependent killing played a role in the formation of these patterns when *E. coli* were not completely eliminated. We tested this by knocking out T6SS in *A. baylyi* (see Methods for details). The growth rate of T6SS$^-$ *A. baylyi* (1.09 ± 0.01 h^{-1}, $n = 3$) was not significantly different from the wild type while their motility was slightly lower as determined by colony expansion rate. Still, it was much higher than *E. coli* (Fig. 3.7 and 3.8). We inoculated mixtures of T6SS$^-$ *A. baylyi* and *E. coli* with different initial ratios on 0.75% LB agar, and observed that the colony formed an outer ring of *E. coli* (Fig. 3.4) and subsequently developed front instability, branches of *E. coli*, and a flower-like pattern in all cases (Fig. 3.3b). The only

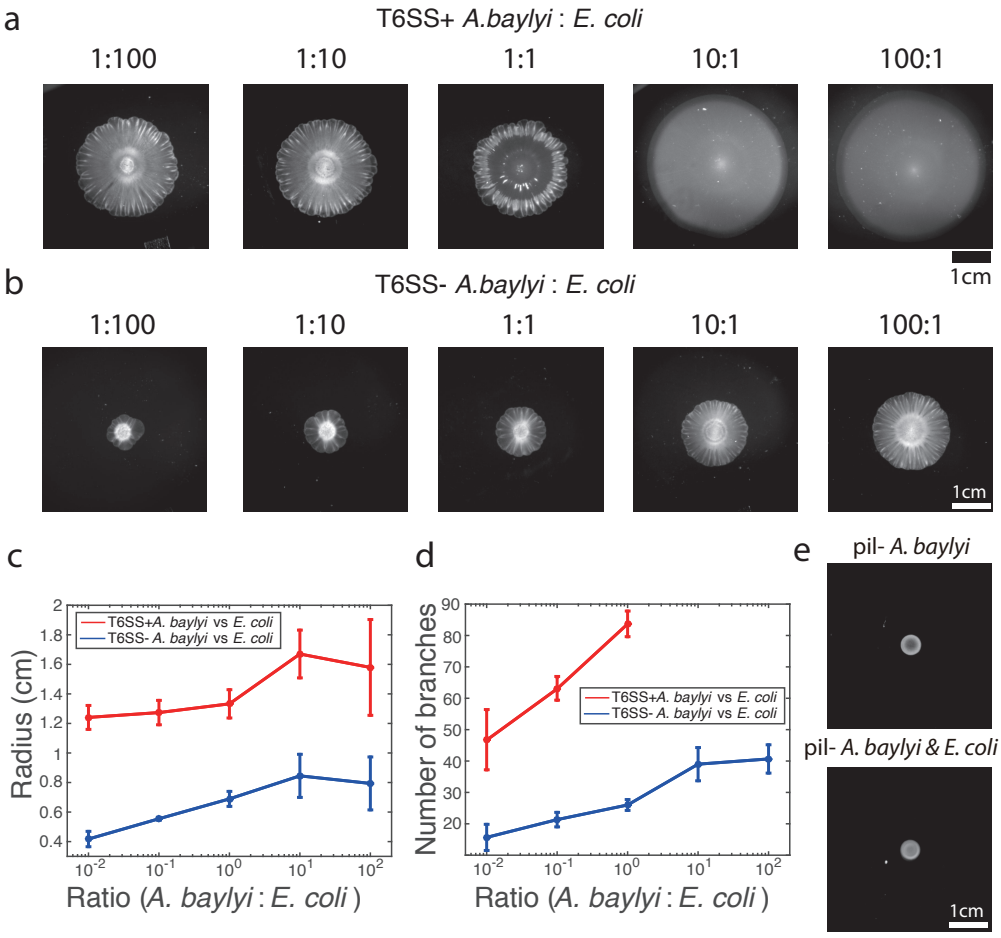

Figure 3.3: Pattern formation requires *A. baylyi* motility, but not killing. **a-b**, Bright-field snapshots of colonies of T6SS$^+$ **a**, and T6SS$^-$ **b**, *A. baylyi* with *E. coli* 16 hours after inoculations at different initial density ratios. **c**, The average colony radius vs density ratios. **d**, Number of branches at the onset of front instability vs density ratios. **e**, Colonies of pure pil$^-$ T6SS$^+$ *A. baylyi* and the mixture of pil$^-$ T6SS$^+$ *A. baylyi* and *E. coli* 16 hours after inoculation.

qualitative difference between the T6SS$^-$ and T6SS$^+$ cases was that in the non-killing case *E. coli* remained at a high concentration within the area of the initial inoculum. We measured the average radius of the colonies with different initial density ratios (Fig. 3.3c). In the case of mixture of T6SS$^-$ *A. baylyi* and *E. coli*, the more *E. coli* in the inoculum, the slower the colony expanded, which is consistent with our hypothesis that *E. coli* hinders the overall colony expansion. However, the trend is not as significant for T6SS$^+$ case because, as we reason, T6SS$^+$*A. baylyi* kill most *E.*

coli at the early stage, which increases and stabilizes the effective A:E ratio. We also counted the number of branches as they first emerged, and found more branches in colonies seeded with less *E. coli* (Fig. 3.3d). In general, the overall structure of the patterns remained unchanged in the mixture of T6SS$^-$ *A. baylyi* and *E. coli*. Thus, we concluded that the T6SS did not play a major role in the formation of flower-like patterns.

Third, the fact that two-species colonies expanded much more quickly than pure *E. coli* colonies strongly suggested that the high motility of *A. baylyi* is primarily responsible for the colony expansion. To test this hypothesis, we knocked out the *pilTU* locus of T6SS$^+$ *A. baylyi*, which is required for the pilus-based twitching motility of *A. baylyi* [16, 11]. As expected, colonies of *pilTU*$^-$ *A. baylyi* cells did not expand significantly (Fig. 3.3e, top) and did not form branching patterns when mixed with *E. coli* cells on 0.75% LB agar (Fig. 3.3e, bottom). The results are the same when the colonies grew on other concentrations of LB agar (Fig. 3.10). This demonstrates that the high *A. baylyi* motility plays a crucial role in the flower-like pattern formation.

3.2.4 Pattern-forming instability originates at the colony interface

Experiments showed that the formation of flower-like patterns appears to be preceded and caused by growing undulations of the colony front, where *E. coli* cells concentrate and locally slow expansion. To mechanistically understand how a ring of low-motility bacteria surrounding an expanding core of highly-motile bacteria can create such patterns, we turned to mathematical modeling. We adapted a one-dimensional "geometrical" model of front dynamics [17, 18] that casts the motion of the interface $\mathbf{x}(\sigma,t)$ in natural, reference-frame independent variables of curvature κ and metric g as a function of its arclength s and time t (see Appendix of this chapter):

$$\dot{\kappa} = -\left(\frac{\partial^2}{\partial s^2} + \kappa^2\right)\mathcal{F}[\kappa, g], \quad \dot{g} = 2g\kappa\mathcal{F}[\kappa, g].$$

In the overdamped limit, the velocity functional $\mathcal{F}$ is determined by the balance of a constant outward pressure force F_0 due to *A. baylyi* motility, surface tension F_s proportional to the interface curvature, and the resistance (friction) force F_r that is assumed to be proportional to the local concentration of *E. coli* on the interface $c(s,t)$ (Fig. 3.4a). For simplicity we ignore *E. coli* growth and leakage from the boundary in the interior and assume that the local concentration of *E. coli* is only changed by stretching or contraction of the interface, therefore c is taken to be inversely proportional to the metric $\sqrt{g}$. A straightforward linear stability analysis demonstrates that the interface is indeed unstable to a broad spectrum of initial perturbations (for more details see Appendix).

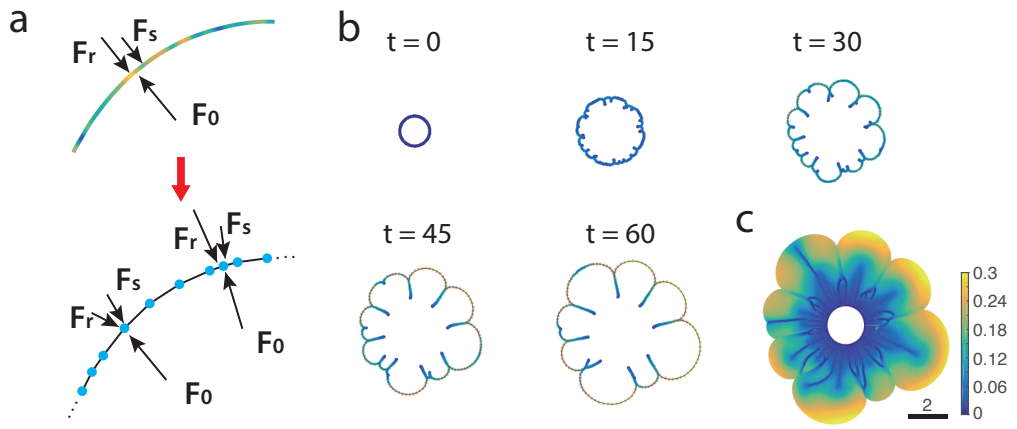

Figure 3.4: Discrete interface model. **a**, Sketches of the continuum and discrete interface models. **b**, Snapshots of the interface in discrete interface model for a sample simulation with parameters listed in Appendix. The colors of the nodes correspond to the distance between node and its neighbors. **c**, "Fossil record" of *E. coli* density on the moving interface.

To simulate the interface dynamics beyond the linear regime, we also constructed a discrete model of the continuous interface by replacing it with a closed chain of nodes connected by straight links (Fig. 3.4a bottom). Each node carries a fixed amount of *E. coli*, so the local density of nodes per unit length of the interface corresponds to the local density of *E. coli*. Nodes are driven by a constant outwards expansion force F_0, surface tension, and a friction force that is proportional to the window-weighted average density of nodes per unit length. Additionally, we introduced

short-range repulsive forces between nodes and between nodes and links, to prevent self-crossing of the interface. Detailed description of this model is also given in Appendix.

As an initial condition, we assumed that the chain forms a circle with nodes slightly perturbed from equidistant positions. Figure 3.4b shows time-lapse snapshots of the interface in a sample simulation. Fig. 3.4c shows the aggregate image of the interface during the colony expansion, with the color of a point corresponding to density of nodes when the interface passed through that point. Assuming that a fixed fraction of *E. coli* is left behind the interface, this interface "fossil record" should roughly correspond to the density of *E. coli* inside the colony. At the beginning, the interface remains nearly circular, but initial perturbations quickly grow as the colony expands, producing large front undulations. Regions with lower node density expand more quickly because they experience less friction, and this expansion stretches the chain and further reduces the node density per unit length, creating a positive feedback loop. Concave regions, on the contrary, accumulate nodes and thus move outward more slowly. Eventually, cusps are formed in these lagging regions that have very high node density and therefore move very slowly, if at all. The regions on both sides of the cusp continue to expand toward each other and eventually "collide". After collision they form "double-layers" that remain nearly static and only increase in length as the overall interface expands further. Thus, "branches" with high concentration of *E. coli* form. As the front continues to expand, the interface already containing branches continues to undulate and form new cusps. This causes the earlier branches to merge, similar to what we observed in experiments (Fig. 3.2b). These simulation results suggest that indeed branch formation and merging can be explained by mechanics of a resistive ring surrounding a colony, which is stretched by the colony expansion. However, since this model neglects *E. coli* growth, the average density of nodes per unit length gradually decays, and eventually, the front instability ceases, in divergence with experimental results. To account for cell growth as well as for the diffusive leakage of *E. coli* from the interface into the bulk of the expanding colony, we developed a more elaborate 2D model of the growing multi-species colony.

3.2.5 Phase-field model of flower-like pattern formation

We also developed a more detailed two-dimensional, multi-component model of the expanding bacterial colony that is conceptually similar to the phase-field models used for description of eukaryotic cell motility and migration [19, 20, 21] (Fig. 3.5a). It is based on three PDEs for the densities of *A. baylyi* ρ_A, *E. coli* ρ_E, and the phase field ϕ that changes continuously from 1 inside the colony to 0 outside (see Appendix for the detailed formulation of the model). The latter is introduced to avoid computational difficulties of dealing with the sharp colony interface. All three components are diffused and advected by the velocity field that is generated by a combination of stress due to cell growth and motility, viscosity, and bottom friction that is proportional to the local *E. coli* density.

When we initialized the model with small circular domains of either pure *E. coli* or *A. baylyi*, the colony boundaries remained circular, and no patterns emerged (Fig. 3.5b). Consistent with the experiments, the *E. coli* colony only slightly expanded, while the *A. baylyi* colony expanded rapidly (Fig. 3.5c). When we initialized the model with a mixture of *A. baylyi* and *E. coli*, the colony grew at an intermediate speed (Fig. 3.5c), as in the experiments (Fig. 3.1d). The mixed colony simulations also exhibited front instability leading to formation of branches of *E. coli* (Fig. 3.5d, the snapshots of *A. baylyi* are shown in Fig. 3.11). As the colony grew, the branches merged and expanded, and a flower-like pattern developed. The *E. coli* density, colony boundary curvature and expansion speed can be analyzed using the same method we used for experimental data shown in Fig. 3.2c,d, which also shows the anti-correlation between *E. coli* density and local speed (Fig. 3.12).

Agar concentration is known to have a strong effect on the motility of bacteria [9] and their adhesion to the agar surface [22], so we reasoned that in our phase-field model changing agar concentration could be simulated by changing friction parameters. The frictional force in our model consists of two contributions: a small basal friction (characterized by parameter ξ) and stronger contribution proportional to the local *E. coli* concentration with coefficient β. Thus, to

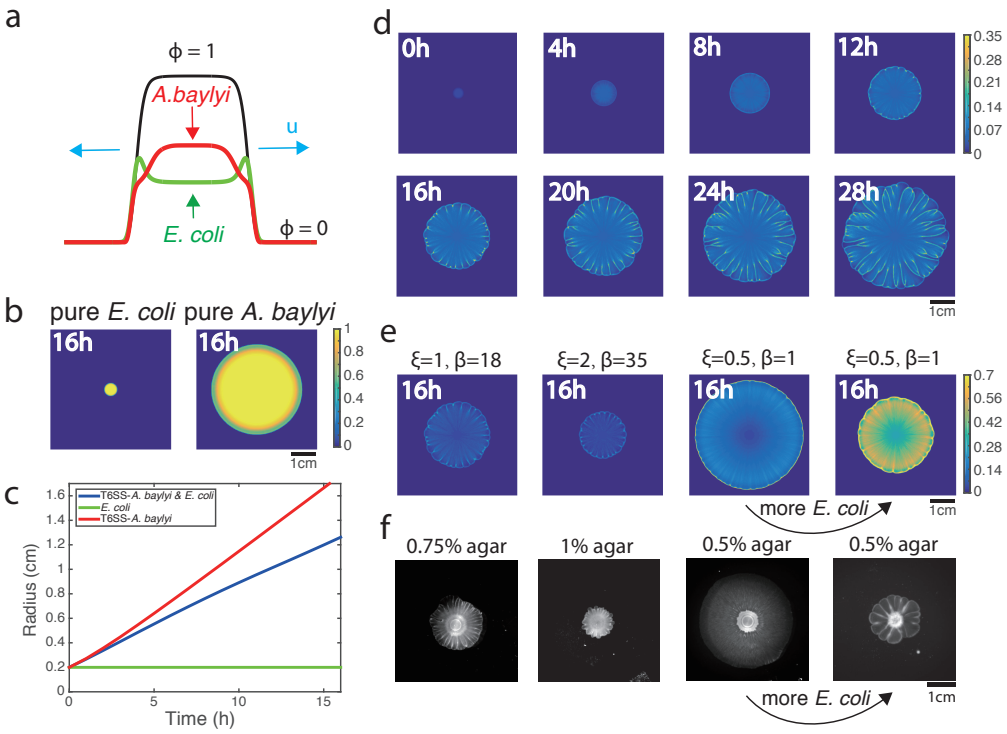

Figure 3.5: Phase-field model simulations of two-species colony growth. **a**, Illustration of the model. **b**, Snapshots of the colonies of pure *E. coli* and pure *A. baylyi* at $t = 12$. A colony of *E. coli* expanded only slightly, while a pure colony of *A. baylyi* expanded quickly, but remained circular. **c**, Colony radius vs time for the mixed and single-species colonies. Radius is defined as $\sqrt{\text{colony area}/\pi}$. **d**, Several snapshots of *E. coli* density during the growth of a mixed colony in simulations. **e**, Colony snapshots at time $t = 16$ in simulations using different friction parameters. For larger friction, the colony grew slower, but still featured flower-like patterns. For smaller friction, the colony expanded more quickly, but patterns eventually disappeared. However, increasing the initial concentration of *E. coli* at low friction coefficients restored patterning. **f**, Experimental snapshots with different agar concentrations 16 hours after inoculation: similar phenomenology observed.

mimic different agar concentrations, we varied both ξ and β. The leftmost panel in Fig. 3.5e shows the colony snapshots at $t = 16$ for the same parameter values as the time-lapse sequence in Fig. 3.5d. The next panel corresponds to larger ξ and β (presumably, higher agar concentration), where as expected, the colony expanded slower. The third panel shows the snapshot for smaller ξ and β (lower agar concentration), in which case the colony expands fast, but no patterns emerge. However,

for the same low ξ and β, when we started a simulation from 10x higher *E. coli* density, the friction provided by *E. coli* increased, and patterning re-emerged (Fig. 3.5e, fourth panel).

These numerical predictions were fully validated by experiments in which we varied the agar concentration and the initial density ratio of *E. coli* and T6SS$^-$ *A. baylyi*. The leftmost panel in Fig. 3.5f shows the snapshot of the colony started from 1:1 mixture after 16 hours of growth on 0.75% agar surface. When we increased the agar concentration to 1% (Fig. 3.5f, second panel), the colony expanded slower but the flower-like pattern emerged. Conversely, for low agar concentration (0.5%), colony grew fast but patterns were completely eliminated (Fig. 3.5f, third panel). However, for the same 0.5% agar concentration but A:E=1:100 initial density ratio, the flower-like pattern formation was rescued (Fig. 3.5f, fourth panel).

3.3 Discussion

Motility plays a key role in the spread of dense bacterial colonies. In this paper, we studied the structure of growing colonies comprised of two bacterial species, *E. coli* and *A. baylyi*, with very different motilities. Not only did the highly-motile species (*A. baylyi*) accelerate the spread of the slow species (*E. coli*), but the structure of the expanding colony quickly became highly heterogeneous and eventually produced very intricate, flower-like patterns.

Pattern formation in growing colonies of single bacterial species has been studied extensively [23, 24, 25, 26], and branching patterns were often found in these experiments. The emergence of these patterns is usually driven by nutrient limitation and ensuing chemotaxis, with agar concentration also having a strong effect on their morphology. For example, colonies expand homogeneously on soft agar rich with nutrients, but under nutrient limitation and in semi-solid agar, complex patterns emerge [24, 26]. In our system, however, we used rich LB media, and single-species colonies in the same conditions did not produce patterns. This suggested that the mechanism of

pattern formation here was different. We also found no significant differences in pattern formation with T6SS$^+$ and T6SS$^-$ strains of *A. baylyi*. In fact, we did not observe noticeable killing of *E. coli* by T6SS$^+$ *A. baylyi* after a short initial period. We believe that an extracellular matrix may have played a role here, as recent studies showed that it protected bacteria from T6SS attacks from other species [27, 28]. Overall, our experiments and modeling provided strong evidence in favor of the mechanical nature of the pattern-forming instability, arising from the interplay between outward pressure generated by the growth and high motility of *A. baylyi*, and the friction provided by sessile *E. coli* that adhere to the agar surface.

Ecologically, one of the primary challenges for any species is to maximize its geographic dispersal. Motility enables bacteria to escape from local stresses, move to locations with more nutrients, or invade host tissue [9]. However, motility, especially on hard surfaces, requires additional gene expression which could be a metabolic burden [6]. So some bacteria take advantage of other species with larger motility to colonize new niches. For example, by hitchhiking on zooplankton, water-borne bacteria can reach places that are otherwise inaccessible for them due to density gradients [29]. Non-motile Staphylococcal species hitchhike on swimming bacteria such as *Pseudomonas aeruginosa* [30]. In other studies, motile swarming *Paenibacillus vortex* was shown to transport non-motile *Xanthomonas perforans* [31] or *E. coli* [32] on agar surfaces. In our system, *A. baylyi* cells move by twitching instead of swarming, and our results suggest that slow-moving bacteria might take advantage of fast-moving twitching species by hitchhiking, or "surfing" along the expanding boundary, and thus spread farther. This can be seen clearly from the experiment in which *E. coli* and *A. baylyi* were inoculated separately at a small distance on agar surface. *A. baylyi* colony expanded and pushed *E. coli* to places where *E. coli* alone could not reach. Although *E. coli* and *A. baylyi* may not necessarily find themselves in the same ecological niche, bacteria with different motilities are ubiquitous in the environment [9]. Therefore, the mechanisms of codependent motility and pattern formation described here are likely to be broadly applicable in

natural habitats or even have implications in the transmission of pathogenic microbes. For example, *Acinetobacter baumannii*, an increasing threat in hospitals due to multi-drug resistance [33], is closely related to *A. baylyi* [34, 13] and also has twitching motility [35, 36], and thus other microbes which coexist with *A. baumannii* might also take advantage of its motility to spread.

3.4 Methods

3.4.1 Strains

We used *E. coli* MG1655 and *A. baylyi* ADP1 (ATCC #33305). The *E. coli* strain carried a plasmid that constitutively expressed mTFP and a kanamycin resistance gene. *A. baylyi* had a kanamycin resistance gene and the mCherry gene integrated in the genome. We also constructed a T6SS$^-$ *A. baylyi* ($\triangle$hcp) mutant by first fusing the tetracycline resistance marker from pTKS/CS to approximately 400 bp homology arms amplified from either side of hcp (ACIAD2689) in the *A. baylyi* genome, and mixing the donor oligo with naturally competent *A. baylyi*. The *pilTU*$^-$ strain was constructed similarly to delete the genes ACIAD0911-0912.

3.4.2 Culture conditions and image capturing

E. coli and *A. baylyi* cells were taken from -80°C glycerol stocks, inoculated in LB with appropriate antibiotics (kanamycin for *E. coli* and T6SS$^+$ *A. baylyi*, tetracycline for T6SS$^-$ *A. baylyi*) and grown at 37°C separately. When their OD600 reached about 0.3, both *E. coli* and *A. baylyi* were concentrated to OD=1, still separately. They were then mixed at specified volume ratios, and 3 μL was inoculated on the surface of 10 mL LB agar in the center of an 8.5 cm Petri dish. The plate was incubated at 37°C. The images were taken using a custom "milliscope" fluorescence imaging device unless indicated otherwise.

When the colony development was to be observed under a microscope, a 5.5 cm Petri dish was used with 15 mL 1% base agar (without LB) and top 10 mL LB agar (1% agar). After the cell culture was inoculated and dried, it was put on the stage of an inverted, epifluorescence microscope (Nikon TI2). The magnification was 4X. Fluorescent images were acquired using a 4X objective and a Photometrics CoolSnap cooled CCD camera in a 37°C chamber. The microscope and accessories were controlled using the Nikon Elements software.

The bacteria growth rates were measured in a Tecan plate reader.

3.4.3 Colony tracking

We adapted the method and the MATLAB™ code from [14] to track the colony boundary. The bright-field images were first segmented to identify the colony using an active contour method [37]. Then the colony boundary pixels were interpolated by a closed cubic spline and the boundary was parameterized by 300 virtual nodes, which were evolved in time as a coupled spring system (Fig. 3.13) [15]. For each node, three quantities were measured: brightness, extension speed and curvature. Brightness at each node was defined as the median of the neighboring pixels assigned to each node (see [14]). Extension speed was computed by the displacement of a node from frame t to frame $t+10$. Curvature was calculated by taking derivatives of the spline contour. Then the time series of these quantities were detrended and smoothed using FFT. An example of these quantities for all nodes at a particular time point is shown in Fig. 3.14. In Fig. 3.2d, we sampled 7 time points with 20 min interval from 9.5 h to 11.5 h and for each time point we plotted 100 nodes.

3.4.4 Mathematical models

Detailed description of the two models is given in Appendix.

3.5 Acknowledgements

We thank Megan Dueck for building the custom "milliscope" used in our study, Philip Bittihn for helpful discussions, and Kit Pogliano lab for providing the original *E. coli* strain. This work was supported by the National Institutes of Health (grant R01-GM069811), the National Science Foundation (grant PHY-1707637), San Diego Center for Systems Biology (NIH grant P50-GM085764) and the DOD Office of Naval Research (grant N00014-16-1-2093).

Chapter 3 contains material being prepared for submission as Xiong, L., Cao, Y., Cooper, R., Rappel, W.J., Hasty, J. and Tsimring, L., 2019. Flower-like patterns in multi-species bacterial colonies. The dissertation author was the primary investigator of this paper.

3.6 Appendix

3.6.1 Interface model

Continuous interface dynamics

To describe the motion of the interface separating the growing bacterial colony from the environment, we can use the framework originally proposed by Brower et al. [17, 18] for solidification patterns. The 1D interface (a closed line) at time t is specified by the position vector $\mathbf{x}(t,\sigma)$ where $0 < \sigma < 1$ is the variable parametrizing the interface such that $\mathbf{x}(t,0) = \mathbf{x}(t,1)$. Using the "orthogonal gauge" assumption that the velocity $d\mathbf{x}/dt$ is orthogonal to the tangent vector $\boldsymbol{\tau} = \partial\mathbf{x}/\partial\sigma$, the equation of motion for the interface can be written in the general form

$$\frac{d\mathbf{x}}{dt} = \hat{\mathbf{n}}\mathcal{F}(\mathbf{x}, \partial\mathbf{x}/\partial\sigma, ...) \tag{3.1}$$

where $\hat{\mathbf{n}}$ is the unit normal to the interface at $\mathbf{x}$ (perpendicular to $\boldsymbol{\tau}$) and $\mathcal{F}$ is the velocity functional that generally may depend on the overall interface position and other parameters. As Brower et al. [18] demonstrated, this equation can be transformed to the reference-frame independent *local* equations of motion for the local curvature κ and the curve metric $g = \boldsymbol{\tau} \cdot \boldsymbol{\tau}$ as a function of arclength s and time t:

$$\dot{\kappa} = -\left(\frac{\partial^2}{\partial s^2} + \kappa^2\right)\mathcal{F} \tag{3.2}$$

$$\dot{g} = 2g\kappa\mathcal{F} \tag{3.3}$$

Here the arclength is given by

$$s = \int_0^{\sigma} \sqrt{g(\sigma')}\, d\sigma' \tag{3.4}$$

and the curvature is defined by

$$\kappa = -\hat{\mathbf{n}} \cdot \frac{\partial^2 \mathbf{x}}{\partial s^2} \tag{3.5}$$

Now we need to specify the velocity functional $\mathcal{F}$ for our system in which a growing colony is surrounded by the thin band of highly frictional *E. coli* that hinders the colony expansion. Thus, we assume that $\mathcal{F}$ depends only on the local curvature κ and the local concentration of *E. coli* on the interface, c. This assumption will be violated if/when the interface will develop large folds and will attempt to "collide" with each other, then non-local terms in $\mathcal{F}$ become essential. We confine our continuous description here to sufficiently early times before this non-local interaction occurs. Under the additional simplifying assumption that the total amount of *E. coli* on the interface is conserved and neglecting their diffusion along the interface, the local concentration of *E. coli* will be inversely proportional to the square root of metric g, $c = c_0/\sqrt{g}$. In reality, of course, *E. coli*

also grows and is left behind in the bulk of the colony, but we assume that in a quasi-stationary regime these two processes approximately balance each other. Thus, the closed-form model for the interface expansion has the following form

$$\dot{\kappa} = -\left(\frac{\partial^2}{\partial s^2} + \kappa^2\right)\mathcal{F}(\kappa, c_0/\sqrt{g}) \tag{3.6}$$

$$\dot{g} = 2g\kappa\mathcal{F}(\kappa, c_0/\sqrt{g}) \tag{3.7}$$

For specificity, we assume that $\mathcal{F}$ has the following simple form:

$$\mathcal{F} = F_0 - \gamma\kappa - \alpha c \tag{3.8}$$

where F_0 is the maximal expansion velocity and c is the concentration of *E. coli* at the point $\mathbf{x}$ (defined by s or σ) on the interface at time t. This expression assumes that the expansion velocity is reduced in linear proportion to the local *E. coli* concentration c with proportionality coefficient α and is also subject to the linear surface tension with coefficient γ. Then, the model (3.6),(3.7) can be rewritten as

$$\dot{\kappa} = -\left(\frac{\partial^2}{\partial s^2} + \kappa^2\right)(F_0 - \gamma\kappa - \alpha c_0/\sqrt{g}) \tag{3.9}$$

$$\dot{g} = 2g\kappa(F_0 - \gamma\kappa - \alpha c_0/\sqrt{g}) \tag{3.10}$$

We can perform a linear stability analysis of a flat interface ($\kappa = 0, g = 1$) by substituting ansatz

$$\kappa = Ke^{iks+\lambda t} \tag{3.11}$$

$$g = 1 + Ge^{iks+\lambda t} \tag{3.12}$$

in Eqs. (3.9), (3.10). The Jacobian of the linearized system reads

$$J = \begin{bmatrix} -\gamma k^2 & \alpha c_0 k^2/2 \\ 2(F_0 - \alpha c_0) & 0 \end{bmatrix}. \tag{3.13}$$

For positive γ, α and $F_0 > \alpha c_0$ (the latter condition means that the colony with smooth interface is expanding), one of the two eigenvalues of this Jacobian is always positive. At small wavenumbers k, it increases linearly with k,

$$\lambda = \sqrt{\alpha c_0 (F_0 - \alpha c_0)} k \tag{3.14}$$

and for large k it reaches the maximum value

$$\lambda_m = \frac{\alpha c_0 (F_0 - \alpha c_0)}{\gamma} \tag{3.15}$$

Since the growth rate is positive for all values of k, this instability may lead to singularities in curvature (cusps). This is indeed what is found in numerical simulations of the discrete analog of this model (see the next section). These singularities correspond to the origins of "branches" of *E. coli* that the interface leaves behind during the flower pattern growth.

Flexible-chain interface model

The interface dynamics beyond linear instability stage can be analyzed numerically. Unfortunately, it is difficult to implement self-avoidance of the interface in the framework of the continuum model described in the previous section. Thus, we implemented a discrete flexible-chain model that is analogous to the continuum model described above but contains additional interaction terms between the nodes that prevent self-intersection of the chain. Specifically, we represent the interface as a closed chain of N nodes with coordinates $\mathbf{x}_i, i = 1, ..., N$. Let us introduce the vectors connecting node $i-1$ to node i (we assume that node 0 is the same as node N): $\mathbf{\Delta}_i = \mathbf{x}_i - \mathbf{x}_{i-1}$. Each

node is driven by the "expansion force" F_0 that acts along the unit vector $\hat{\mathbf{n}}_i$ that is directed outwards along the bisectrix of two adjacent edges, $\mathbf{\Delta}_i$ and $\mathbf{\Delta}_{i+1}$. It is counteracted by the "friction" force that is directed along $-\hat{\mathbf{n}}_i$ and is proportional to the local density of *E. coli* c_i associated with node i and by the surface tension force that is proportional to the local curvature of the interface κ_i. In addition, we introduce repulsion forces between all nodes and edges that prevent the interface from self-intersecting. The equation of motion in the overdamped limit can be written as follows:

$$\frac{d\mathbf{x}_i}{dt} = \hat{\mathbf{n}}_i(F_0 - \alpha c_i - \gamma\kappa_i) + \sum_{j\neq i} \mathbf{f}_{ij}^{nn} + \sum_{j\neq i} \mathbf{f}_{ij}^{ne} \tag{3.16}$$

The discrete analog of the local curvature at node i is defined as follows,

$$\kappa_i = \left| \frac{\mathbf{\Delta}_{i+1}}{\Delta_{i+1}} - \frac{\mathbf{\Delta}_i}{\Delta_i} \right| \frac{2}{\Delta_i + \Delta_{i+1}} \tag{3.17}$$

where $\Delta_i = |\mathbf{\Delta}_i|$.

We assume that each node carries the fixed "amount" of *E. coli* c, and the local concentration of *E. coli* c_i is defined as the average amount of c per unit length of the interface. In the simplest case, it can be computed as c/L_i where L_i is the half-sum of lengths of two edges attached to node i, $L_i = ½(\Delta_i + \Delta_{i+1})$, however in simulations we typically used longer averaging over 2 adjacent edges on both sides,

$$c_i = \frac{2(2K+1)c}{\sum_{j=-K}^{K}[\Delta_{i+j} + \Delta_{i+1+j}]} \tag{3.18}$$

with $K = 2$.

The last two terms in the r.h.s. of Eq.(3.16) represents the vector sum of possible repulsive forces acting on the node i from other nodes ($\mathbf{f}_{ij}^{nn}$) or edges ($\mathbf{f}_{ij}^{ne}$) of the chain. The node-node force acts along the vector connecting nodes i and j, $\mathbf{x}_i - \mathbf{x}_j$. We assume that the node-edge force acts

perpendicular to the orientation of the j-th link, Δ_j. We assume that the node-node force $\mathbf{f}_{ij}^{nn}$ is zero if $d_{ij}^{nn} = |\mathbf{x}_i - \mathbf{x}_j| > d_0$ and varies as $F_m(1 - d_{ij}^{nn}/d_0)^4$ for $d_{ij}^{nn} < d_0$ with large $F_m \ll F_0$. Similarly, the node-edge force $\mathbf{f}_{ij}^{ne}$ is zero if the distance between the node i and the edge j, $d_{ij}^{ne} > d_0$ and varies as $F_m(1 - d_{ij}^{ne}/d_0)^4$ for $d_{ij}^{ne} < d_0$.

Parameters

We used parameters below (Table 3.1) unless specified otherwise.

Table 3.1: Parameters for interface model.

F_0	α	γ	F_m	d_0	c	N	dt
1	0.5	10^{-8}	0.1	0.01	1	512	0.001

3.6.2 Phase-field model

Model description

In this more elaborate 2D model of a two-strain colony, we consider it as a growing mass of compressible fluid. A convenient way to describe a compact expanding colony is to use a phase-field approach where the phase ϕ changes smoothly from 0 outside the colony to 1 inside. The evolution of phase field ϕ is given by the equation:

$$\frac{\partial \phi}{\partial t} = -\mathbf{u} \cdot \nabla \phi + \Gamma(\varepsilon \nabla^2 \phi - G'(\phi)/\varepsilon + \kappa\varepsilon|\nabla\phi|) \tag{3.19}$$

where $\mathbf{u}$ is the velocity field, $\kappa = -\nabla \cdot (\nabla\phi/|\nabla\phi|)$ is the local interface curvature, and ε characterizes the interface width. The term $G(\phi) = 18\phi^2(1-\phi)^2$ is included to force the bistable dynamics of ϕ field with two stable fixed points at 0 and 1. The dynamics of the *A. baylyi* cells density ρ_A within

the colony is described by

$$\frac{\partial(\phi\rho_A)}{\partial t} + \nabla\cdot(\phi\rho_A\mathbf{u}) = \nabla\cdot(\phi D_A\nabla\rho_A) + \alpha_A\phi\rho_A(1-\rho_A-\rho_E) \tag{3.20}$$

The second term in the left-hand side is the advection term while the two terms in the right-hand side are diffusion and growth terms respectively. D_A and α_A are the diffusion constant and growth rate of *A. baylyi* respectively. The growth term follows logistic form and we assume that the growth can be saturated when the total density of *A. baylyi* (ρ_A) and *E. coli* (ρ_E) reaches 1. Note that the densities of two species are already scaled here.

Similarly, the dynamics for *E. coli* cells density ρ_E is described by

$$\frac{\partial(\phi\rho_E)}{\partial t} + \nabla\cdot(\phi\rho_E\mathbf{u}) = \nabla\cdot(\phi D_E\nabla\rho_E) + \alpha_E\phi\rho_E(1-\rho_A-\rho_E) \tag{3.21}$$

where D_E and α_E are the diffusion rate and growth rate of *E. coli*. Note that the advection of the phase field and both cell densities is provided by the same velocity field $\mathbf{u}$.

The velocity field could be determined by the overdamped Stokes equation:

$$\nabla\cdot[\nu(\phi)(\nabla\mathbf{u}+\nabla\mathbf{u}^{\mathbf{T}})] + \nabla\cdot(\chi\sigma_A) - [\xi+\beta f(\rho_E)\phi]\mathbf{u} = 0 \tag{3.22}$$

where $\nu(\phi) = \nu_0\phi$ is the viscosity, $\sigma_A = -\eta\phi\rho_A\mathbf{I}$ is the stress provided by motile *A. baylyi* cells ($\mathbf{I}$ is the identity matrix). χ is a random number uniformly distributed between $1\pm\Delta$, which adds noise to the stress driven by *A. baylyi*. Because pure *E. coli* colony expands very slowly and pure *A. baylyi* colony expands fast, we assume that the stress provided by *E. coli* is negligible compared to *A. baylyi*. Our experiments with mixtures of *E. coli* and *A. baylyi* show that regions where there are more *E. coli* move outward more slowly, so we assume that *E. coli* cells provide friction to prevent colony from expanding fast. This is described by the last term in which ξ is the basal friction

constant and $f(\rho_E) = \rho_E$ determines how the friction is modulated by *E. coli* cells. Here we assume it is simply proportional to ρ_E.

In reality, as the colony expands, the nutrients in the media are expected to get depleted over time at the center of the colony. In the experiment, we use rich LB media. Besides, since the interesting dynamics of the pattern formation mainly happens at the colony boundary, and the pattern inside the colony does not change once it forms, we do not include the nutrient diffusion and uptake in our model. Actually, in our model, the growth of bacteria saturates once the total density reaches 1. This effect is similar to nutrient depletion at the center of the colony which could stop the growth.

Parameters

Parameters of simulations on 0.75% LB agar are shown in Table 3.2. Some of these parameters (such as growth rates α_E and α_A) are known from experiments, while others had to be plausibly hypothesized. For example, the diffusion constants for bacterial motion are only known very roughly [24, 38], but since *A. baylyi* is motile and *E. coli* is not, we chose the diffusion constant of *A. baylyi* to be two orders of magnitude higher than that of *E. coli*.

Our simulations showed that viscosity and diffusion terms did not play significant roles in the dynamics. Changing D_A had little effect on the colony expansion speed and the pattern formation (Fig. 3.15). The reduction of ν_0 makes colony expand faster but the flower-like pattern still forms (Fig. 3.15). On the contrary, the stress and friction terms play major roles in our model. For the stress term, η is chosen to make the expansion speed of pure *A. baylyi* colony similar to experiment measurement. We also added white uniformly-distributed noise (with magnitude Δ) to the stress term to break the circular symmetry and induce the front instability. When Δ is small, the colony front instability also occurs, but at a later time point and merging of branches is not obvious (Fig. 3.15, first row), so we choose $\Delta = 0.3$ in our simulations.

Table 3.2: Parameters for phase-field model.

Γ	ε	D_A	α_A	D_E	α_E
0.008 cm/h	0.16 cm	0.0024 cm^2/h	1.2 h^{-1}	4×10^{-5} cm^2/h	1.3 h^{-1}

ν_0	η	ξ	β	Δ	Δx	Δy	Δt
0.0036 cm^2	0.03 cm^2/h	1	18	0.3	0.01 cm	0.01 cm	1×10^{-4} h

Note that if parameters ν_0, η, ξ, β are multiplied by the same constant factor, the velocity as determined by Eq. 3.22 will not change. So we set arbitrarily $\xi = 1$ and chose other parameters ν_0, η, β relative to ξ.

To model the changes in the agar concentration (Fig. 3.5e), we changed ξ and β while keep ν_0 and η the same. As shown in Fig. 3.5e, for the simulation for 0.5% LB agar, $\xi = 0.5, \beta = 1$ and for the simulation for 1% LB agar, $\xi = 2, \beta = 35$. The colony radii after 14 h in simulations are illustrated in Fig. 3.16 which can be compared to Fig. 3.7. Note that in Fig. 3.7, we show the experimental data after 16 h of growth because in experiments, the colonies only begin to expand 2 to 3h after innoculation, while in simulations the colonies begin to expand immediately.

Numerical algorithm

The numerical algorithm is similar to [21]. We aim to solve Eqns. 3.19-3.22 with uniform spatial grid sizes $\Delta x, \Delta y$ and fixed time step Δt from initial conditions $\phi^0, \rho_A^0, \rho_E^0, \mathbf{u}^0$. The system variables at time $t = n\Delta t$ are denoted as $\phi^n, \rho_A^n, \rho_E^n, \mathbf{u}^n$.

We first solve Eq. 3.19 by forward Euler scheme:

$$\phi^{n+1} = \phi^n - \Delta t \mathbf{u}^n \cdot \nabla\phi^n + \Delta t\Gamma[\varepsilon\nabla^2\phi^n - G'(\phi^n)/\varepsilon + \varepsilon\kappa^n|\nabla\phi^n|]$$

with κ^n calculated by $\kappa^n = -\nabla\cdot(\nabla\phi^n/|\nabla\phi^n|)$ when $|\nabla\phi^n| > 0.05$, and set to 0 otherwise.

The reaction-diffusion-advection equations for ρ_A and ρ_E are discretized using the forward

Euler scheme:

$$\phi^n \frac{\rho^{n+1}-\rho^n}{\Delta t} + \frac{\phi^{n+1}-\phi^n}{\Delta t}\rho^n = \text{Advection+Diffusion+Reaction} \tag{3.23}$$

where ϕ^{n+1} is obtained from the above step, and ρ^{n+1} is only updated when $\phi^n > 10^{-4}$. The advection term is calculated by

$$\begin{aligned}[\nabla\cdot(\phi^n\rho^n\mathbf{u}^n)]_{ij} &= (\phi^n_{i+1/2,j}\rho^n_{i+1/2,j}u^n_{i+1/2,j} - \phi^n_{i-1/2,j}\rho^n_{i-1/2,j}u^n_{i-1/2,j})/\Delta x \\ &\quad +(\phi^n_{i,j+1/2}\rho^n_{i,j+1/2}v^n_{i,j+1/2} - \phi^n_{i,j-1/2}\rho^n_{i,j-1/2}v^n_{i,j-1/2})/\Delta y\end{aligned}$$

and for the diffusion term

$$\begin{aligned}[\nabla\cdot(\phi^n D\nabla\rho^n)]_{ij} &= D[\phi_{i+1/2,j}\frac{\rho_{i+1,j}-\rho_{i,j}}{\Delta x} - \phi_{i-1/2,j}\frac{\rho_{i,j}-\rho_{i-1,j}}{\Delta x}]/\Delta x \\ &\quad +D[\phi_{i,j+1/2}\frac{\rho_{i,j+1}-\rho_{i,j}}{\Delta y} - \phi_{i,j-1/2}\frac{\rho_{i,j}-\rho_{i,j-1}}{\Delta y}]/\Delta y\end{aligned}$$

where $\mathbf{u}=(u,v)$, $\phi_{i\pm1/2,j}=(\phi_{i\pm1,j}+\phi_{i,j})/2$, $\phi_{i,j\pm1/2}=(\phi_{i,j\pm1}+\phi_{i,j})/2$, and we used the same definitions for ρ, u and v between collocation points. Then we can calculate ρ^{n+1} from Eqn. 3.23.

The Stokes equation Eq. 3.22 is integrated by the semi-implicit Fourier spectral method [21, 39] (to stabilize the scheme, we subtract the term $\nu_0\phi_0\nabla^2\mathbf{u}$ from both sides of Stokes equation with large constant ϕ_0, e.g. $\phi_0=200$):

$$\xi\mathbf{u} - \nu_0\phi_0\nabla^2\mathbf{u} = \nu_0\nabla\cdot[\phi\nabla\mathbf{u}^T + (\phi-\phi_0)\nabla\mathbf{u}] + \nabla\cdot(\chi\sigma_A) - \beta f(\rho_E)\phi\mathbf{u}$$

To obtain $\mathbf{u}^{n+1}$, we set $\mathbf{u}_0^{n+1}=\mathbf{u}^n$ and solve the equation below iteratively using spectral Fourier

method:

$$\xi \mathbf{u}_{k+1}^{n+1} - \nu_0 \phi_0 \nabla^2 \mathbf{u}_{k+1}^{n+1} = \nu_0 \nabla \cdot [\phi^{n+1} \nabla \mathbf{u}_k^{T,n+1} + (\phi^{n+1} - \phi_0) \nabla \mathbf{u}_k^{n+1}] + \nabla \cdot (\chi \sigma_A)^{n+1} - \beta f(\rho_E^{n+1}) \phi^{n+1} \mathbf{u}_k^{n+1}$$

where $k = 0, 1, 2, \cdots$ are iteration steps. In simulations, we constrain the error by iterating the above process until

$$\max |\mathbf{u}_k^{n+1} - \mathbf{u}_{k-1}^{n+1}| < 0.01 \max |\mathbf{u}_k^{n+1}|$$

or until $k_{max} = 200$, and the final $\mathbf{u}^{n+1} = \mathbf{u}_m^{n+1}$.

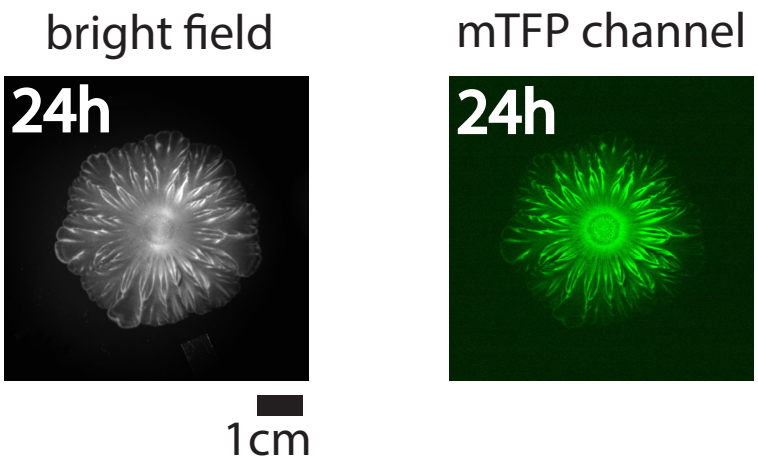

Figure 3.6: Bright-field image (left) and mTFP channel image (right) for the flower-like pattern after 24 hours of growth under milliscope.

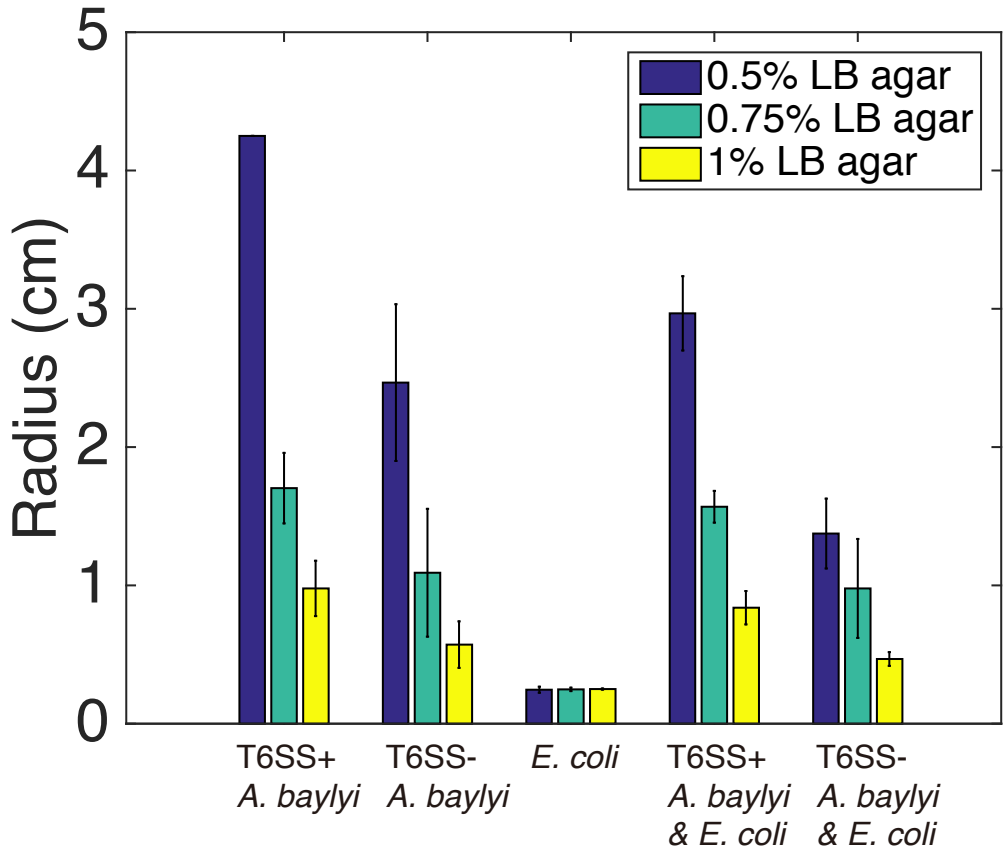

Figure 3.7: Colony radii after 16 hours of growth in 37°C for pure T6SS$^+$ *A. baylyi*, pure T6SS$^-$ *A. baylyi*, pure *E. coli*, mixture of T6SS$^+$ *A. baylyi* and *E. coli* with 1:1 initial density ratio, mixture of T6SS$^-$ *A. baylyi* and *E. coli* with 1:1 initial density ratio with different agar concentrations (10 mL LB agar). For pure T6SS$^+$ *A. baylyi* on LB agar (0.5% agar) plate, after 16 hours, the colony already reached the edge of the plate, so the radius of the plate is shown here. For each combination, experiments were run in triplicate.

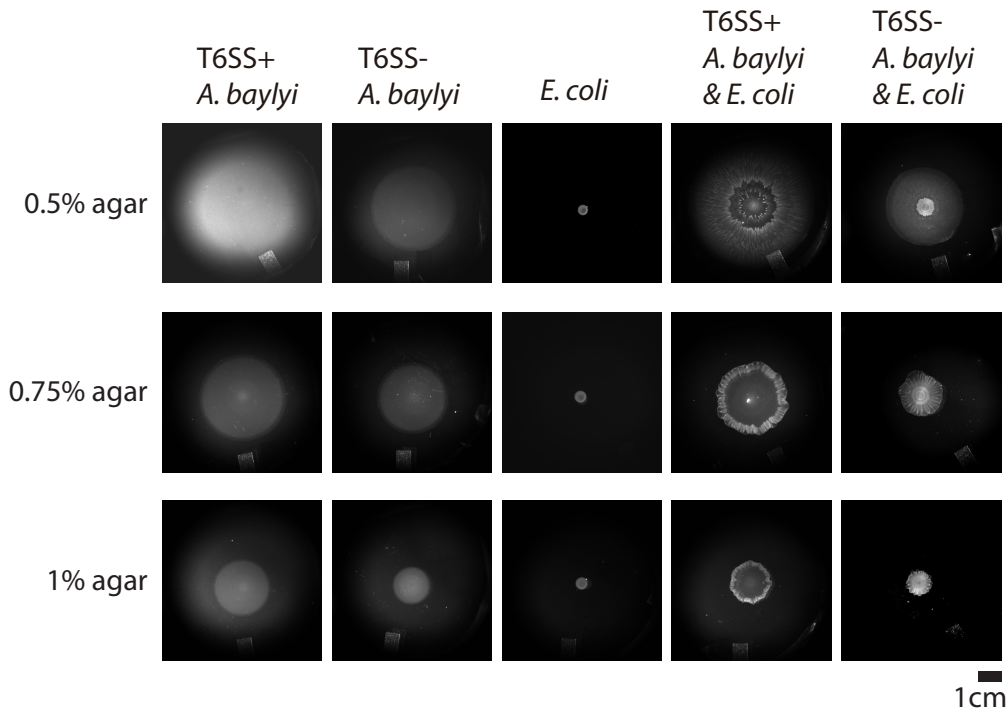

Figure 3.8: Examples of the colonies for all combinations of *E. coli* and *A. baylyi* with different agar concentrations after 16 hours of growth on 10 mL LB agar. When *A. baylyi* and *E. coli* were mixed, the initial seeding density ratio was 1:1.

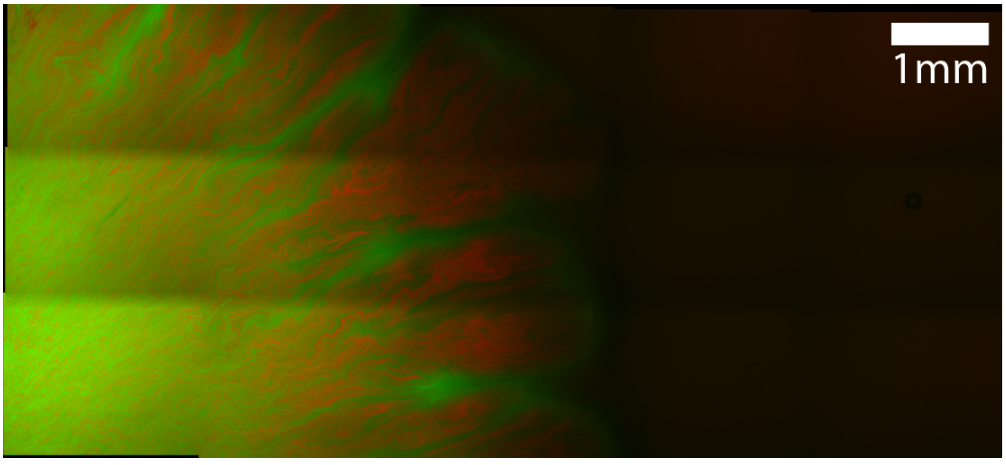

Figure 3.9: Microscope image of mixture of *E. coli* and T6SS$^-$ *A. baylyi* on agar surface. Red color shows *A. baylyi* (mCherry channel) while green color shows *E. coli* (mTFP channel).

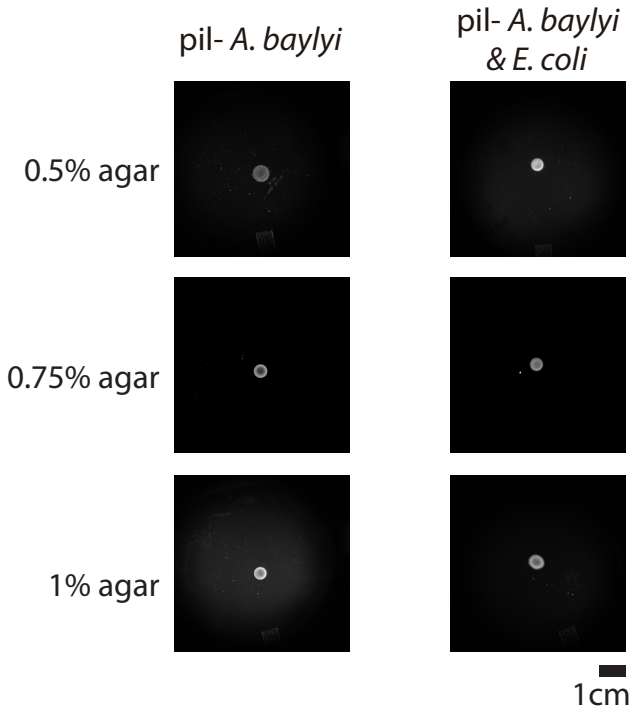

Figure 3.10: Examples of the colonies for pure pil$^-$ T6SS$^+$ *A. baylyi*, mixture of pil$^-$ T6SS$^+$ *A. baylyi* and *E. coli* with initial seeding density ratio 1:1 with different agar concentrations after 16 hours of growth on 10 mL LB agar.

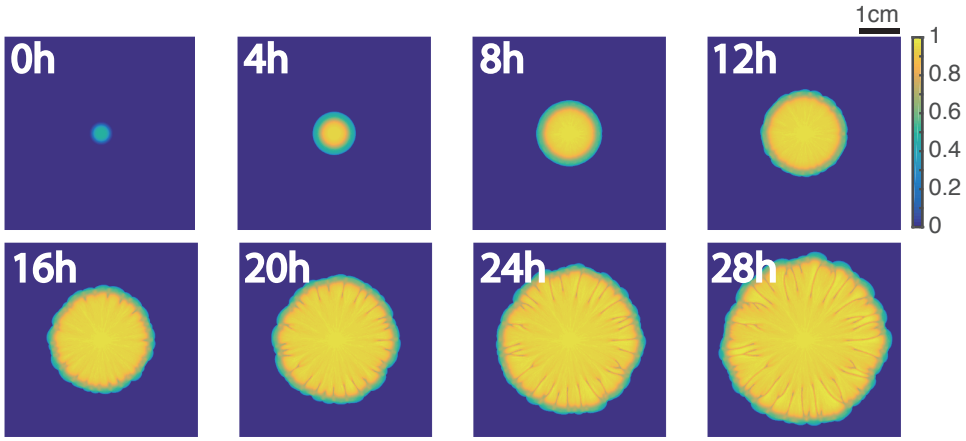

Figure 3.11: Several snapshots of *A. baylyi* density during the growth of a mixed colony in a phase-field model simulation.

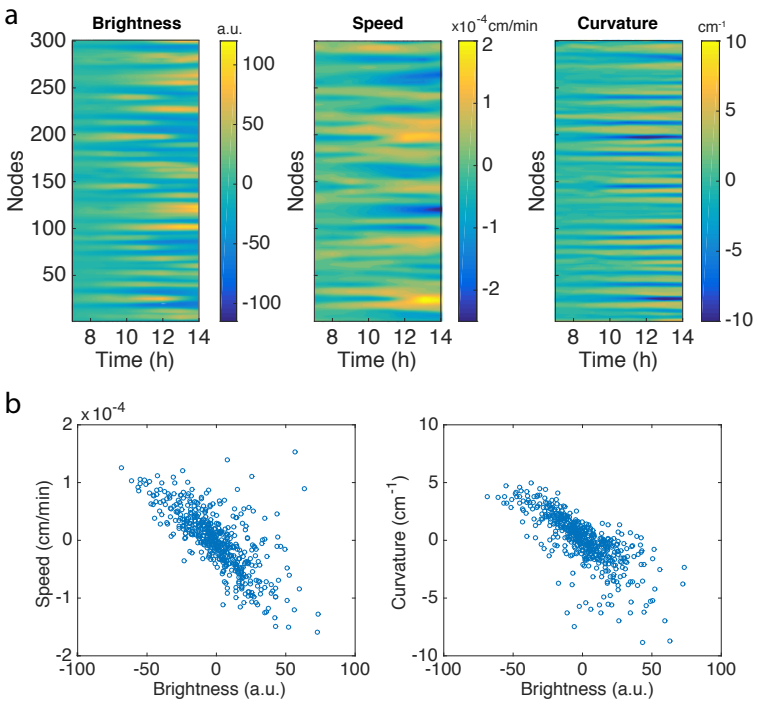

Figure 3.12: **a**, Kymographs of detrended brightness, speed and curvature along the colony boundary from the simulation in Fig. 3.5d. **b**, Scatter plots for detrended brightness vs. speed (left) and detrended brightness vs. curvature (right). Each circle corresponds to one virtual tracking node at one time point. Pearson coefficient for detrended brightness and speed is $\rho = -0.71$, and for detrended brightness and curvature is $\rho = -0.75$. Data points from 8 to 11 h are used in the scatter plot.

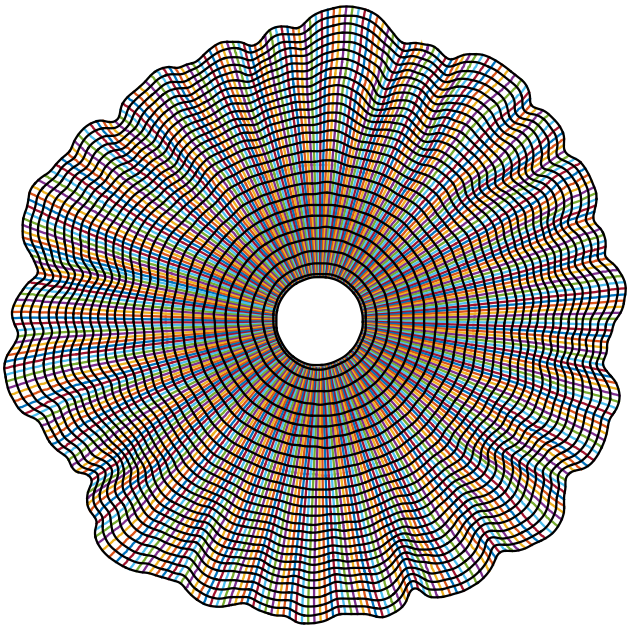

Figure 3.13: Examples of the tracked colony boundary and traces of 300 virtual nodes on the colony boundary. Black curves show the splines interpolated from the positions of 300 nodes at each time point. Different curves with colors show the traces of each node.

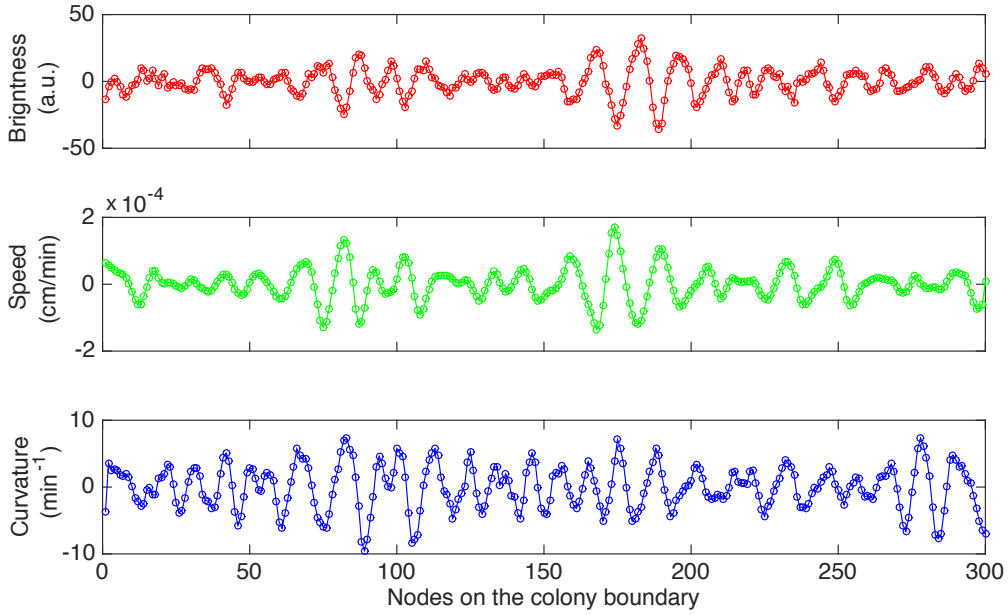

Figure 3.14: An example of the detrended brightness, speed and local curvature for all 300 nodes after 10 hours of colony growth in experiment.

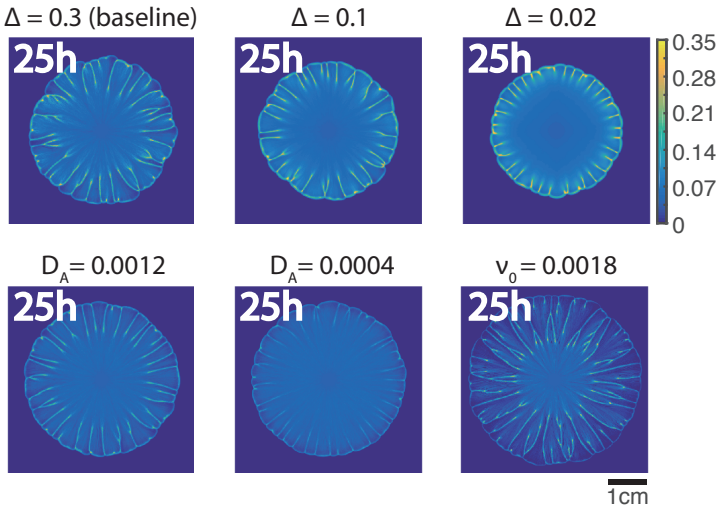

Figure 3.15: The influence of different parameters on the pattern formation in phase-field model. The parameters in Table 3.2 are used for the baseline simulation. For each snapshot, only one parameter (the parameter on top of each snapshot) is changed relative to the baseline simulation while other parameters stay the same.

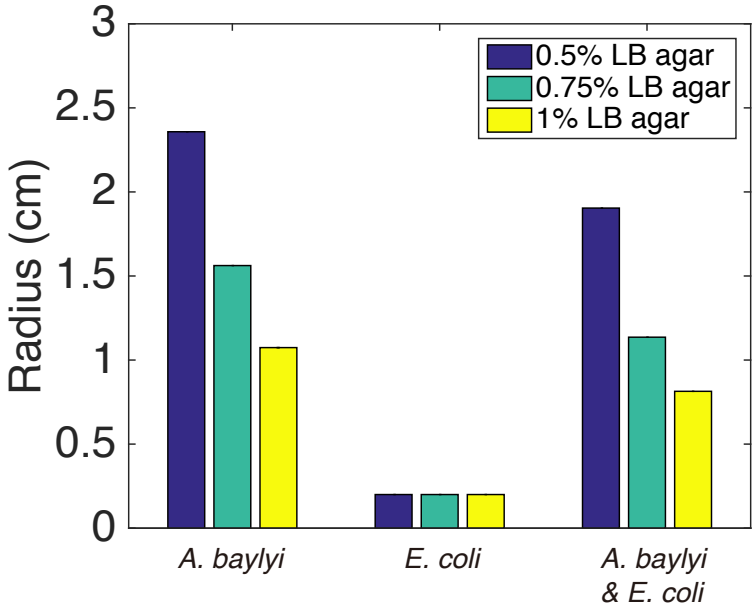

Figure 3.16: Colony radii after 14 h of growth in simulations. The parameters in Table 3.2 are used for the 0.75% LB agar simulation. For the simulation for 0.5% LB agar, $\xi = 0.5, \beta = 1$ and for the simulation for 1% LB agar, $\xi = 2, \beta = 35$.

References

[1] Munehiro Asally, Mark Kittisopikul, Pau Rué, Yingjie Du, Zhenxing Hu, Tolga Çağatay, Andra B Robinson, Hongbing Lu, Jordi Garcia-Ojalvo, and Gürol M Süel. Localized cell death focuses mechanical forces during 3d patterning in a biofilm. *Proceedings of the National Academy of Sciences*, 109(46):18891–18896, 2012.

[2] Miguel Trejo, Carine Douarche, Virginie Bailleux, Christophe Poulard, Sandrine Mariot, Christophe Regeard, and Eric Raspaud. Elasticity and wrinkled morphology of bacillus subtilis pellicles. *Proceedings of the National Academy of Sciences*, 110(6):2011–2016, 2013.

[3] James N Wilking, Vasily Zaburdaev, Michael De Volder, Richard Losick, Michael P Brenner, and David A Weitz. Liquid transport facilitated by channels in bacillus subtilis biofilms. *Proceedings of the National Academy of Sciences*, 110(3):848–852, 2013.

[4] Dmitri Volfson, Scott Cookson, Jeff Hasty, and Lev S Tsimring. Biomechanical ordering of dense cell populations. *Proceedings of the National Academy of Sciences*, 105(40):15346–15351, 2008.

[5] Joao B Xavier, Esteban Martinez-Garcia, and Kevin R Foster. Social evolution of spatial patterns in bacterial biofilms: when conflict drives disorder. *The American Naturalist*, 174(1):1–12, 2009.

[6] Daniel B Kearns. A field guide to bacterial swarming motility. *Nature Reviews Microbiology*, 8(9):634, 2010.

[7] Denis Boyer, William Mather, Octavio Mondragón-Palomino, Sirio Orozco-Fuentes, Tal Danino, Jeff Hasty, and Lev S Tsimring. Buckling instability in ordered bacterial colonies. *Physical biology*, 8(2):026008, 2011.

[8] Alexandre Persat, Carey D Nadell, Minyoung Kevin Kim, Francois Ingremeau, Albert Siryaporn, Knut Drescher, Ned S Wingreen, Bonnie L Bassler, Zemer Gitai, and Howard A Stone. The mechanical world of bacteria. *Cell*, 161(5):988–997, 2015.

[9] Rasika M Harshey. Bacterial motility on a surface: many ways to a common goal. *Annual Reviews in Microbiology*, 57(1):249–273, 2003.

[10] Mariana Bitrian, Rodrigo H González, Gaston Paris, Klaas J Hellingwerf, and Clara B Nudel. Blue-light-dependent inhibition of twitching motility in acinetobacter baylyi adp1: additive involvement of three bluf-domain-containing proteins. *Microbiology*, 159(9):1828–1841, 2013.

[11] Colleen G Leong, Rebecca A Bloomfield, Caroline A Boyd, Amber J Dornbusch, Leah Lieber, Flora Liu, Amie Owen, Erin Slay, Kristine M Lang, and C Phoebe Lostroh. The role of core and accessory type iv pilus genes in natural transformation and twitching motility in the bacterium acinetobacter baylyi. *PloS one*, 12(8):e0182139, 2017.

[12] Sandra Schwarz, Rachel D Hood, and Joseph D Mougous. What is type vi secretion doing in all those bugs? *Trends in microbiology*, 18(12):531–537, 2010.

[13] Robert M Cooper, Lev Tsimring, and Jeff Hasty. Inter-species population dynamics enhance microbial horizontal gene transfer and spread of antibiotic resistance. *Elife*, 6:e25950, 2017.

[14] Monica Skoge, Micha Adler, Alex Groisman, Herbert Levine, William F Loomis, and Wouter-Jan Rappel. Gradient sensing in defined chemotactic fields. *Integrative Biology*, 2(11-12):659–668, 2010.

[15] Matthias Machacek and Gaudenz Danuser. Morphodynamic profiling of protrusion phenotypes. *Biophysical journal*, 90(4):1439–1452, 2006.

[16] Yuhua Zhan, Yongliang Yan, Wei Zhang, Ming Chen, Wei Lu, Shuzhen Ping, and Min Lin. Comparative analysis of the complete genome of an acinetobacter calcoaceticus strain adapted to a phenol-polluted environment. *Research in microbiology*, 163(1):36–43, 2012.

[17] Richard C Brower, David A Kessler, Joel Koplik, and Herbert Levine. Geometrical approach to moving-interface dynamics. *Physical review letters*, 51(13):1111, 1983.

[18] Richard C Brower, David A Kessler, Joel Koplik, and Herbert Levine. Geometrical models of interface evolution. *Physical Review A*, 29(3):1335, 1984.

[19] Danying Shao, Wouter-Jan Rappel, and Herbert Levine. Computational model for cell morphodynamics. *Physical review letters*, 105(10):108104, 2010.

[20] Danying Shao, Herbert Levine, and Wouter-Jan Rappel. Coupling actin flow, adhesion, and morphology in a computational cell motility model. *Proceedings of the National Academy of Sciences*, 109(18):6851–6856, 2012.

[21] Brian A Camley, Yanxiang Zhao, Bo Li, Herbert Levine, and Wouter-Jan Rappel. Periodic migration in a physical model of cells on micropatterns. *Physical review letters*, 111(15):158102, 2013.

[22] Kristopher W Kolewe, Shelly R Peyton, and Jessica D Schiffman. Fewer bacteria adhere to softer hydrogels. *ACS applied materials & interfaces*, 7(35):19562–19569, 2015.

[23] Hiroshi Fujikawa and Mitsugu Matsushita. Fractal growth of bacillus subtilis on agar plates. *Journal of the physical society of japan*, 58(11):3875–3878, 1989.

[24] Elena O Budrene and Howard C Berg. Complex patterns formed by motile cells of escherichia coli. *Nature*, 349(6310):630, 1991.

[25] Ido Golding, Yonathan Kozlovsky, Inon Cohen, and Eshel Ben-Jacob. Studies of bacterial branching growth using reaction–diffusion models for colonial development. *Physica A: Statistical Mechanics and its Applications*, 260(3-4):510–554, 1998.

[26] M Matsushita, J Wakita, H Itoh, Ismael Rafols, T Matsuyama, H Sakaguchi, and M Mimura. Interface growth and pattern formation in bacterial colonies. *Physica A: Statistical Mechanics and its Applications*, 249(1-4):517–524, 1998.

[27] Jonida Toska, Brian T Ho, and John J Mekalanos. Exopolysaccharide protects vibrio cholerae from exogenous attacks by the type 6 secretion system. *Proceedings of the National Academy of Sciences*, 115(31):7997–8002, 2018.

[28] Carlos Molina-Santiago, John R Pearson, Yurena Navarro, Maria Victoria Berlanga-Clavero, Andres Mauricio Caraballo-Rodriguez, Daniel Petras, Francisco M Cazorla, Antonio de Vicente, Pieter C Dorrestein, and Diego Romero. Extracellular matrix components are required to protect bacillus subtilis colonies from t6ss-dependent pseudomonas invasion and modulate co-colonization of plant. *bioRxiv*, page 429001, 2018.

[29] Hans-Peter Grossart, Claudia Dziallas, Franziska Leunert, and Kam W Tang. Bacteria dispersal by hitchhiking on zooplankton. *Proceedings of the National Academy of Sciences*, 107(26):11959–11964, 2010.

[30] Tahoura Samad, Nicole Billings, Alona Birjiniuk, Thomas Crouzier, Patrick S Doyle, and Katharina Ribbeck. Swimming bacteria promote dispersal of non-motile staphylococcal species. *The ISME journal*, 11(8):1933, 2017.

[31] Efrat Hagai, Reut Dvora, Tal Havkin-Blank, Einat Zelinger, Ziv Porat, Stefan Schulz, and Yael Helman. Surface-motility induction, attraction and hitchhiking between bacterial species promote dispersal on solid surfaces. *The ISME journal*, 8(5):1147, 2014.

[32] Alin Finkelshtein, Dalit Roth, Eshel Ben Jacob, and Colin J Ingham. Bacterial swarms recruit cargo bacteria to pave the way in toxic environments. *MBio*, 6(3):e00074–15, 2015.

[33] Lenie Dijkshoorn, Alexandr Nemec, and Harald Seifert. An increasing threat in hospitals: multidrug-resistant acinetobacter baumannii. *Nature reviews microbiology*, 5(12):939, 2007.

[34] Marie Touchon, Jean Cury, Eun-Jeong Yoon, Lenka Krizova, Gustavo C Cerqueira, Cheryl Murphy, Michael Feldgarden, Jennifer Wortman, Dominique Clermont, Thierry Lambert, et al. The genomic diversification of the whole acinetobacter genus: origins, mechanisms, and consequences. *Genome biology and evolution*, 6(10):2866–2882, 2014.

[35] Bart A Eijkelkamp, Uwe H Stroeher, Karl A Hassan, Michael S Papadimitrious, Ian T Paulsen, Melissa H Brown, and Reggie Lo. Adherence and motility characteristics of clinical acinetobacter baumannii isolates. *FEMS microbiology letters*, 323(1):44–51, 2011.

[36] Katy M Clemmer, Robert A Bonomo, and Philip N Rather. Genetic analysis of surface motility in acinetobacter baumannii. *Microbiology*, 157(9):2534–2544, 2011.

[37] Tony F Chan, B Yezrielev Sandberg, and Luminita A Vese. Active contours without edges for vector-valued images. *Journal of Visual Communication and Image Representation*, 11(2):130–141, 2000.

[38] Yeong-Chul Kim. Diffusivity of bacteria. *Korean Journal of Chemical Engineering*, 13(3):282–287, 1996.

[39] Long Qing Chen and Jie Shen. Applications of semi-implicit fourier-spectral method to phase field equations. *Computer Physics Communications*, 108(2-3):147–158, 1998.

Chapter 4

Agent-based modeling of bacterial population dynamics

Agent-based modeling is useful in studying bacterial population dynamics. In the continuous models, the cell populations are represented by fields which normally characterize the cell densities. In the agent-based models, each cell can carry a set of equations and is simulated individually. Each cell can be modeled as a spherocylinder of unit diameter that grows linearly along its axis and divides equally after reaching a critical length. It can also move along the plane due to forces and torques produced by interactions with other cells. The slightly inelastic cell-cell normal contact forces are computed using the standard spring-dashpot model and the tangential forces are computed as velocity-dependent friction. In the agent-based model, the cell-cell and cell-substrate interactions are considered which generates a more "realistic" characterization of bacterial population dynamics. Besides, the incorporation of both intra- and intercelluar dynamics makes it a multi-scale model. In this chapter, I will present two examples of the applications of agent-based modeling in exploring bacterial population dynamics.

4.1 Species-independent attraction to biofilms through electrical signaling

4.1.1 Experimental phenomena

Recently, bacterial cell-to-cell communication mechanism based on ion channel-mediated electrical signaling was discovered [1, 2]. It has also been shown in experiments that *B. subtilis* biofilms can periodically release potassium signals, producing electrical waves through and beyond the biofilms. Such long-range signaling could affect distant bacteria that are not part of the biofilm. More specifically, the distant motile cells are periodically attracted to the electrically oscillation biofilm (Fig. 4.1). Experimental evidence shows that extracellular potassium can direct cell motility by affecting the potassium ion channel activity and cell membrane potential which can modulate the tumbling frequency of distant cells.

4.1.2 Modeling

To integrate the above described experimental evidence into a coherent phenomenological framework, we turned to mathematical modeling. We utilized an electrophysiological model based on the mathematical framework developed by Hodgkin and Huxley [3] to predict changes in membrane potential in response to extracellular potassium.

Our agent-based model assumes that each motile cell changes its electrophysiological state and motility independently of each other and only in response to changes in extracellular potassium. We describe intracellular potassium-driven dynamics within each cell using a generalization of the electrophysiological model introduced in earlier paper [2]. The membrane potential is governed by the standard Hodgkin-Huxley-type conductance equation,

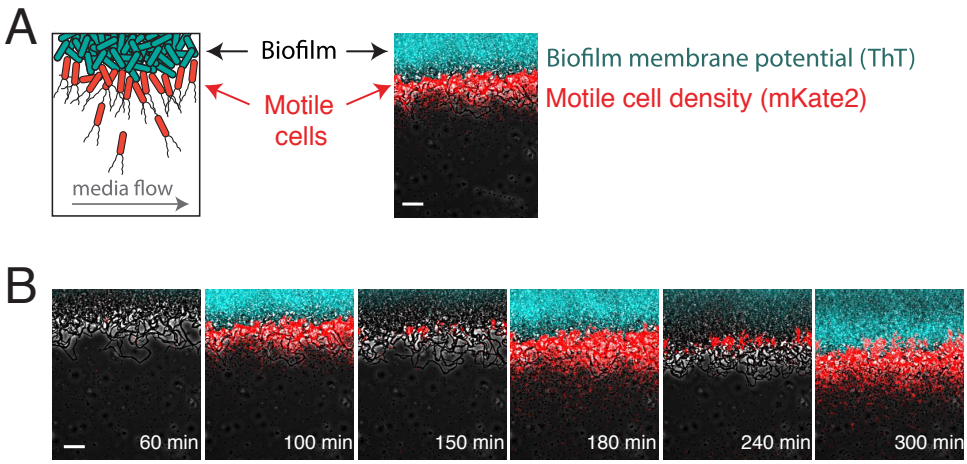

Figure 4.1: Distant motile cells are periodically attracted to an electrically oscillating biofilm. (A) Illustration of motile cell interaction with a biofilm within a shared microfluidic growth chamber. Membrane potential changes are reported by Thioflavin T (ThT, pseudocolored cyan), a cationic dye that acts as a Nernstian voltage indicator [2]. ThT fluorescence increases when the cell becomes more inside-negative, making ThT fluorescence inversely related to the membrane potential. Motile cells (pseudocolored red) express a fluorescent protein mKate2. Motile cell density is measured using mKate2 fluorescence in the 100 μm region outward from the biofilm edge. Scale bar, 50 μm. (B) Filmstrip showing the edge of a biofilm that is located on the top of each image. Images depict periodic motile cell attraction to an electrically oscillating biofilm and subsequent passive dispersal away from the biofilm. Gray (phase contrast), cyan (membrane potential), red (motile cells). Scale bar, 50 μm.

$$\eta C \frac{dV}{dt} = -g_K n^4 (V - V_K) - g_L (V - V_L) \tag{4.1}$$

in which C is the capacitance of the cell membrane. The first term in the right hand side describes the change in membrane potential by potassium ions escaping the cell through potassium ion channels, while the second term describes the leak current. In the standard Hodgkin-Huxley model, the membrane potential dynamics are very fast (milliseconds), much faster than the slow changes in extracellular potassium and corresponding changes in bacterial motility (hours). Since it is very difficult to simulate together processes of such vastly different timescales, we introduced a scaling factor η to slow down the intracellular electrophysiological dynamics. The scaling factor is also applied to Eqns. (4.4) and (4.5). As long as the electrophysiological processes remain much faster

than the slow part of the model, this did not have an appreciable effect on the slow dynamics of the cellular population. We used the value $\eta = 300$ and verified that changing this factor to 150 did not appreciably affect the results of our simulations.

The resting potentials V_K and V_L set by the ion pumps, and generally are dependent on both intra- and extracellular potassium levels, for which we assume a simple linear form,

$$V_K = V_{K0} + \delta_K(K_e + K_i) \tag{4.2}$$

$$V_L = V_{L0} + \delta_L(K_e + K_i) \tag{4.3}$$

The fourth power in the first term of Eq. (4.1) stems from the fact [4] that bacterial potassium channels are formed by four subunits, which on average are open during a fraction of time n whose dynamics is given by the following rate equation:

$$\eta \frac{dn}{dt} = \alpha(S)(1-n) - \beta n \tag{4.4}$$

where the first term describes channel opening and the second term specifies the rate of channel closing. As in [2], the opening rate α of the potassium channel is assumed to depend on metabolic stress, S, according to the Hill function $\alpha(S) = \alpha_0 S^m/(S_{th}^m + S^m)$. This metabolic stress variable that stands for the concentration of stress-related metabolic products [5], such as excess NAD+ [6, 7] is itself controlled by the membrane potential according to the equation

$$\eta \frac{dS}{dt} = \frac{\alpha_s(V_{th} - V)}{\exp(\frac{V_{th}-V}{\sigma}) - 1} - \gamma_S S \tag{4.5}$$

In departure from previous model in [2] that described time-dependent dynamics of the extracellular potassium in the dense biofilm environment, here we assume that motile cells have sufficiently low density and therefore do not change the extracellular potassium appreciably. Instead, we focus on

the concentration of the intracellular potassium K_i,

$$\frac{dK_i}{dt} = -\varepsilon g_K n^4 (V - V_K) + \beta_K (V_0 - V) \tag{4.6}$$

where the first term describes the flux of potassium through ion channels and the second term describes the action of potassium pumps which maintain the membrane potential at the resting value V_0. The second term only appears when $V_0 > V$ and is zero otherwise, because the ion pump can only pump the potassium from outside to inside of a cell.

It can be shown that the regulation of the intracellular potassium described by Eq. (4.6) plays the role of the integral feedback control loop similar to other mechanisms of bacterial chemotaxis [8]. Indeed, in the absence of stress $S \approx 0$, the ion channels are closed $n \approx 0$, and the membrane potential equilibrates near $V = V_0$ independently of the level of extracellular potassium (perfect adaptation). However, a change in extracellular potassium levels may cause complex transient changes in the membrane potential. When extracellular potassium level rises, according to Eq. (4.1) it slightly depolarizes the cell (increases V). The depolarization causes opening of the ion channels $n > 0$, intracellular potassium flushes out according to Eq. (4.6), and the cell becomes strongly hyperpolarized. Then the channels close, and the ion pumps restore the membrane potential to the resting value. If the level of extracellular potassium continues to rise, the process repeats, and a periodic sequence of depolarization pulses ensues (Fig. 4.2). If the level of extracellular potassium slowly decreases, it slightly hyperpolarizes the cell, but the channels remain closed, and the ion pump maintains the membrane potential close to the resting value. These transient changes in the membrane potential lead to changes in intracellular energy levels (we can think of this energy as PMF or ATP) and in turn lead to changes in the bacterial motility. We describe the energy dynamics

by the simple relaxation equation:

$$\frac{dE}{dt} = -\alpha_E V - \gamma_E E \tag{4.7}$$

and postulate that the tumbling probability is downregulated by the energy:

$$\mathscr{P} = \frac{K_E^q}{(E - E_0)^q + K_E^q} \tag{4.8}$$

The strong anisotropy in the dynamics of the membrane potential for increasing and decreasing extracellular potassium leads to the chemotactic response of motile bacteria to the spatial gradient of potassium (Fig. 4.2). Indeed, if a cell swims up the gradient, it experiences rising levels of potassium and strongly hyperpolarizes, thus increasing the mean proton motive force and the level of energy in the cell. Therefore, its tumbling probability diminishes, and the cell continues to swim in the same direction. However, when the cell swims down the potassium gradient, hyperpolarization does not occur, and the tumbling probability remains high.

To simulate bacterial motion, we adapted the mechanical agent-based model developed in our earlier work [9, 10]. Each cell is modeled as a spherocylinder of unit diameter that grows linearly along its axis and divides equally after reaching a critical length $l_d = 4$. It can also move along the plane due to forces and torques produced by interactions with other cells and its own flagella-mediated motility (however, we do not model the flagella dynamics explicitly). The slightly inelastic cell-cell normal contact forces are computed via the standard spring-dashpot model, and the tangential forces are computed as velocity-dependent friction. During periods of directed motion, the cell experiences a self-propelling force directed along its axis. During the periods of tumbling, the self-propelling directional force is switched off, and the cell experiences a strong random torque which quickly turns it in a random new direction. The probability of switching from directed motion to tumbling for each cell is controlled by variable $\mathscr{P}$ that is computed from the electrophysiological

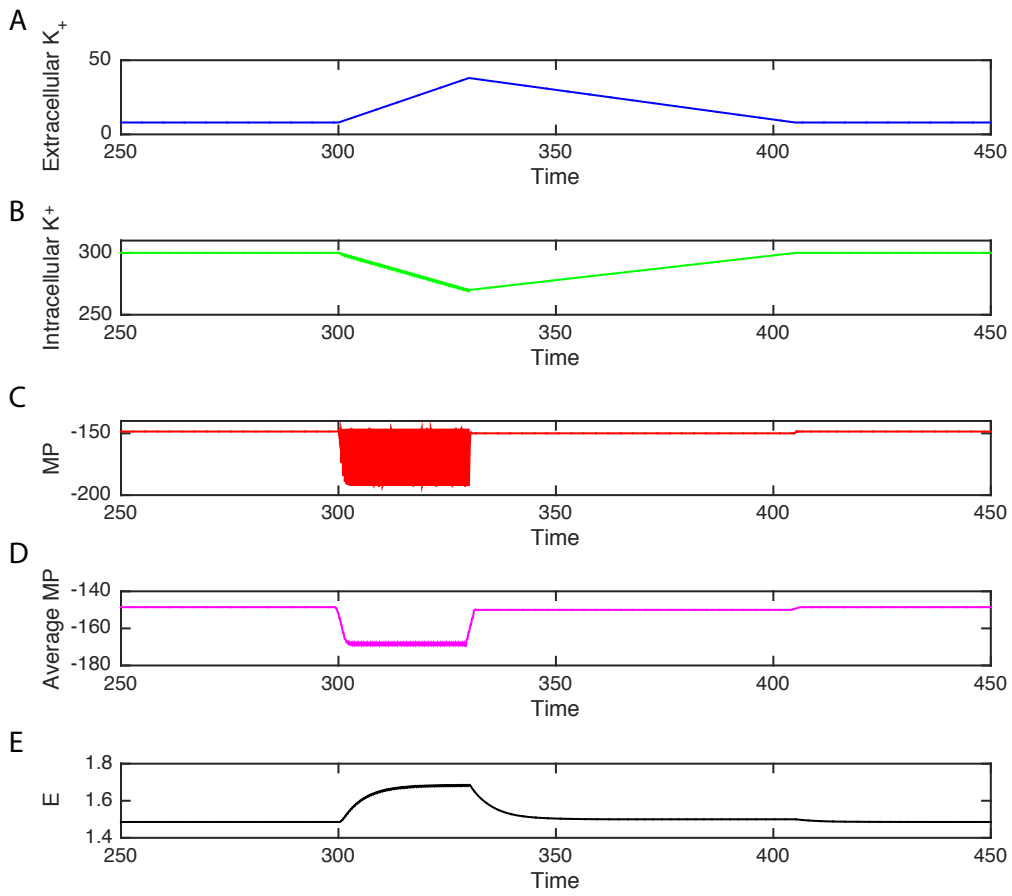

Figure 4.2: Mathematical modeling of the motile cell response to extracellular potassium released by a biofilm. (A) Extracellular potassium emitted from the biofilm over time. (B) Intracellular potassium in motile cells over time. (C) Instantaneous membrane potential (MP) in motile cells over time. (D) Average membrane potential in motile cells over time. (E) Average energy in motile cells over time.

cell model. Biofilm-bound cells were assumed to be non-motile (no self-propelling force, no tumbling torque).

The dynamics of extracellular potassium ion field were implemented via a reaction-diffusion model where the biofilm cells played the role of sources and sinks of potassium periodically,

$$\frac{\partial K_e(\mathbf{r})}{\partial t} = \sum_j f(t)\delta(\mathbf{r}-\mathbf{r}_j) + D_k \nabla^2 K_e(\mathbf{r}) \tag{4.9}$$

Here K_e is the extracellular potassium concentration and $\mathbf{r}_j$ is the location of the j-th cell, $f(t)$ is the periodic function describing periodic excretion (with rate α_k) and absorption (with rate $-\beta_k K_e$) cycles of extracellular potassium by the biofilm cells, and D_k is the potassium diffusion constant [11].

Each simulated motile "cell" carried a set of equations above describing its membrane potential dynamics in response to the local extracellular potassium concentration. The effect of the motile cells on the extracellular potassium concentration was ignored. The parameters of the model are shown in Table 4.1.

Table 4.1: Parameters for mathematical model.

Parameter	Value	Description	Source
g_K	36 mS/cm^2	potassium ion channel conductance per unit area	[3]
g_L	0.3 mS/cm^2	leak conductance per unit area	[3]
C	1 μF/cm^2	membrane capacity per unit area	[3]
V_{K0}	-688 mV	basal potassium resting potential	measurement
V_{L0}	-5694 mV	basal leak resting potential	measurement
δ_K	1 mV/mM	potassium sensitivity of potassium resting potential	[2]
δ_L	18 mV/mM	potassium sensitivity of leak resting potential	[2]
S_{th}	0.04 mM	metabolic stress constant	[2]
V_{th}	-148 mV	membrane potential threshold	measurement
α_0	0.12 ms^{-1}	maximal opening rate of potassium channel	[3]
β	0.156 ms^{-1}	potassium channel closing rate	[3]
m	1	opening rate Hill coefficient	[2]
σ	0.2 mV	steepness of the membrane potential stress response	[2]
γ_s	0.3 ms^{-1}	stress relaxation rate	fitting
α_s	0.03 mM/(ms mV)	membrane potential stress response rate	fitting
η	300	scaling factor	fitting
ε	7×10^3 (mM cm^2)/(mA min)	rate of potassium flux through the open channel	fitting
β_K	0.8mM/(min mV)	potassium pumping efficiency	fitting
V_0	-148 mV	pump resting potential	fitting
α_E	0.008 (min mV)$^{-1}$	PMF accumulation rate	fitting
γ_E	0.8 min^{-1}	PMF relaxation rate	fitting
E_0	1.535 mM	PMF basal value	fitting
q	7	tumbling rate Hill coefficient	fitting
K_E	0.002 mM	PMF threshold for tumbling rate change	fitting
α_k	64 mM/min	extracellular potassium production rate	fitting
β_k	400 min^{-1}	extracellular potassium consumption rate	fitting
D_k	8×10^4 μm^2/min	extracellular potassium diffusion constant	[11]

We performed multiple simulations in a narrow channel of length 100 and width 20 (Fig. 4.3B). The biofilm consisting of approximately 200 cells was initially grown in the back of the open channel ($100 \times 20\ \mu m^2$), after which 100 motile cells were introduced into the open space of the channel. Of course, this computational domain represents only a small portion of the microfluidic chamber used in experimental studies, so our computational results only can be interpreted on a semiquantitative level, as a way to reveal and explore the underlying biophysical mechanism of the potassium-driven chemotaxis. For simplicity, we also neglected growth and division for motile cells and only considered their motion in response to the external potassium changes. We used periodic boundary conditions on the side walls for motile cells: when a motile cell touches the left wall, it disappears and reappears at the right side and vice versa. The non-motile biofilm cells were periodically switched between producing and absorbing potassium.

At each time step we computed the average concentration of potassium and the motile cell density near the biofilm edge. The periodic oscillations of cell density are clearly seen, which indicate that an oscillating source (biofilm) of extracellular potassium can periodically attract motile cells by changing their membrane potential (Fig. 4.3B).

Our model was predominantly informed by measurements in stationary cells, providing the opportunity to independently validate modeling predictions through additional motile cell measurements. In particular, we tested the modeling prediction that motile cells moving along a spatial potassium gradient are expected to have a similar membrane potential profile as stationary cells responding to temporal changes of potassium (Fig. 4.3C). In other words, motile cells during peak biofilm electrical activity should on average have a more negative membrane potential. To test this prediction, we measured the distribution of membrane potential in motile cells specifically at the attraction (peak) and non-attraction (trough) phases of the electrical oscillations in the biofilm. As predicted by our model, we find that motile cells have on average a more negative membrane potential in the attraction phase (Fig. 4.3D). These data show that similar to stationary cells, the

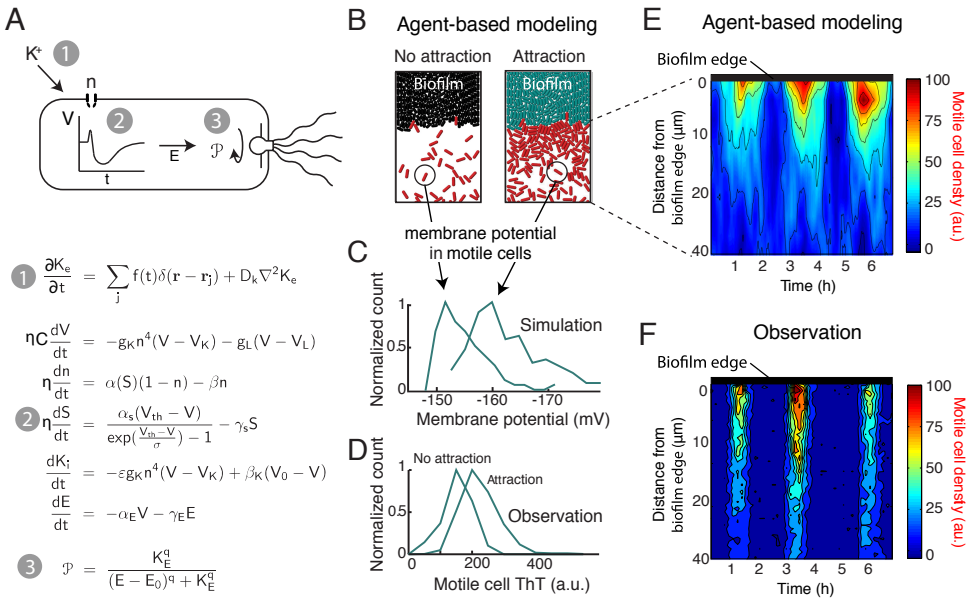

Figure 4.3: Agent-based modeling of motile cell attraction driven by electrical signaling from biofilms. (A) Top: schematic illustrating how extracellular potassium alters motility by changing the membrane potential. Step 1: extracellular potassium depolarizes the cell. Step 2: depolarization prompts adaptation by the cell leading to hyperpolarization. Step 3: hyperpolarization increases the proton motive force, thus directing motility by altering the tumbling frequency of the cell. Bottom: the computational model encompassing: (1) spatiotemporal reaction-diffusion model for the extracellular potassium K_e dynamics; (2) intracellular electrophysiological model for the cell membrane potential V, ion channel state n, metabolic stress S, intracellular potassium K_i, and energy needed to drive the flagellar motor E; and (3) discrete biomechanical model for individual cell motion influenced by their internal motility and interaction with other cells. The motility of individual cells is affected by the internal cellular state E via the change of the probability of tumbling. (B) Two snapshots of the combined agent-based simulation show increased density of motile (red) cells near the biofilm during the peak of the attraction phase to the biofilm. Biofilm cells are colored according to their membrane potential during each time point, where cyan coloring indicates more negative membrane potential relative to black coloring. (C) Distributions of membrane potential in motile cells from the computational model indicate that motile cell membrane potential is more negative during the peak of the attraction phase to the biofilm. (D) Experimental data confirm the modeling prediction that the distribution of motile cell membrane potential (ThT, a.u.) is more negative during attraction to the biofilm compared to the non-attraction phase. (E) Plot of motile cell density in the first 40 m away from the biofilm edge over time, obtained from agent-based modeling simulations of motile cell attraction. The region closest to the biofilm edge is located at the top of the plots for both (E) and (F) and distance from the biofilm edge increases moving downward. (F) Experimental data show similar motile cell density dynamics in the first 40 μm away from the biofilm edge.

membrane potential of motile cells also depends on the electrical activity of the biofilm. In addition, we find that the motile cell density profile as a function of time and distance from the biofilm is consistent with modeling predictions (Fig. 4.3E and F). Together, these results further validate the mathematical model and allow us to establish a coherent framework to interpret experimental observations.

4.2 A stabilized microbial ecosystem of self-limiting bacteria using synthetic quorum-regulated lysis

4.2.1 Two-strain co-culturing in experiments

Stability of an ecosystem cannot arise without mechanisms that prohibit the faster-growing species from eliminating the slower one. Orthogonal quorum-sensing (QS) systems and a population control circuit with diverse self-limiting growth dynamics can be combined to engineer two "ortholysis" circuits capable of maintaining a stable co-culture of metabolically competitive *Salmonella* Typhimurium strains in microfluidic devices. Basically, the circuit exhibits oscillations characterized by periodic lysis events, which are driven by activation of the Lux-controlled positive feedback loop upon reaching a quorum threshold of AHL, as seen in earlier [12]. A lysis event reduces the population dramatically, and a few survivors resume the process, starting again below the quorum threshold. The Lux and Rpa systems are suitable for two-way orthogonal signalling [13]. These components can be used to design synchronized lysis circuits (SLCs) [12] in two bacterial strains, where each strain is programmed to lyse upon reaching a critical population density (Fig. 4.4a). Through two orthogonal SLCs, two bacteria strains can be engineered to coexist in a common environment for long time (Fig. 4.4b).

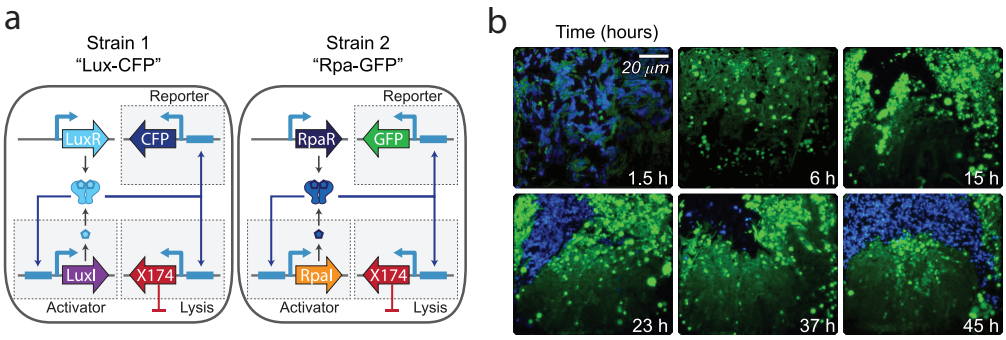

Figure 4.4: Experimental demonstration of long-term co-culture of competitive species with unequal growth rates using signal orthogonal self-lysis. (a) Genetic diagram of a two-strain ecosystem of self-lysing *Salmonella* constructed with two signal orthogonal QS systems, rpa and lux. (b) Video stills of a representative co-culture of the Lux-CFP and Rpa-GFP strains with the lysis plasmid. Addition of the lysis plasmid prevents either strain from taking over for the duration of the experiment.

4.2.2 Modeling

We used agent-based modeling to visually show how the "ortholysis" strains might behave with different QS parameters.

For the agent-based model, we use the same method as shown in the last section to simulate bacterial motion. To describe the intracellular dynamics of each cell, we adapted the ordinary differential equation model from [12]. Specifically, the intracellular dynamics are as follows:

$$\begin{aligned}
P_{lux} &= \alpha_0 + \alpha_H \frac{(\frac{H_i}{H_0})^m}{1+(\frac{H_i}{H_0})^m} \\
\frac{dH_i}{dt} &= b\frac{I_i}{K_I + I_i} + D_m(H_e(\mathbf{x}_i,t) - H_i) \\
\frac{dI_i}{dt} &= C_I P_{lux} - \gamma_I I_i \\
\frac{dL_i}{dt} &= C_L P_{lux} - \gamma_L L_i
\end{aligned}$$

Here the variables P_{lux}, H_i, I_i and L_i are the activity of luxI promoter, intracellular AHL, LuxI and

lysis protein of the i-th cell. $H_e(\mathbf{x}_i,t)$ is the extracellular concentration of AHL at the location of the i-th cell. luxI promoter is induced by AHL. $b\frac{I_i}{K_I+I_i}$ is the production term for AHL. $D_m(H_e(\mathbf{x}_i,t)-H_i)$ describes the exchange of intra- and extra-celluar AHL across the cell membrane. $C_I P_{lux}$ and $\gamma_I I_i$ are the production and degradation terms for LuxI. $C_L P_{lux}$ and $\gamma_L L_i$ are the production and degradation terms for lysis protein.

The extracellular AHL concentration $H_e(\mathbf{x},t)$ is governed by linear diffusion equation

$$\frac{\partial H_e(\mathbf{x},t)}{\partial t} = D_m \sum (H_i \delta(\mathbf{x}-\mathbf{x}_i) - H_e(\mathbf{x},t)) - \delta_H H_e(\mathbf{x},t) + D_H \nabla^2 H_e(\mathbf{x},t)$$

In the simulation, we use 2D finite difference methods to describe the diffusion of AHL.

We implement the model in traps with diffrent side lengths (20, 40 and 60). To simulate the lysis of each cell, we assume that when the concentration of lysis protein L_i is above a threshold L_{th}, the cell has a probability of $P_r = p_L(L_i - L_{th})$ per unit of time to lyse and once a cell lyses, it is removed from the trap.

We chose model parameters to qualitatively fit the experimental results and the parameters H_0, m, b, p_L were chosen to account for the differences of experimental measurements and dynamic behaviors between Lux-CFP and Rpa-GFP strains. The parameter values for the Lux-CFP strain are $\alpha_0 = 0.1$ (Lux promoter basal production); $\alpha_H = 2$ (Lux promoter AHL induced production); $H_0 = 1$ (AHL binding affinity to Lux promoter); $m = 4$ (Hill coefficient of AHL induced production of Lux promoter); $b = 1.5$ (AHL production rate); K_I (Conc. of LuxI resulting half maximum production of AHL); $D_m = 10$ (Diffusion constant of AHL across cell membrane); $C_I = 1$ (LuxI copy number); $\gamma_I = 1$ (Degradation rate of LuxI); $C_L = 1$ (Lysis gene copy number); $\gamma_L = 0.5$ (Degradation rate of lysis protein); $\delta_H = 0.1$ (Dilution rate of extracellular AHL); $D_H = 65$ (Diffusion constant of extracellular AHL); $p_L = 0.3$ (Probability of lysing); $L_{th} = 1.6$ (Threshold of lysis protein for lysis).

To simulate the constant-lysis Rpa-GFP strain, these parameters have different values:

$H_0 = 0.2, m = 1, b = 0.8, p_L = 0.03$. Besides, Rpa-GFP strain's growth rate is 10% larger than Lux-CFP strain.

We first modeled a system where the QS parameters of the Rpa system were the same as the Lux system parameters used in previous [12]. However, we used the experimental difference in growth whereby the Rpa-GFP strain grows at 110% the rate of the Lux-CFP strain. With the Lux-CFP strain seeded in a 10:1 ratio with respect to the Rpa-GFP strain in the model simulation, the resulting dynamics show antiphase oscillations (Fig. 4.5a). Seemingly due to volume exclusion, as shown by their fluorescence time series, the populations enter an antiphase pattern where the strains switch off growing and lysing (Fig. 4.5c).

We then took into consideration the innate differences between the two QS systems [13] by changing several of the Rpa-GFP strain's QS parameters in relation to the Lux parameters used. Furthermore, based on the observed phenotypic phenomenon, the probability of lysing was reduced tenfold, which allows more AHL to build up and a constant lysis dynamic to develop (Fig. 4.5b). The resulting dynamics were similar to the experimental observations, with a constantly lysing Rpa-GFP strain maintaining the majority of the population share and the Lux-CFP strain intermittently firing and lysing (Fig. 4.5d). To understand how these dynamics and the size of the growth container affect stability, the agent-based model was run many times under different conditions. For conditions where Lux-CFP is oscillating and Rpa-GFP is in constant lysis (lys/osc), or where both are oscillating (osc/osc), ten simulations were carried out in volumes of 20, 40 and 60 a.u. each. As the size of the space increases, so does the average residence time of the co-culture (Fig. 4.5e), suggesting that, as we expected, larger traps will have fewer issues with losing co-culture to stochastic events.

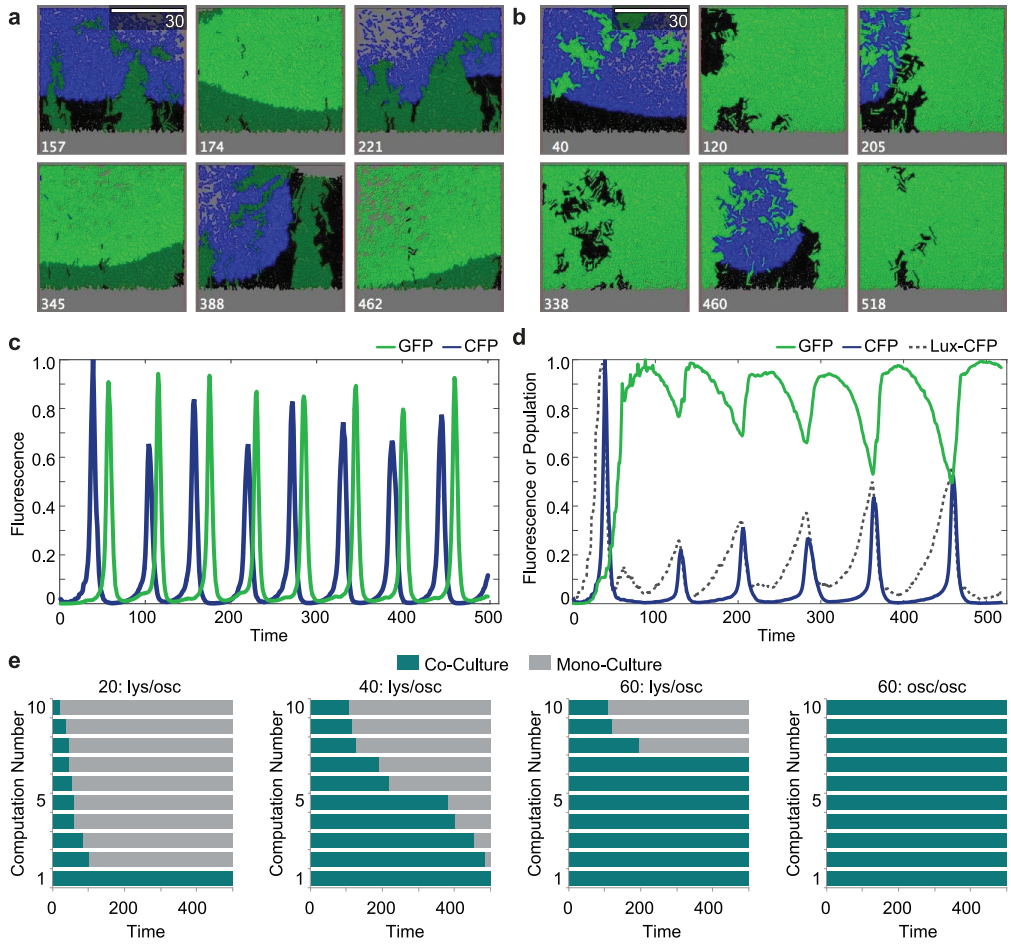

Figure 4.5: Agent-based model elucidating experimental dynamics. (a) Video stills of a representative, virtual co-culture of two self-lysing strains both in the oscillatory regime of the lysis circuit in a simulated trap of size 60. Scale bar at the top right of the micrograph indicates half of the size of the trap. The number at the bottom of the micrographs indicates iteration time. (b) Video stills of representative, model-generated video recreating experimental dynamics. The number at the bottom of the micrographs indicates iteration time. (c) Time trace of the GFP (green) and CFP (blue) fluorescence of the trap in a, over time. (d) Time trace of the GFP (green) and CFP (blue) fluorescence of the trap in (b), as well as population of the Lux-CFP strain (black dashed line). (e) From left to right: (1) GFP in constant lysis phase, CFP in the oscillatory phase in a trap with size 20; (2) GFP in constant lysis phase, CFP in the oscillatory phase in a trap with size 40; (3) GFP in constant lysis phase, CFP in the oscillatory phase in a trap with size 60 (the video in b is in this size trap with these lysing conditions); (4) both strains in oscillatory phase with trap size 60 (the video in a is in this size trap with these lysing conditions).

4.3 Acknowledgements

Chapter 4 contains material originally published as Humphries, J., Xiong, L., Liu, J., Prindle, A., Yuan, F., Arjes, H.A., Tsimring, L. and Suel, G.M., 2017. Species-independent attraction to

biofilms through electrical signaling. *Cell*. The chapter also contains material originally published as Scott, S.R., Din, M.O., Bittihn, P., Xiong, L., Tsimring, L.S. and Hasty, J., 2017. A stabilized microbial ecosystem of self-limiting bacteria using synthetic quorum-regulated lysis. *Nature Microbiology*. The dissertation author was the primary investigator of these papers.

References

[1] Jintao Liu, Arthur Prindle, Jacqueline Humphries, Marçal Gabalda-Sagarra, Munehiro Asally, D Lee Dong-yeon, San Ly, Jordi Garcia-Ojalvo, and Gürol M Süel. Metabolic co-dependence gives rise to collective oscillations within biofilms. *Nature*, 523(7562):550, 2015.

[2] Arthur Prindle, Jintao Liu, Munehiro Asally, San Ly, Jordi Garcia-Ojalvo, and Gürol M Süel. Ion channels enable electrical communication in bacterial communities. *Nature*, 527(7576):59, 2015.

[3] Alan L Hodgkin and Andrew F Huxley. A quantitative description of membrane current and its application to conduction and excitation in nerve. *The Journal of physiology*, 117(4):500–544, 1952.

[4] Declan A Doyle, Joao Morais Cabral, Richard A Pfuetzner, Anling Kuo, Jacqueline M Gulbis, Steven L Cohen, Brian T Chait, and Roderick MacKinnon. The structure of the potassium channel: molecular basis of k+ conduction and selectivity. *science*, 280(5360):69–77, 1998.

[5] Yu Cao, Yaping Pan, Hua Huang, Xiangshu Jin, Elena J Levin, Brian Kloss, and Ming Zhou. Gating of the trkh ion channel by its associated rck protein trka. *Nature*, 496(7445):317, 2013.

[6] Andreas Schlosser, Angela Hamann, Dirk Bossemeyer, Erwin Schneider, and Evert P Bakker. Nad+ binding to the escherichia coli k+-uptake protein trka and sequence similarity between trka and domains of a family of dehydrogenases suggest a role for nad+ in bacterial transport. *Molecular microbiology*, 9(3):533–543, 1993.

[7] Tarmo P Roosild, Samantha Miller, Ian R Booth, and Senyon Choe. A mechanism of regulating transmembrane potassium flux through a ligand-mediated conformational switch. *Cell*, 109(6):781–791, 2002.

[8] Tau-Mu Yi, Yun Huang, Melvin I Simon, and John Doyle. Robust perfect adaptation in bacterial chemotaxis through integral feedback control. *Proceedings of the National Academy of Sciences*, 97(9):4649–4653, 2000.

[9] Dmitri Volfson, Scott Cookson, Jeff Hasty, and Lev S Tsimring. Biomechanical ordering of dense cell populations. *Proceedings of the National Academy of Sciences*, 105(40):15346–15351, 2008.

[10] William Mather, Octavio Mondragón-Palomino, Tal Danino, Jeff Hasty, and Lev S Tsimring. Streaming instability in growing cell populations. *Physical review letters*, 104(20):208101, 2010.

[11] Christopher JD Fell and H Peter Hutchison. Diffusion coefficients for sodium and potassium chlorides in water at elevated temperatures. *Journal of Chemical & Engineering Data*, 16(4):427–429, 1971.

[12] M Omar Din, Tal Danino, Arthur Prindle, Matt Skalak, Jangir Selimkhanov, Kaitlin Allen, Ellixis Julio, Eta Atolia, Lev S Tsimring, Sangeeta N Bhatia, et al. Synchronized cycles of bacterial lysis for in vivo delivery. *Nature*, 536(7614):81, 2016.

[13] Spencer R Scott and Jeff Hasty. Quorum sensing communication modules for microbial consortia. *ACS synthetic biology*, 5(9):969–977, 2016.